Higgs and Heavy Meson Lattice Spectroscopy

Mark B. Wurtz

A Dissertation Submitted to
the Faculty of Graduate Studies
in Partial Fulfillment of the Requirements
for the degree of Doctor of Philosophy

Graduate Program in Physics and Astronomy
York University
Toronto, Ontario

September 2015

Abstract

Lattice simulations are a first principles method of numerically studying the spectrum of bound states. In quantum chromodynamics (QCD), lattice simulations have had tremendous success in accurately calculating the hadron spectrum. They also provide a non-perturbative description of the Higgs mechanism, where spontaneously broken gauge symmetry is substituted by Higgs-confinement complementarity.

Presented are studies of two different sectors of the standard model of particle physics using the latest methods in lattice spectroscopy. A search for exotic states in the SU(2)-Higgs model is performed using a variational analysis. All parameters are tuned to match their experimental values, including the recently discovered Higgs mass. A vast spectrum of multi-particle states is found and all are consistent with weakly interacting Higgs and W bosons, with no exotic candidates. In the QCD sector, the spectrum of heavy mesons that contain at least one bottom quark is extracted using free-form smearing. A new "minimal-path" implementation is introduced which maintains the usefulness of the original free-form smearing method and reduces its computational time dramatically. First lattice results of assorted radially and orbitally excited bottomonium and bottom-charm meson masses are presented. Calculations of the bottom-strange and bottom-up/down mesons are also performed. The methodology and results presented within are a significant contribution to the field of lattice spectroscopy.

Acknowledgements

Thank you to my supervisor Randy Lewis and our collaborator Richard Woloshyn.

Thank you to my colleagues Jamie Hudspith and Anthony Francis.

Also, thank you to Axel Maas for very fruitful discussions about lattice Higgs spectroscopy, Colin Morningstar for helpful discussions about the smearing of lattice operators, Georg von Hippel for helpful discussions about free-form smearing, Erhard Seiler for helpful correspondence about Higgs-confinement complementarity, Martin Lüscher for making his DD-HMC code publicly available, and the PACS-CS collaboration for making their dynamical gauge field ensembles publicly available. The calculations were done in part using computational resources from Westgrid (http://www.westgrid.ca) and Sharcnet (http://www.sharcnet.ca).

Also, thank you to Mr. Zurek for the excellent training and to all the other instructors at Beaches ITF.

This thesis is for Melissa and Jonathan.

Contents

List of Tables

List of Figures

Chapter 1

Introduction

1.1 Higgs Theory

The electroweak force of the standard model is mediated by four vector bosons: the massless photon γ, and the massive weak bosons $W^{\pm}$ and Z^0. A theory of the electroweak interactions is given by a $SU(2) \times U(1)$ gauge theory [1], but including an explicit mass term renders the theory nonrenormalizable and therefore not predictive beyond the classical approximation.

The problem of constructing a gauge theory of massive vector bosons was famously solved in 1964 [2–5] resulting in Nobel prizes for Englert and Higgs in 2013. The authors of [2–5] showed that a vacuum expectation value of the scalar field, minimally coupled to the gauge field, produces a vector boson mass within a renormalized theory. By breaking a local symmetry, the Goldstone theorem [6, 7] of massless particles with zero spin is circumvented. Instead of the degrees of freedom of a broken continuous symmetry resulting in Goldstone bosons, the vector bosons gain a longitudinal degree of freedom, i.e., a physical mass. This effect is more generally known as the Higgs mechanism.

A necessary outcome of a spontaneously broken symmetry involving a scalar field is the appearance of a scalar particle [8], called the Higgs boson. While the Goldstone bosons[1] come from "angular" components of the complex scalar doublet field, the Higgs boson corresponds to the radial component of the scalar field, and thus can not be removed by symmetry breaking. Therefore, an experimental detection of the Higgs boson and precise measurements of its properties provide a rigorous test for a scalar field as the root of the Higgs mechanism.

While the Higgs mechanism was conceived historically as an attempt to describe the strong

[1] Even though there may be no Goldstone bosons in the physical spectrum, as they donate themselves to the vector bosons, it can be still very useful to talk about them as elementary degrees of freedom.

interactions, it was later used to construct a unified theory of the electroweak interactions that is renormalizable [9–11]. By coupling a scalar field to $SU(2) \times U(1)$ gauge theory, mass terms for the $W^{\pm}$ and Z^0 bosons are generated by the Higgs mechanism while keeping the theory gauge invariant. The discovery of the Higgs boson at the Large Hadron Collider (LHC) in 2012 [12, 13] was an incredible vindication of the Higgs mechanism and of the electroweak theory. The measured Higgs mass of $125.09 \pm 0.21 \pm 0.11$ GeV/c^2 [14] fixes a parameter that has been unknown for nearly 50 years.[2]

A simplified version of the electroweak-Higgs sector is the $SU(2)$-Higgs model, where the photon and all fermions are removed. In this approximation, the $W^{\pm}$ bosons are electrically neutral and the Z^0 mass is equal to the W mass, forming a degenerate triplet (W^1, W^2, W^3) of massive vector bosons. This is a useful simplification because it retains the Higgs mechanism in a non-Abelian gauge theory. Non-Abelian gauge theories are intrinsically nontrivial because of the gauge field self-interactions. In the absence of spontaneous symmetry breaking the $SU(2)$-Higgs model is expected to having confining properties [15]. The scalar fields are confined to colourless bound states much like the quarks of QCD. Therefore, lattice studies of the gauge-Higgs theory are very useful because they allow the investigation of nonperturbative physics.

Early studies [15–29] of the $SU(2)$-Higgs model revealed a first-order phase transition which partially separates two regions: a confinement region with bound states similar to that of QCD, and a Higgs region with three massive vector bosons and a Higgs boson, consistent with physical expectations. These regions are analytically connected beyond the phase transition end point [15].

A smooth continuation between the two regions implies that bound states could persist into the Higgs region. Gauge-Higgs complementarity states that the physical Higgs and W bosons are bound states of the fundamental fields [30]. This contrasts with the traditional explanation of the Higgs mechanism involving spontaneous symmetry breaking of a gauge symmetry, where the fundamental fields directly correspond to the physical degrees of freedom by a choice of gauge fixing. If no gauge fixing term is present, then Elitzur's theorem [31]

[2]From now on this thesis will use conventional natural units where $\hbar = c = 1$. In those units the Higgs mass is 125 GeV. Sections 3.8 and 3.9 restore $\hbar$ and c for clarity.

says that gauge symmetry can not be spontaneously broken. The physical degrees of freedom can be formulated using gauge-invariant composite fields [32, 33], which supports their interpretation as bound states.

If the Higgs and W bosons are bound states, then it is natural to ask whether excited states exist in the spectrum. Contributions from radially excited Higgs and W bosons and orbitally excited D waves (where the Higgs and W bosons are treated as S-wave and P-wave states [34]) were considered in $W - W$ scattering cross sections [35], but the existence of these extra states is something that needs to be proven or disproven by a nonperturbative lattice simulation. Recent lattice simulations have investigated the question of additional bound states in the Higgs region [36–39], though conclusive evidence for their existence was not established.

Lattice simulations of the $SU(2)$-Higgs model in 2+1 dimensions investigated the spectrum over the smooth transition [40,41]. The spectrum in the confinement region is characterized by a "decoupling" mechanism, where the glueball mass and string tension are essentially unchanged from the pure gauge theory. Flux loops that are stable in the pure gauge theory can decay by producing pairs of scalars in the $SU(2)$-Higgs confinement region, though such decays are strongly suppressed and the flux loops are approximately stable. When approaching the analytic pathway into the Higgs region, such flux loop decays become so rapid that the particle description loses its relevance, leaving the Higgs region with the simple spectrum of Higgs and W bosons. The flux loops were probed with Polyakov loop operators, which couple to flux loops that wrap around the periodic lattice. The expectation value of a Polyakov loop also increases quickly (though smoothly) while moving into the Higgs region, indicating a sudden loss of confinement. Some evidence of a dense spectrum of states in the Higgs region was found at large values of the quartic coupling [41], though the authors concluded that a thorough study of multi-particle states is needed before a confident interpretation can be made.

The first lattice studies of the $SU(2)$-Higgs spectrum, dating back to the mid-1980's, used only the most basis methods and were sufficient to identify the basic spectrum. In the mid-1990's, more advanced methods were used to investigate the existence of bound states [40, 41]. Evidence was found for bound states in the confining region of the theory,

but the question remained open in the (physically realized) Higgs region of the theory. The discovery of the Higgs boson, plus recent speculative lattice studies [36, 37], have motatived the need for a more thorough investigation of bound states in Higgs physics, which this study provides [42, 43]. Strong evidence for bound states would have direct consequences for the experiments at the LHC as they could be discovered in the near future.

The goal of this study [42, 43] is to thoroughly investigate the spectrum of the $SU(2)$-Higgs model using lattice simulations. The calculations are performed in the Higgs region, which corresponds to the physically realized situation, with both parameters (m_H/m_W and $g^2/(4\pi)$) fixed to their experimental values. All channels given by the lattice irreducible representations of angular momentum, parity and weak isospin are investigated. Different types of operators are employed; some contain scalar fields and others only gauge fields, which allows one to cast a broad net in the search for nonperturbative and exotic states. In addition, explicit two-particle operators are analyzed to ensure that the multi-particle spectrum is understood.

1.2 Heavy Mesons

The bottom quark is the heaviest quark that can form a bound state[3]. Mesons (bound states of a quark and an anti-quark) containing at least one bottom quark are the heaviest to be detected. There are four types of mesons that contain bottom quarks, listed from heaviest to lightest: bottomonium, B_c, B_s and B, whose net quark content is $\overline{b}b$, $\overline{b}c$, $\overline{b}s$ and $\overline{b}u/d$, respectively. The latter three are called the bottom mesons, because they contain a bottom quark number of one, while bottomonium has a bottom number of zero due to the bottom quark anti-bottom quark pair. Throughout this study, the up and down quarks are assumed to be degenerate.

Heavy mesons provide a clean environment where the strong interactions between quarks can be studied in detail. The meson spectrum has many features that are analogues of other quantum mechanical bound states, such as hydrogen, like radial excitations, orbital excitations and hyperfine splitting. Experiments are able to measure these properties, in some

[3]The top quark is far heavier, but it decays too quickly to hadronize.

cases to sub-MeV precision. The richness and detailed experimental knowledge of the heavy meson spectrum allows for high precision tests of the theory of quantum chromodynamics (QCD) using numerical lattice simulations.

There is an abundant history of lattice studies of the bottomonium spectrum [44–52] and the bottom meson spectrum [53–63]. The bottom quark is difficult to directly simulate on the lattice because its mass is much heavier than the typical energy scale of the strong interaction. A commonly used method for incorporating the bottom quark into a lattice simulation is to treat the bottom quark nonrelativistically . This is called nonrelativistic QCD (NRQCD) [64–66], and is the framework used for the bottom quark in this study.

In the mid-1980's, before NRQCD was considered on the lattice, simulating the bottom quark was viewed as well beyond the capabilities of computers for many years. By the mid-1990's, within a few years of the first lattice NRQCD simulations, precise results for bottomonium and B mesons and their excited spectra were calculated on the lattice [44, 53–55], including predictions of previously unmeasured masses, well beyond what was previously thought possible. The precision and accuracy of the simulations have steadily improved with time [45, 50, 51, 56, 60, 61].

This study [67,68] builds on the work of previous lattice efforts for bottomonium and bottom meson spectroscopy. A persistent challenge to obtaining results for even higher excited states is the constuction of operators that are optimized for these states. By implementing the relatively new method of free-form smearing [69] to NRQCD for the first time, and greatly improving the general method of free-form smearing as well, the reach of lattice simulations is extended beyond what was previously possible and first lattice predictions for several unmeasured masses are made.

To study the various states in the spectrum, operators are constructed with the desired symmetries corresponding to angular momentum, parity and charge conjugation. While these properties can distinguish states with different quantum numbers, states with the same quantum numbers will mix. Building operators with a specific spatial shape allows greater selectivity of the various states, and is especially useful for radial and orbital excitations. To this end, free-form smearing is a method that allows the construction of gauge-invariant operators of an arbitrary shape [69].

Free-form smearing is used in this study [67, 68] to design operators that target specific states. This method allows for greater reliability and pushes the limits of lattice spectroscopy. A new implementation of free-form smearing is presented, which is based on the sum of minimal paths, and is much more computationally efficient than the original version. First lattice results for states in the bottomonium and B_c spectrum are reported. Predictions are provided for upcoming experiments, particularly in the B_c spectrum.

1.3 Lattice Methodology Overview

Lattice field theory is the study of quantum field theory on a discrete space-time lattice. Points in space and time are separated by a length scale called the lattice spacing, denoted by a, as shown in Fig. 1.1. Fields are assigned values only on the lattice sites. There are a finite number of points along each direction, given by L_i/a, where L_i is the length of the lattice along the ith direction.

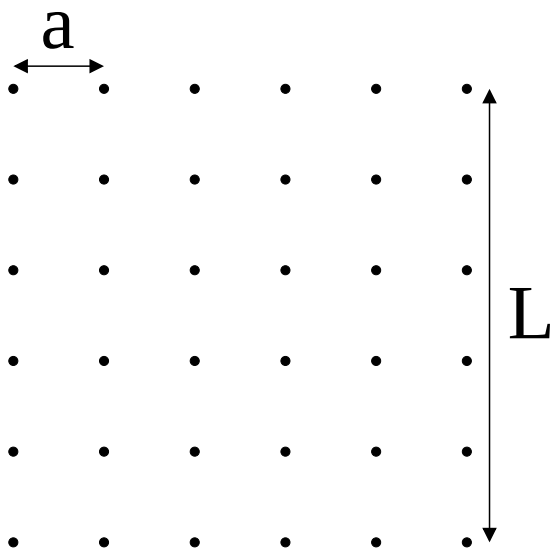

Figure 1.1: Sketch of a lattice in two dimensions. The length of the lattice is denoted by L and the lattice spacing by a.

The lattice formulation allows the Feynman path integral to be expressed as a finite number of integrations. Though there are still far too many integrals to apply brute force numerical integration, statistical methods are able to estimate the path integral. Performing a Wick rotation to Euclidean time, where $t \to -it$, the exponential of the action in the path

integral takes on purely real values and is interpreted as a Boltzmann distribution

$$\langle \mathcal{O}[U,\Phi] \rangle = \frac{\int \left(\prod_x dU_x d\Phi_x \right) \mathcal{O}[U,\Phi] e^{-S[U,\Phi]}}{\int \left(\prod_x dU_x d\Phi_x \right) e^{-S[U,\Phi]}} \quad , \tag{1.1}$$

where U are the lattice gauge fields and Φ are the matter fields. By using statistical Monte Carlo methods to generate a relatively small number of field configurations N, where the fields are distributed according to e^{-S}, the expectation value of an observable may be estimated by an average over the configurations

$$\langle \mathcal{O}[U,\Phi] \rangle = \frac{1}{N} \sum_{n=1}^{N} \mathcal{O}[U^{(n)},\Phi^{(n)}] \quad . \tag{1.2}$$

The uncertainty in Eq. (1.2) from sampling a finite number configurations from the ensemble is treated as a statistical error. Increasing the number of configurations decreases the statistical error by $1/\sqrt{N}$. The bootstrap resampling method is used to estimate the statistical uncertainty [70].

Configurations are generated in a Markov chain where a Monte Carlo update is applied to a previous configuration to create the next configuration

$$(U^{(0)},\Phi^{(0)}) \to (U^{(1)},\Phi^{(1)}) \to (U^{(2)},\Phi^{(2)}) \to (U^{(3)},\Phi^{(3)}) \to \cdots \to (U^{(N)},\Phi^{(N)}) \quad . \tag{1.3}$$

An initial field configuration is usually chosen to be either as random (hot start) or uniform (cold start). The Monte Carlo update satisfies the equilibrium condition

$$dp_{\text{eq}}(U^{(n+1)},\Phi^{(n+1)}) = \int dp_{\text{eq}}(U^{(n)},\Phi^{(n)}) \; P\left[(U^{(n)},\Phi^{(n)}) \to (U^{(n+1)},\Phi^{(n+1)})\right] \quad , \tag{1.4}$$

which guarantees that once the configurations reach an equilibrium distribution subsequent configurations remain in the equilibrium distribution. The equilibrium distribution is given by $dp_{\text{eq}}(U^{(n)},\Phi^{(n)})$ and $P\left[(U^{(n)},\Phi^{(n)}) \to (U^{(n+1)},\Phi^{(n+1)})\right]$ is the probability to generate the new configuration from the old configuration. Updates to the initial configurations, which are not started in equilibrium, will move towards the equilibrium distribution (or at least leave them where they are, but not away from equilibrium), a process called thermalization. Once the configurations thermalize, i.e., they are sampled from the equilibrium distribution,

they can used to compute expectation values, as in Eq. (1.2). However, care must be taken that neighbouring configurations in the Markov chain are not statistically correlated, which can cause bootstrap statistical uncertainties to be underestimated and results to be biased. This can be remedied by taking more Monte Carlo updates between sampling until the autocorrelations are sufficiently small. Another useful option is to average the observables into bins until the autocorrelations have been sufficiently reduced and bootstrap errors stabilize.

All quantities calculated using the lattice contain discretization errors, also called lattice artifacts. Physical results are obtained in the continuum limit where $a \to 0$. Typically, a full lattice analysis involves repeating calculations for different values of the lattice spacing and extrapolating to the continuum limit. This is a time consuming feat, and the analyses presented within consider only a single lattice spacing.

The analysis of the Higgs spectrum presented in Chapter 2 is an exploratory study, which looks for striking new features in the spectrum, and a careful continuum limit extrapolation is not necessary. The analysis of the heavy meson spectrum presented in Chapter 3 uses an improved action which reduces lattice discretization errors. As explained in Sec. 3.1, the non-relativistic treatment of the bottom quark is ill-defined in the continuum limit. Therefore the continuum limit can not be taken in this case. However, excellent results can still be obtained as long as the lattice spacing is not to large or too small.

The spectrum of energy eigenstates is extracted from two-point correlation functions of operators $\Psi(t)$ with respect to displacements in the time direction:

$$\begin{aligned}
\left\langle \Psi(t_2)\Psi^\dagger(t_1) \right\rangle &= \langle \Omega | \, \Psi e^{-H(t_2-t_1)} \Psi^\dagger \, | \Omega \rangle \\
&= \langle \Omega | \, \Psi \sum_n | n \rangle \langle n | \, e^{-H(t_2-t_1)} \Psi^\dagger \, | \Omega \rangle \\
&= \sum_n \left| \langle \Psi | n \rangle \right|^2 e^{-E_n(t_2-t_1)} \\
&= \sum_n c_n e^{-E_n(t_2-t_1)} \quad , \qquad (1.5)
\end{aligned}$$

where $|\Omega\rangle$ is the interaction vacuum state, $|n\rangle$ is the nth energy eigenstate and E_n are the energy eigenvalues. The use of Euclidean time allows for the low lying spectrum (small E_n) to be extracted by the exponential decay with respect to the time separation $t_2 - t_1$. The operator Ψ couples to the energy eigenstates by the matrix element $\langle \Omega | \, \Psi \, | n \rangle = \langle \Psi | n \rangle$.

Different methods to extract the spectrum were used in Chapters 2 and 3. In Chapter 2, the Higgs spectrum is extracted using a variational analysis applied to a matrix of correlation functions. This is a powerful and systematic method of calculating multiple energy levels, and is currently the cutting edge technique used in lattice spectroscopy. Chapter 2 is an exporatory study, testing for the existence of presently unknown states, and the variational method offers the greatest flexibility and reliability in this general search for new states.

Chapter 3 instead uses the relatively new method of free-form smearing to extract the spectrum of mesons containing bottom quarks. This study was initially motivated as a test of the usefulness of free-form smearing. High quality correlation functions are calculated from free-form smearing which allow for the first lattice exploration of several bottomonium and B_c meson states. Physical intuition is used to construct free-form smearing shapes that are optimized for the states of interest.

It is standard practice in lattice NRQCD studies to extract the spectrum by performing simultaneous fits of several correlation functions to multiple exponentials, and that method is applied here to free-form smeared correlation functions, as presented in Sec. 3.7. The advantage of this approach over the variational method is that the correlation functions are sufficiently precise to obtain high quality fits of the low lying spectrum, without the need of calculating a correlation function matrix. Calculating a matrix of correlation functions can be computationally expensive, and a sufficiently large basis of operators is needed for the variational method to be useful. Applying the variational method together with free-form is potentially a very powerful method, though is it currently a computationally expensive feat. The minimal-path implementation of free-form smearing presented in Sec. 3.4.3 opens the door towards this possibility, but this is beyond the scope of the present work.

1.4 Unique Contributions

New lattice methodologies were developed by the author for the projects presented within, which extend and significantly improve upon existing methods. In particular, the minimal-path method of free-form smearing given in Sec. 3.4.3 greatly improves upon the original method of Ref. [69]. Whereas the original implementation was limited by its high computation

time, the mininal-path approach greatly reduces the computation time, opening the door for this method to be applied more generally with a variety of lattice studies. The power of free-form smearing is demonstrated by the results in Chapter 3, which is the first time that this method has been used in an extensive study.

The study of the Higgs and W boson spectrum given in Chapter 2 is the first lattice study of the $SU(2)$-Higgs model in all 20 channels given by the lattice irreducible representations, parity and weak isospin. Previously, only three channels were studied [20, 24–27, 36, 40, 41] ($0(A_1^+)$, $0(E^+)$ and $1(T_1^-)$ in the notation given in Sec. 2.4.4). A large number of operators were constructed to access all of these channels, including explicit two-particle operators with non-zero internal momentum. Analyzing all of these operators has for the first time allowed for a confident interpretation of the entire spectrum.

For the work of Chapter 2, all computer code was written originally by the author (with the exception of the Linear Algebra PACKage [LAPACK] [71] where specified) in Fortran 90. This includes the Monte Carlo heatbath and overrelaxation updates for the gauge and scalar fields, stout-link and scalar field smearing, the calculation of the operators and correlation matrices, the variational method (LAPACK was used for the eigenvectors/values) and the uncorrelated χ^2–minimization fits (LAPACK was used for matrix inverse). For the work of Chapter 3, Fortran 90 code written by Randy Lewis and Richard Woloshyn was used for the calculation of the bottom quark propagator, stout-link and gaussian quark smearing, and the calculation of the meson two-point correlation function. The author wrote Fortran 90 code for the original and minimal-path implementations of free-form smearing within a partial wall source. The relativistic quark propagator was calculated using the DD-HMC code made publicly available by Martin Lüscher [72–74].

Chapter 2

Higgs Spectrum

2.1 Electroweak Theory

The (Euclidean) Lagrangian of the $SU(2) \times U(1)$-Higgs theory (all fermions removed[1]) is

$$\mathcal{L} = \tfrac{1}{4} F^a_{\mu\nu} F^a_{\mu\nu} + \tfrac{1}{4} G_{\mu\nu} G_{\mu\nu} + |D_\mu \Phi|^2 + \mu_0^2 |\Phi|^2 + \lambda_0 |\Phi|^4 \tag{2.1}$$

$$F^a_{\mu\nu} = \partial_\mu A^a_\nu - \partial_\nu A^a_\mu + g_0 \epsilon^{abc} A^b_\mu A^c_\nu \tag{2.2}$$

$$G_{\mu\nu} = \partial_\mu B_\nu - \partial_\nu B_\mu \tag{2.3}$$

$$D_\mu = \partial_\mu I + \tfrac{1}{2} i g_0 A^a_\mu \sigma^a + \tfrac{1}{2} i g_0' B_\mu I \tag{2.4}$$

$$\Phi = \begin{pmatrix} \phi_2 + i\phi_1 \\ \phi_0 - i\phi_3 \end{pmatrix} \quad , \tag{2.5}$$

where A^a_μ ($a = 1, 2, 3$) is the $SU(2)$ gauge field, B_μ is the $U(1)$ gauge field and Φ is a complex scalar doublet, μ_0 is the bare Higgs mass, λ_0 is the bare Higgs quartic coupling, g_0 is the $SU(2)$-gauge coupling and g_0' is the $U(1)$-gauge coupling. For values of $\mu_0^2 < 0$, the classical Higgs potential

$$V(\Phi) = \mu_0^2 |\Phi|^2 + \lambda_0 |\Phi|^4 \tag{2.6}$$

has a minimum value at

$$|\Phi| = \sqrt{\frac{-\mu_0^2}{2\lambda_0}} \quad , \tag{2.7}$$

which implies that the Higgs vacuum is spontaneously broken. The vacuum of the scalar field is assumed to spontaneously break gauge symmetry such that $\langle \phi_0 \rangle = v/\sqrt{2}$ and $\langle \phi_1 \rangle =$

[1]The fermions are not needed in this discussion of the Higgs mechanism and spontaneous breaking, and are neglected later on as well.

$\langle\phi_2\rangle = \langle\phi_3\rangle = 0$. Fluctuations around the vacuum are given by

$$\phi_0 = \frac{v+h}{\sqrt{2}} \quad , \tag{2.8}$$

where v is the Higgs vacuum expectation value and h is the field for the physical Higgs boson. Fixing to a unitary gauge ensures that $\phi_1 = \phi_2 = \phi_3 = 0$, which explicitly removes the unphysical Goldstone modes. The kinetic term for the scalar field then becomes

$$|D_\mu \Phi|^2 = \tfrac{1}{2}(\partial_\mu h)^2 + \left(\frac{g_0 v}{2}\right)^2 W_\mu^+ W_\mu^- + \tfrac{1}{2}\left(\frac{\sqrt{g_0^2 + g_0'^2}\, v}{2}\right) Z_\mu^2 \tag{2.9}$$

$$+ \text{interaction terms}$$

$$W_\mu^\pm = \frac{1}{\sqrt{2}}(A_\mu^1 \mp i A_\mu^2) \tag{2.10}$$

$$Z_\mu = \frac{1}{\sqrt{g_0^2 + g_0'^2}}(g_0 A_\mu^3 + g_0' B_\mu) \tag{2.11}$$

$$A_\mu = \frac{1}{\sqrt{g_0^2 + g_0'^2}}(-g_0' A_\mu^3 + g_0 B_\mu) \quad , \tag{2.12}$$

where the $W_\mu^\pm$ and Z_μ fields have acquired mass terms, but the photon field A_μ has not. The tree level masses for the $W^\pm$ and Z^0 bosons are

$$m_W = \frac{g_0 v}{2} \quad , \tag{2.13}$$

$$m_Z = \frac{\sqrt{g_0^2 + g_0'^2}\, v}{2} \quad , \tag{2.14}$$

and the weak mixing angle θ_W is defined by

$$\cos\theta_W = \frac{m_W}{m_Z} \quad . \tag{2.15}$$

The vacuum expectation value v is determined by the Fermi coupling constant

$$G_F = \frac{\sqrt{2}}{8}\frac{g_0^2}{m_W^2} = \frac{\sqrt{2}}{2v^2} = 1.166 \times 10^{-5}\,\text{GeV}^{-2} \quad , \tag{2.16}$$

which gives $v = 246\,\text{GeV}$. The gauge coupling constants are related to the fine structure constant at tree level by

$$\frac{1}{4\pi\alpha} = \frac{1}{g_0^2} + \frac{1}{g_0'^2} \quad . \tag{2.17}$$

2.2 Lattice SU(2)-Higgs model

The $SU(2)$-Higgs model is the subset of the standard model Higgs sector where all fermions and the photon have been removed. Removing the photon causes the $W^{\pm}$ bosons to become electrically neutral and the mass of the Z_0 boson to equal m_W, leaving a triplet of degenerate bosons labeled W_1, W_2 and W_3. Removing the fermions tremendously simplifies the lattice calculations.

The advantage of the $SU(2)$-Higgs model is that it retains the non-Abelian gauge fields which interact with the Higgs field, thus preserving the most relevant aspect of the Higgs mechanism in generating masses for the W bosons. Nonperturbatively, the $SU(2)$-Higgs model has a confining region with a phenomologically different spectrum than the physically realized Higgs region. The smooth analytic connection between these qualitatively different regions begs the question of whether nonperturbative states survive into the Higgs region of the theory, thus providing good motivation for a systematic and detailed study of the $SU(2)$-Higgs model in the physical region of parameter space.

The discretized $SU(2)$-Higgs action is given by

$$\begin{aligned} S[U,\Phi] = \sum_x \Bigg\{ & \beta \sum_{\mu<\nu} \left[1 - \tfrac{1}{2} \operatorname{Tr} \left(U_\mu(x) U_\nu(x+\hat{\mu}) U_\mu^\dagger(x+\hat{\nu}) U_\nu^\dagger(x) \right) \right] \\ & + \Phi^\dagger(x)\Phi(x) + \lambda \left(\Phi^\dagger(x)\Phi(x) - 1 \right)^2 \\ & - 2\kappa \sum_{\mu=1}^{4} \operatorname{Re} \left(\Phi^\dagger(x) U_\mu(x) \Phi(x+\hat{\mu}) \right) \Bigg\} \quad , \end{aligned} \tag{2.18}$$

where $U_\mu(x) = \exp\left(iag_0 \sigma^a A_\mu^a(x) \right)$ is the gauge field, $\Phi(x)$ is the scalar field, $\beta = 4/g_0^2$ is the gauge coupling, $\kappa = \frac{1-2\lambda}{8+a^2\mu_0^2}$ is the hopping parameter (related to the inverse bare mass squared), and $\lambda = \kappa^2 \lambda_0$ is the scalar self-coupling. Eq. (2.18) is invariant under the local gauge transformations

$$U_\mu(x) \to g(x) U_\mu(x) g^\dagger(x+\hat{\mu}) \quad , \tag{2.19}$$

$$\Phi(x) \to g(x) \Phi(x) \quad , \tag{2.20}$$

where $g(x) \in SU(2)$ is a function of space-time and is multiplied to the left of the scalar field.

There is an additional global flavour symmetry that exists for scalar fields in the fundamental representation of $SU(2)$. The action in Eq. (2.18) contains a symmetry in which the scalar field may be replaced by a dual copy $\hat{\Phi} = i\sigma_2\Phi^*$. Taking advantage of this duality, the scalar field can be written in 2×2 matrix form

$$\phi = \begin{pmatrix} \hat{\Phi} & \Phi \end{pmatrix} = \begin{pmatrix} \phi_0 + i\phi_3 & \phi_2 + i\phi_1 \\ -\phi_2 + i\phi_1 & \phi_0 - i\phi_3 \end{pmatrix} \quad . \tag{2.21}$$

The 2×2 complex scalar field is proportional to an $SU(2)$ matrix and is written as

$$\phi(x) = \rho(x)\alpha(x) \quad , \tag{2.22}$$

where $\rho(x) > 0$ is called the scalar length (or Higgs length) and $\alpha(x) \in SU(2)$ is the scalar field's "angular" component. The global flavour symmetry is now given by

$$\phi(x) \to \phi(x)g_W \quad , \tag{2.23}$$

where $g_W \in SU(2)$ is constant in space-time and is multiplied to the right of the scalar field. Writing the action with the matrix scalar field ϕ makes the weak isospin flavour symmetry explicit:

$$\begin{aligned} S[U,\phi] = \sum_x \Bigg\{ & \beta \sum_{\mu<\nu} \left[1 - \tfrac{1}{2}\,\mathrm{Tr}\left(U_\mu(x)U_\nu(x+\hat{\mu})U_\mu^\dagger(x+\hat{\nu})U_\nu^\dagger(x)\right)\right] \\ & + \tfrac{1}{2}\,\mathrm{Tr}\left(\phi^\dagger(x)\phi(x)\right) + \lambda\left(\tfrac{1}{2}\,\mathrm{Tr}\left(\phi^\dagger(x)\phi(x)\right) - 1\right)^2 \\ & - \kappa \sum_{\mu=1}^{4} \mathrm{Tr}\left(\phi^\dagger(x)U_\mu(x)\phi(x+\hat{\mu})\right) \Bigg\} \quad . \end{aligned} \tag{2.24}$$

Weak isospin, denoted by I, is a valuable quantum number for describing the spectrum of the $SU(2)$-Higgs model. The vector bosons are eigenstates of weak isospin, i.e., they are weak isovectors, and correspond to $I = 1$. The Higgs boson is a weak isoscalar and has $I = 0$.

2.3 Simulation Details

The simulations are performed in the Higgs region of the phase diagram, with a gauge coupling near the physical value $g_0^2 \approx \frac{4\pi\alpha}{\sin^2\theta_W} \approx \frac{4\pi\alpha}{1-m_W^2/m_Z^2} \approx 0.5$, corresponding to $\beta = 8$,

which is in the weak coupling region. The remaining parameters are tuned to $\kappa = 0.131$ and $\lambda = 0.0033$ to give a Higgs mass near the physical value of $\sim$125 GeV and a reasonable lattice spacing. The number of lattice sites is $20^3 \times 40$ (where the longer direction is Euclidean time) and $24^3 \times 48$, and the scale is set with the W mass defined to be 80.4 GeV. For comparison, separate simulations are carried out with $\kappa = 0.4$ and $\lambda = \infty$, which gives a much heavier Higgs mass.

Although ϕ^4 theories are trivial, the standard model can be viewed as an effective field theory up to some finite cutoff. The calculations presented in this paper are at a cutoff of approximately $1/a = 400$ GeV. Even though the continuum limit is problematic in a trivial theory, simulations at an appropriately large cutoff are sufficient to produce phenomenological results.

Standard heatbath and over-relaxation algorithms [75–82] were used for the Monte Carlo update of the gauge and scalar fields. Details of the algorithms are given in Appendix A. Define one sweep to mean an update at all sites across the lattice. Then the basic update step is one gauge heatbath sweep followed by two scalar heatbath sweeps followed by one gauge over-relaxation sweep followed by four scalar over-relaxation sweeps. Ten of these basic update steps are performed between the calculation of lattice observables. Any remaining autocorrelation is handled by binning the observables. For a given simulation, observables for 20000 configurations were calculated and placed in 100 bins of 200 configurations each.

For thermalization, 10000 basic update steps were used to create a thermalized configuration, which was saved and used as a starting point for several different Markov chains. Each Markov chain, using a different sequence of pseudorandom numbers, begins with the thermalized configuration and evolves it with another 1000 basic update steps to ensure that it is statistically independent. The different Markov chains are run in parallel trivially.

2.4 Operators

2.4.1 Stout Link Smearing

For the $SU(2)$-gauge links, one stout link iteration [83] is given by

$$U_\mu^{(n+1)}(x) = \exp\left\{iQ_\mu^{(n)}(x)\right\} U_\mu^{(n)}(x) \quad , \quad \mu \neq 4 \tag{2.25}$$

$$Q_\mu^{(n)}(x) = \frac{i}{2}\left(\Omega_\mu^{(n)}(x) - \Omega_\mu^{(n)\dagger}(x)\right) \tag{2.26}$$

$$\begin{aligned}\Omega_\mu^{(n)}(x) = \rho \sum_{\nu\neq\mu,\nu\neq 4} \Big\{ & U_\mu^{(n)}(x) U_\nu^{(n)}(x+\hat{\mu}) U_\mu^{(n)\dagger}(x+\nu) U_\nu^{(n)\dagger}(x) \\ & + U_\mu^{(n)}(x) U_\nu^{(n)\dagger}(x+\hat{\mu}-\hat{\nu}) U_\mu^{(n)\dagger}(x-\hat{\nu}) U_\nu^{(n)}(x-\hat{\nu}) \Big\}\end{aligned} \tag{2.27}$$

where ρ is the stout link smearing parameter. Only the spatial links are smeared, and only in the spatial direction. Since the 2×2 matrix $Q_\mu^{(n)}(x)$ is traceless and Hermitian, $\exp\left\{iQ_\mu^{(n)}(x)\right\}$ is an element of $SU(2)$ and thus $U_\mu^{(n+1)}(x)$ is an element of $SU(2)$. Using the Cayley-Hamilton theorem, which states that every matrix is a zero of its characteristic equation, the exponential of $Q_\mu^{(n)}(x)$ is written as

$$\exp\{iQ\} = \cos(\lambda) \cdot I + \frac{\sin(\lambda)}{\lambda} \cdot iQ \ , \tag{2.28}$$

$$\lambda = \sqrt{-\det(Q)} \quad , \tag{2.29}$$

where $\det(Q) \leq 0$. The final smeared links $\tilde{U}$ are given after a successive number of smearing iterations:

$$U = U^{(0)} \to U^{(1)} \to U^{(2)} \to \cdots \to U^{(N)} = \tilde{U}. \tag{2.30}$$

2.4.2 Scalar Smearing

The scalar smearing for the $SU(2)$-Higgs field [84–86] is given by

$$\phi^{(n+1)}(x) = (1+\alpha\Delta)\,\phi^{(n)}(x) \tag{2.31}$$

$$\begin{aligned}&= \phi^{(n)}(x) + \alpha \sum_{\mu=1}^{3} \Big\{ \tilde{U}_\mu(x) \phi^{(n)}(x+\hat{\mu}) - 2\phi^{(n)}(x) \\ &\qquad + \tilde{U}_\mu^\dagger(x-\hat{\mu}) \phi^{(n)}(x-\hat{\mu}) \Big\} \quad ,\end{aligned} \tag{2.32}$$

where Δ is the discrete Laplacian operator and α the smearing parameter. The gauge links $\tilde{U}$ are stout links. The scalar fields are smeared only in the spatial directions. The final smeared scalar fields $\tilde{\phi}$ are given after a successive number of smearing iterations:

$$\phi = \phi^{(0)} \to \phi^{(1)} \to \phi^{(2)} \to \cdots \to \phi^{(N)} = \tilde{\phi} \quad . \tag{2.33}$$

2.4.3 Higgs and W Boson Operators

To obtain information about continuum angular momentum from a lattice simulation, there is a well-known correspondence with irreducible representations (irreps) of the octahedral group of rotations [87, 88], given in Table 2.1. A detailed discussion is given in Appendix B, but the key result is repeated here for convenience. In this chapter, the results are given by the lattice irreps and can be interpreted in terms of the continuum angular momentum using Table 2.1.

Table 2.1: The continuum integer spins J corresponding to the irreducible representations Λ of the octahedral group O.

Λ	J							
	0	1	2	3	4	5	6	...
A_1	1	0	0	0	1	0	1	...
A_2	0	0	0	1	0	0	1	...
E	0	0	1	0	1	1	1	...
T_1	0	1	0	1	1	2	1	...
T_2	0	0	1	1	1	1	2	...

The simplest gauge-invariant operator that can be constructed from scalar fields is the Higgs length operator

$$H(t) = \frac{1}{2} \operatorname{Tr} \sum_{\vec{x}} \phi^\dagger(x)\phi(x) = \sum_{\vec{x}} \rho^2(x) \quad , \tag{2.34}$$

where the sum includes all spatial sites at a single Euclidean time. The $H(t)$ operator transforms according to the $\Lambda^{PC} = A_1^{++}$ irrep and thus couples to the spin-0 Higgs state. The Higgs operator is quadratic in the scalar field $\phi(x)$, rather than linear, as is familiar from

the earliest SU(2)-Higgs model lattice simulations [15–29]. In fact, it is not possible to build a gauge-invariant operator that contains an odd number of scalar fields.

Another useful operator that couples to the Higgs boson is the gauge-invariant link operator

$$L(t) = \frac{1}{2} \operatorname{Tr} \sum_{\vec{x}} \sum_{\mu} \phi^\dagger(x) U_\mu(x) \phi(x + \hat{\mu}) \quad , \tag{2.35}$$

where the link direction μ has been summed in all spatial directions. This operator is familiar from the last term of the action in Eq. (2.24). Notice that the matrix $\phi^\dagger(x) U_\mu(x) \phi(x + \hat{\mu})$ is gauge-invariant but still transforms under weak isospin. This gauge-invariant $SU(2)$ matrix contains four degrees of freedom: one corresponding to an isoscalar, as in Eq. (2.35), which is invariant under Eq. (2.23), and three isovector components, which may be obtained by multiplying a Pauli matrix and computing the trace.

The simplest operator that couples to the W boson is the isovector gauge-invariant link

$$W^a_\mu(t) = \frac{1}{2} \operatorname{Tr} \sum_{\vec{x}} -i\sigma^a \phi^\dagger(x) U_\mu(x) \phi(x + \hat{\mu}) \quad , \tag{2.36}$$

which belongs to the $\Lambda^P = T_1^-$ irrep, and thus corresponds to spin-1. The index $a = 1, 2, 3$ corresponds to the components of weak isospin ($I = 1$) and the index $\mu = 1, 2, 3$ to the components of spin ($J = 1$). The parity is negative because Eq. (2.36) reverses its sign for $\mu \to -\mu$.

Notice that, in general, an isovector operator does not have definite charge conjugation. The operator $W^a_\mu(t)$, for example, transforms under charge conjugation as

$$(W^1_\mu, W^2_\mu, W^3_\mu) \to (-W^1_\mu, +W^2_\mu, -W^3_\mu) \quad . \tag{2.37}$$

If the operator W^a_μ is given an arbitrary isospin rotation it will not be an eigenfunction of charge conjugation. In contrast, all isoscalar operators have only positive charge conjugation. Therefore charge conjugation is not a helpful quantum number for the present work.

Lattice operators for the Higgs and W bosons can also be understood in terms of continuum operators by expanding the link variables in powers of the lattice spacing. The operator

for the W boson from Eq. (2.36) is given by

$$\begin{aligned}&\mathrm{Tr}\left(-i\sigma^a\phi^\dagger(x)U_\mu(x)\phi(x+e_\mu)\right)\\&=\frac{1}{2}\,\mathrm{Tr}\left(-ia\sigma^a\left(\phi^\dagger(x)D_\mu\phi(x)-\left(D_\mu\phi(x)\right)^\dagger\phi(x)\right)\right)+O(a^2)\quad .\end{aligned}\tag{2.38}$$

The leading-order term in a is a gauge-invariant vector operator with $J^P=1^-$, which is a continuum W boson operator. The isoscalar gauge-invariant link operator from Eq. (2.35) is expanded as

$$\begin{aligned}&\mathrm{Tr}\left(\phi^\dagger(x)U_\mu(x)\phi(x+\hat{\mu})\right)\\&=\frac{1}{2}\,\mathrm{Tr}\left(\phi^\dagger(x)\phi(x)+\phi^\dagger(x+\hat{\mu})\phi(x+\hat{\mu})-a^2\left(D_\mu\phi(x)\right)^\dagger D_\mu\phi(x)\right)+O(a^3)\quad .\end{aligned}\tag{2.39}$$

The leading-order term is simply the gauge-invariant Higgs operator from Eq. (2.34) and has $J^P=0^+$. The order a^2 term contains two derivatives, which is interpreted as a W-W operator. Since the two-derivative operator is symmetric upon interchange and is a tensor (where both indices happen to be in the same direction for this particular lattice operator) its J^P is a linear combination of 0^+ and 2^+. Summing μ over the (x,y,z) directions will project out the spin-zero component, while taking differences $(x-y, x+y-2z)$ will isolate the spin-two components. Replacing the scalar field $\phi(x)$ with the "angular" field $\alpha(x)$, the isoscalar gauge-invariant link becomes

$$\mathrm{Tr}\left(\alpha^\dagger(x)U_\mu(x)\alpha(x+\hat{\mu})\right)=1+\frac{1}{2}\,\mathrm{Tr}\left(a^2\left(D_\mu\alpha(x)\right)^\dagger D_\mu\alpha(x)\right)+O(a^3)\quad ,\tag{2.40}$$

where the leading-order term contains two W boson operators.

2.4.4 Operators for All Channels

Other irreps can be obtained by considering operators with a more complicated shape. The gauge-invariant link operator

$$L^{\phi}_{\mu\nu\rho}(t) = \sum_{\vec{x}} \phi^{\dagger}(x) U_{\mu}(x) U_{\mu}(x+\hat{\mu}) U_{\nu}(x+2\hat{\mu}) \\ \times U_{\rho}(x+2\hat{\mu}+\hat{\nu}) \phi(x+2\hat{\mu}+\hat{\nu}+\hat{\rho}) \quad , \tag{2.41}$$

shown in Fig. 2.1, has 48 possible orientations and is one of the simplest two-scalar-field

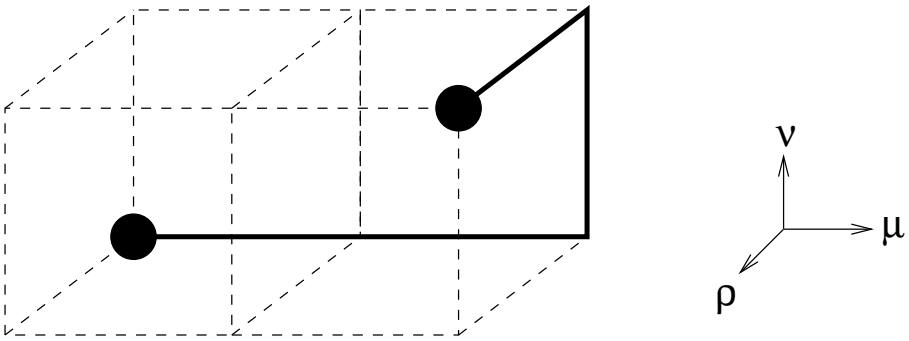

Figure 2.1: Sketch of the two-scalar-field operator $L_{\mu\nu\rho}$. The two dots at the ends of $L_{\mu\nu\rho}$ represent the scalar fields.

operators that couples to all of the $I(\Lambda^P)$ channels. Also considered is the gauge-invariant link constructed using $SU(2)$ "angular" components of the scalar field:

$$L^{\alpha}_{\mu\nu\rho}(t) = \sum_{\vec{x}} \alpha^{\dagger}(x) U_{\mu}(x) U_{\mu}(x+\hat{\mu}) U_{\nu}(x+2\hat{\mu}) \\ \times U_{\rho}(x+2\hat{\mu}+\hat{\nu}) \alpha(x+2\hat{\mu}+\hat{\nu}+\hat{\rho}) \quad , \tag{2.42}$$

which has exactly the same rotational properties as $L^{\phi}_{\mu\nu\rho}(t)$. Useful linear combinations of $L_{\mu\nu\rho}(t)$ (dropping the ϕ, α and t symbols for brevity) are given by

$$\begin{aligned} A^{+}_{\mu\nu\rho} &= L_{+\mu+\nu+\rho} + L_{+\mu+\nu-\rho} + L_{+\mu-\nu+\rho} + L_{+\mu-\nu-\rho} \\ &\quad + L_{-\mu+\nu+\rho} + L_{-\mu+\nu-\rho} + L_{-\mu-\nu+\rho} + L_{-\mu-\nu-\rho} \end{aligned} \tag{2.43}$$

$$\begin{aligned} A^{-}_{\mu\nu\rho} &= L_{+\mu+\nu+\rho} - L_{+\mu+\nu-\rho} - L_{+\mu-\nu+\rho} + L_{+\mu-\nu-\rho} \\ &\quad - L_{-\mu+\nu+\rho} + L_{-\mu+\nu-\rho} + L_{-\mu-\nu+\rho} - L_{-\mu-\nu-\rho} \end{aligned} \tag{2.44}$$

$$\begin{aligned} B^{+}_{\mu\nu\rho} &= L_{+\mu+\nu+\rho} - L_{+\mu+\nu-\rho} - L_{+\mu-\nu+\rho} + L_{+\mu-\nu-\rho} \\ &\quad + L_{-\mu+\nu+\rho} - L_{-\mu+\nu-\rho} - L_{-\mu-\nu+\rho} + L_{-\mu-\nu-\rho} \end{aligned} \tag{2.45}$$

$$\begin{aligned} B^{-}_{\mu\nu\rho} &= L_{+\mu+\nu+\rho} + L_{+\mu+\nu-\rho} + L_{+\mu-\nu+\rho} + L_{+\mu-\nu-\rho} \\ &\quad - L_{-\mu+\nu+\rho} - L_{-\mu+\nu-\rho} - L_{-\mu-\nu+\rho} - L_{-\mu-\nu-\rho} \end{aligned} \tag{2.46}$$

$$\begin{aligned} C^{+}_{\mu\nu\rho} &= L_{+\mu+\nu+\rho} + L_{+\mu+\nu-\rho} - L_{+\mu-\nu+\rho} - L_{+\mu-\nu-\rho} \\ &\quad - L_{-\mu+\nu+\rho} - L_{-\mu+\nu-\rho} + L_{-\mu-\nu+\rho} + L_{-\mu-\nu-\rho} \end{aligned} \tag{2.47}$$

$$\begin{aligned} C^{-}_{\mu\nu\rho} &= L_{+\mu+\nu+\rho} + L_{+\mu+\nu-\rho} - L_{+\mu-\nu+\rho} - L_{+\mu-\nu-\rho} \\ &\quad + L_{-\mu+\nu+\rho} + L_{-\mu+\nu-\rho} - L_{-\mu-\nu+\rho} - L_{-\mu-\nu-\rho} \end{aligned} \tag{2.48}$$

$$\begin{aligned} D^{+}_{\mu\nu\rho} &= L_{+\mu+\nu+\rho} - L_{+\mu+\nu-\rho} + L_{+\mu-\nu+\rho} - L_{+\mu-\nu-\rho} \\ &\quad - L_{-\mu+\nu+\rho} + L_{-\mu+\nu-\rho} - L_{-\mu-\nu+\rho} + L_{-\mu-\nu-\rho} \end{aligned} \tag{2.49}$$

$$\begin{aligned} D^{-}_{\mu\nu\rho} &= L_{+\mu+\nu+\rho} - L_{+\mu+\nu-\rho} + L_{+\mu-\nu+\rho} - L_{+\mu-\nu-\rho} \\ &\quad + L_{-\mu+\nu+\rho} - L_{-\mu+\nu-\rho} + L_{-\mu-\nu+\rho} - L_{-\mu-\nu-\rho} \end{aligned} \tag{2.50}$$

and Table 2.2 shows how to construct operators of any irrep and parity. Note that operators $A^{+}_{\mu\nu\rho}$, $B^{+}_{\mu\nu\rho}$, $C^{+}_{\mu\nu\rho}$ and $D^{+}_{\mu\nu\rho}$ are even under parity, whereas $A^{-}_{\mu\nu\rho}$, $B^{-}_{\mu\nu\rho}$, $C^{-}_{\mu\nu\rho}$ and $D^{-}_{\mu\nu\rho}$ are odd. The operators $A^{\pm}_{\mu\nu\rho}$ belong to the A_1, A_2 and E irreps, whereas $B^{\pm}_{\mu\nu\rho}$, $C^{\pm}_{\mu\nu\rho}$ and $D^{\pm}_{\mu\nu\rho}$ belong to the T_1 and T_2 irreps. The operator $L_{\mu\nu\rho}$ consists of four gauge-invariant real components: one is an isoscalar,

$$\frac{1}{2}\mathrm{Tr}(L_{\mu\nu\rho}) \quad , \tag{2.51}$$

and the other three form an isovector,

$$\frac{1}{2}\mathrm{Tr}(-i\sigma^{a}L_{\mu\nu\rho}) \quad . \tag{2.52}$$

Table 2.2: Linear combinations of operators from Eqs. (2.43)-(2.50) that give any irrep and parity. The multiplicity, mult(Λ^P), is shown for each case.

Λ^P	mult(Λ^P)	operators
A_1^+	1	$A^+_{123} + A^+_{231} + A^+_{312} + A^+_{132} + A^+_{213} + A^+_{321}$
A_1^-	1	$A^-_{123} + A^-_{231} + A^-_{312} - A^-_{132} - A^-_{213} - A^-_{321}$
A_2^+	1	$A^+_{123} + A^+_{231} + A^+_{312} - A^+_{132} - A^+_{213} - A^+_{321}$
A_2^-	1	$A^-_{123} + A^-_{231} + A^-_{312} + A^-_{132} + A^-_{213} + A^-_{321}$
E^+	2	$\big\{(A^+_{123} - A^+_{231} + A^+_{132} - A^+_{213})/\sqrt{2},$
		$(A^+_{123} + A^+_{231} - 2A^+_{312} + A^+_{132} + A^+_{213} - 2A^+_{321})/\sqrt{6}\big\}$
		$\big\{(A^+_{123} - A^+_{231} - A^+_{132} + A^+_{213})/\sqrt{2},$
		$(A^+_{123} + A^+_{231} - 2A^+_{312} - A^+_{132} - A^+_{213} + 2A^+_{321})/\sqrt{6}\big\}$
E^-	2	$\big\{(A^-_{123} - A^-_{231} + A^-_{132} - A^-_{213})/\sqrt{2},$
		$(A^-_{123} + A^-_{231} - 2A^-_{312} + A^-_{132} + A^-_{213} - 2A^-_{321})/\sqrt{6}\big\}$
		$\big\{(A^-_{123} - A^-_{231} - A^-_{132} + A^-_{213})/\sqrt{2},$
		$(A^-_{123} + A^-_{231} - 2A^-_{312} - A^-_{132} - A^-_{213} + 2A^-_{321})/\sqrt{6}\big\}$
T_1^+	3	$\big\{B^+_{123} - B^+_{132}\,,\, B^+_{231} - B^+_{213}\,,\, B^+_{312} - B^+_{321}\big\}$
		$\big\{C^+_{123} - C^+_{213}\,,\, C^+_{231} - C^+_{321}\,,\, C^+_{312} - C^+_{132}\big\}$
		$\big\{D^+_{123} - D^+_{321}\,,\, D^+_{231} - D^+_{132}\,,\, D^+_{312} - D^+_{213}\big\}$
T_1^-	3	$\big\{B^-_{123} + B^-_{132}\,,\, B^-_{231} + B^-_{213}\,,\, B^-_{312} + B^-_{321}\big\}$
		$\big\{C^-_{123} + C^-_{321}\,,\, C^-_{231} + C^-_{132}\,,\, C^-_{312} + C^-_{213}\big\}$
		$\big\{D^-_{123} + D^-_{213}\,,\, D^-_{231} + D^-_{321}\,,\, D^-_{312} + D^-_{132}\big\}$
T_2^+	3	$\big\{B^+_{123} + B^+_{132}\,,\, B^+_{231} + B^+_{213}\,,\, B^+_{312} + B^+_{321}\big\}$
		$\big\{C^+_{123} + C^+_{213}\,,\, C^+_{231} + C^+_{321}\,,\, C^+_{312} + C^+_{132}\big\}$
		$\big\{D^+_{123} + D^+_{321}\,,\, D^+_{231} + D^+_{132}\,,\, D^+_{312} + D^+_{213}\big\}$
T_2^-	3	$\big\{B^-_{123} - B^-_{132}\,,\, B^-_{231} - B^-_{213}\,,\, B^-_{312} - B^-_{321}\big\}$
		$\big\{C^-_{123} - C^-_{321}\,,\, C^-_{231} - C^-_{132}\,,\, C^-_{312} - C^-_{213}\big\}$
		$\big\{D^-_{123} - D^-_{213}\,,\, D^-_{231} - D^-_{321}\,,\, D^-_{312} - D^-_{132}\big\}$

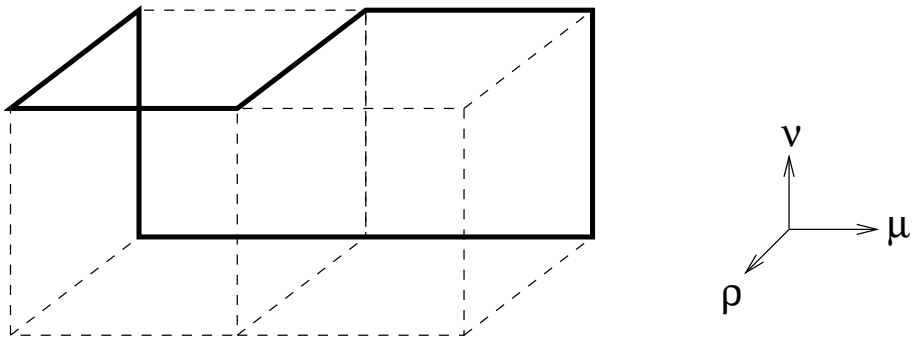

Figure 2.2: The Wilson loop operator $W_{\mu\nu\rho}$ of Eq. (2.53).

In addition to the gauge-invariant link, which contains two scalar fields, there are operators that contain only gauge fields. A Wilson loop is a gauge-invariant operator in which the path of gauge links returns to itself to form a closed loop. A particular Wilson loop that couples to all available irreps is shown in Fig. 2.2. Mathematically, it is

$$W_{\mu\nu\rho}(t) = \frac{1}{2}\,\mathrm{Tr}\sum_{\vec{x}} U_\mu(x)U_\mu(x+\hat{\mu})U_\nu(x+2\hat{\mu})U_\mu^\dagger(x+\hat{\mu}+\hat{\nu}) \\ \times U_\rho(x+\hat{\mu}+\hat{\nu})U_\mu^\dagger(x+\hat{\nu}+\hat{\rho})U_\rho^\dagger(x+\hat{\nu})U_\nu^\dagger(x) \tag{2.53}$$

which is operator #4 in Table 3.2 of Ref. [88] and has 48 different orientations. A Polyakov loop is also a gauge-invariant closed loop, but it wraps around a boundary of the periodic lattice. All irreps can be obtained from a Polyakov loop that contains a "kink," denoted by $K_{\mu\nu\rho}$, such as the one shown in Fig. 2.3, which is

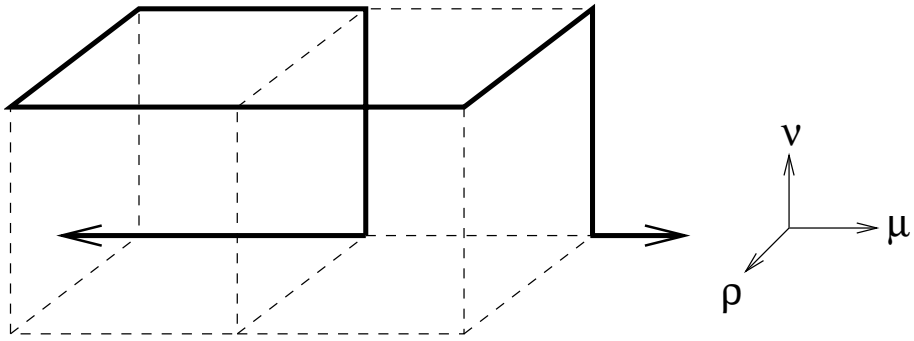

Figure 2.3: The "kinked" Polyakov loop operator $P_{\mu\nu\rho}$ of Eq. (2.54).

$$P_{\mu\nu\rho}(t) = \frac{1}{2}\,\mathrm{Tr}\sum_{\vec{x}}\left\{\prod_{y_\mu<x_\mu} U_\mu(x+(y_\mu-x_\mu)\hat{\mu})\right\}K_{\mu\nu\rho}(x) \times\left\{\prod_{y_\mu>x_\mu} U_\mu(x+(y_\mu-x_\mu)\hat{\mu})\right\} \tag{2.54}$$

$$K_{\mu\nu\rho}(x) = U_\nu(x)U_\mu^\dagger(x+\hat{\nu}-\hat{\mu})U_\rho(x+\hat{\nu}-\hat{\mu})U_\mu(x+\hat{\nu}-\hat{\mu}+\hat{\rho}) \times U_\mu(x+\hat{\nu}+\hat{\rho})U_\rho^\dagger(x+\hat{\nu}+\hat{\mu})U_\nu^\dagger(x+\hat{\mu}) \quad , \tag{2.55}$$

and has 48 different orientations. The kink $K_{\mu\nu\rho}$ is inserted to fill the gap between points x and $x+\hat{\mu}$ of an otherwise normal Polyakov loop. All possible irreps and parities for $W_{\mu\nu\rho}$ and $P_{\mu\nu\rho}$ can be obtained from Table 2.2 simply by replacing $L_{\mu\nu\rho}$ with $W_{\mu\nu\rho}$ or $P_{\mu\nu\rho}$ in Eqs. (2.43) to (2.50). Since a Pauli matrix cannot be inserted into the trace of a closed loop operator made entirely of gauge links without destroying gauge invariance, there are no isovector Wilson or Polyakov loop operators.

To reduce the computer time required to compute Eq. (2.54), a computationally efficient method was devised and implemented. The kinked Polyakov loop $P_{\mu\nu\rho}$ is computed by first constructing an ordinary (untraced) Polyakov loop in the μ direction

$$P_\mu(x) = \prod_{y_\mu} U_\mu(x+y_\mu) \quad . \tag{2.56}$$

Then one link is removed from the left side of $P_\mu(x)$, creating a Polyakov loop with a gap $U_\mu^\dagger(x)P_\mu(x)$. The gap is filled by multiplying the kink $K_{\mu\nu\rho}(x)$ on the left of the gapped Polyakov loop to give

$$P_{\mu\nu\rho}(x) = \frac{1}{2}\,\mathrm{Tr}\left(K_{\mu\nu\rho}(x)U_\mu^\dagger(x)P_\mu(x)\right) \quad . \tag{2.57}$$

To calculate the kinked Polyakov loop at the next spatial site $P_{\mu\nu\rho}(x+\hat{\mu})$, the gapped Polyakov loop from above is filled by multiplying a link on the right, and then a new gapped Polyakov loop is made by removing another link from the left, giving

$$P_{\mu\nu\rho}(x+\hat{\mu}) = \frac{1}{2}\,\mathrm{Tr}\left(K_{\mu\nu\rho}(x+\hat{\mu})U_\mu^\dagger(x+\hat{\mu})U_\mu^\dagger(x)P_\mu(x)U_\mu(x)\right) \quad . \tag{2.58}$$

This procedure continues iteratively until a kink has been inserted along every point of $P_\mu(x)$. The advantage of this method is that the long portion of the kinked Polyakov loop does not

have to be recalculated at every site x. Instead, only a small change is applied to the ends of the Polyakov loop. This reduces the computation time required to construct $P_{\mu\nu\rho}$ from $O(L^4)$ to $O(L^3)$, where L is the number of lattice sites in each of the spatial directions.

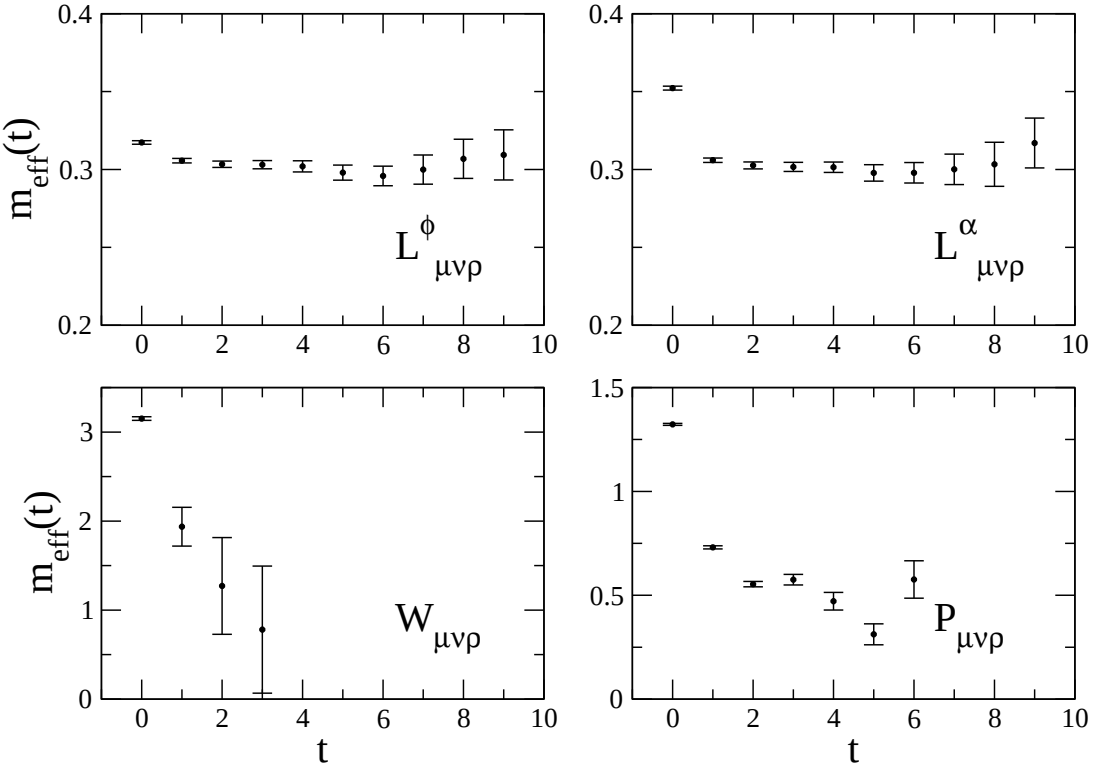

Figure 2.4: Effective masses of the $I(\Lambda^P) = 0(A_1^+)$ gauge-invariant link operators $L^{\phi}_{\mu\nu\rho}$ and $L^{\alpha}_{\mu\nu\rho}$, Wilson loop $W_{\mu\nu\rho}$ and Polyakov loop $P_{\mu\nu\rho}$ operators on a $20^3 \times 40$ lattice with $\beta = 8$, $\kappa = 0.131$ and $\lambda = 0.0033$. No smearing was used.

To illustrate the efficacy of the operators, consider effective masses

$$m_{\text{eff}}(t) = -\log\left(\frac{\langle \mathcal{O}(t+1)\mathcal{O}(0)\rangle}{\langle \mathcal{O}(t)\mathcal{O}(0)\rangle}\right) \tag{2.59}$$

where $\mathcal{O}(t)$ is a gauge-invariant operator with its vacuum expectation value subtracted,

$$\mathcal{O}(t) = O(t) - \langle O(t)\rangle \quad . \tag{2.60}$$

Figures 2.4, 2.5 and 2.6 show effective mass plots of four operator types: two gauge-invariant links ($L^{\phi}_{\mu\nu\rho}$ and $L^{\alpha}_{\mu\nu\rho}$), a Wilson loop $W_{\mu\nu\rho}$, and a Polyakov loop $P_{\mu\nu\rho}$. Figures 2.4 and 2.5 correspond to the $I(\Lambda^P) = 0(A_1^+)$ channel, where the former contains no smearing and the latter has stout links and scalar smearing. The stout link and smearing parameters are

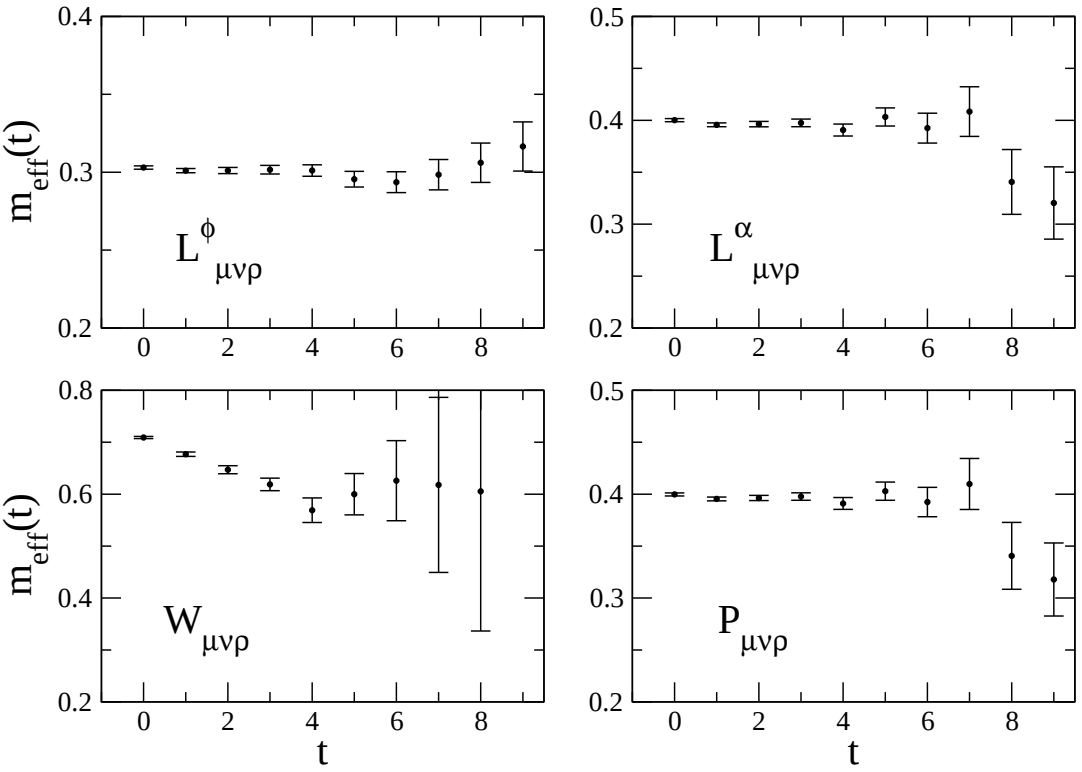

Figure 2.5: Effective masses of the $I(\Lambda^P) = 0(A_1^+)$ gauge-invariant link operators $L^{\phi}_{\mu\nu\rho}$ and $L^{\alpha}_{\mu\nu\rho}$, Wilson loop $W_{\mu\nu\rho}$ and Polyakov loop $P_{\mu\nu\rho}$ operators on a $20^3 \times 40$ lattice with $\beta = 8$, $\kappa = 0.131$ and $\lambda = 0.0033$. The stout link and smearing parameters are $n_{\rm stout} = n_{\rm smear} = 200$ and $r_{\rm stout} = r_{\rm smear} = 0.1$.

$n_{\rm stout} = n_{\rm smear} = 200$ and $r_{\rm stout} = r_{\rm smear} = 0.1$. Figure 2.6 shows the $0(A_1^-)$ channel with stout links and scalar smearing. A statistically non-zero signal for the $0(A_1^-)$ channel could not be obtained without the aid of link and scalar field smearing. The same is true for many other $I(\Lambda^P)$ channels.

The $0(A_1^+)$ channel is expected, at least, to contain a Higgs boson. From the non-smeared operators in Fig. 2.4, the gauge-invariant link operators give a mass near 0.3 in lattice units. The Wilson and Polyakov loop operators indicate the presence of heavier states, though their signals are quite noisy. The smeared operators in Fig. 2.5 have an improved signal for the Wilson and Polyakov loops. The $L^{\alpha}_{\mu\nu\rho}$ and $P_{\mu\nu\rho}$ operators in Fig. 2.5 now show a mass near 0.4 in lattice units, while $L^{\phi}_{\mu\nu\rho}$ remains relatively unchanged. The smeared $L^{\alpha}_{\mu\nu\rho}$ and $P_{\mu\nu\rho}$ operators have nearly identical effective mass plots despite being conceptually very different operators. The Wilson loop continues to show contamination from heavier states. This is

an indication that the $0(A_1^+)$ spectrum (corresponding to $J = 0$ in the continuum) contains more than a lone Higgs boson.

For $0(A_1^-)$, Fig. 2.6 shows that the gauge-invariant links give a mass at 0.6 in lattice units, while the Wilson and Polyakov loops are contaminated by heavier states. Again this is $J = 0$ in the continuum, and neither a single Higgs nor a single W has $J^P = 0^-$. An analysis that allows the systematic identification of the low lying states of this and all other channels is discussed below.

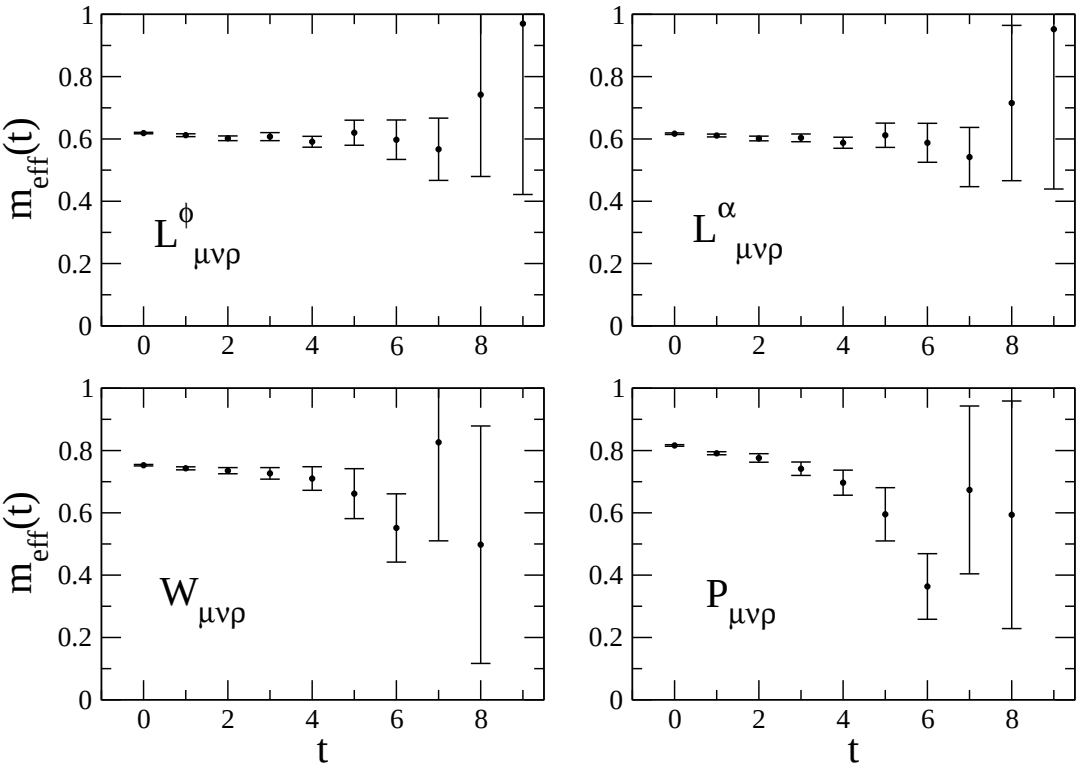

Figure 2.6: Effective masses of the $I(\Lambda^P) = 0(A_1^-)$ gauge-invariant link operators $L^{\phi}_{\mu\nu\rho}$ and $L^{\alpha}_{\mu\nu\rho}$, Wilson loop $W_{\mu\nu\rho}$ and Polyakov loop $P_{\mu\nu\rho}$ operators on a $20^3 \times 40$ lattice with $\beta = 8$, $\kappa = 0.131$ and $\lambda = 0.0033$. The stout link and smearing parameters are $n_{\text{stout}} = n_{\text{smear}} = 200$ and $r_{\text{stout}} = r_{\text{smear}} = 0.1$.

2.5 Correlation Matrix and Variational Method

Particle energies, E_n, are extracted from lattice simulations by observing the exponential decay of correlation functions,

$$C_{ij}(t) = \langle \mathcal{O}_i(t)\mathcal{O}_j(0)\rangle = \sum_n \langle 0|\, \mathcal{O}_i\, |n\rangle \, \langle n|\, \mathcal{O}_j\, |0\rangle \exp\left(-E_n t\right) \tag{2.61}$$

$$= \sum_n a_i^n a_j^n \exp\left(-E_n t\right) \quad , \tag{2.62}$$

where $\mathcal{O}_i(t)$ is a Hermitian gauge-invariant operator with its vacuum expectation value subtracted as in Eq. (2.60). The choice of operator determines the quantum numbers $I(\Lambda^P)$ of the states $|n\rangle$ that are present in the correlation function and also determines the coupling strength, a_i^n, to each. The operators are calculated for eight different levels of smearing, $n_{\text{stout}} = n_{\text{smear}} = 0$, 5, 10, 25, 50, 100, 150, and 200. The smearing parameters are held fixed at $r_{\text{stout}} = r_{\text{smear}} = 0.1$. Each of these different smearing levels produces a unique operator $\mathcal{O}_i$ in the correlation matrix $C_{ij}(t)$.

The energy spectrum is extracted using the variational method [89, 90]. To begin, the eigenvectors $\vec{v}_n$ and eigenvalues λ_n $(n = 1, ..., M)$ of the correlation matrix are found at a single time step $C_{ij}(t_0)$ $(i, j = 1, ..., N)$, where N is the number of operators, M is the number of statistically nonzero eigenvalues, which corresponds to the number of states that can be resolved, and $M \leq N$. The value of t_0 is typically chosen to be small, e.g., $t_0 = 1$, where the signal-to-noise ratio is large. The correlation matrix is changed from the operator basis to the eigenvector basis by

$$\widetilde{C}_{nm}(t) = \frac{\vec{v}_n^T C(t) \vec{v}_m}{\sqrt{\lambda_n \lambda_m}} \quad . \tag{2.63}$$

The correlation function for the kth $(k = 1, ..., M)$ state is then given by

$$C_k(t) = \vec{R}_k^T \widetilde{C}(t) \vec{R}_k \quad , \tag{2.64}$$

where $\vec{R}_k$ is a set of orthonormal vectors chosen such that the energies from $C_k(t)$ are ordered from smallest to largest for increasing k. $\vec{R}_k$ is determined recursively by a variational method as follows: $\vec{R}_1$ maximizes $C_1(t_1)$, the correlation function of the smallest energy at a time step $t_1 > t_0$. The normalization of Eq. (2.63) ensures that $C_k(t_0) = 1$, thus maximizing $C_1(t_1)$

ensures that $\vec{R}_1$ projects out the state with smallest energy while minimizing contamination from higher-energy states. In practice, the time step t_1 is taken to be t_0+1. The optimization of $C_1(t_1)$ reduces to solving the eigenproblem

$$\widetilde{C}(t_1)\vec{x}_1 = \mu_1\vec{x}_1 \quad , \tag{2.65}$$

where the eigenvalue μ_1 is the Lagrange multiplier for the constraint $\vec{R}_1^T\vec{R}_1 = 1$, and the solution for $\vec{R}_1$ is given by the eigenvector $\vec{x}_1$ that maximizes $C_1(t_1)$. The correlation function $C_2(t)$ of the next-smallest-energy state can be found by calculating $\vec{R}_2$ in the same way as above, given that $\vec{R}_2$ must be orthonormal to $\vec{R}_1$. This is accomplished by defining $\vec{R}_2$ as the vector

$$\vec{x}_2 = \sum_{n=1}^{M-1} a_n\vec{x}_{1,n} \tag{2.66}$$

that maximizes $C_2(t_1)$, where $\vec{R}_1 = \vec{x}_{1,M}$ and $\vec{x}_{1,n}$ $(n = 1, ..., M-1)$ are the remaining eigenvectors from Eq. (2.65). The eigenproblem resulting from the maximization of $C_2(t_1)$ is

$$X_1^T\widetilde{C}(t_1)X_1\vec{a} = \mu_2\vec{a} \quad , \tag{2.67}$$

where the matrix $X_1 = (\vec{x}_{1,1}, ..., \vec{x}_{1,M-1})$, the vector $\vec{a}^T = (a_1, ..., a_{M-1})$ contains the coefficients from Eq. (2.66) and the vector $\vec{R}_2 = X_1\vec{a}$ is calculated from the eigenvector $\vec{a}$ that maximizes $C_2(t_1)$. The calculation can continue recursively up to the Mth case, where the eigenproblem becomes trivial.

The energy can then be extracted by a (uncorrelated) χ^2-minimizing fit using

$$C_k(t) = A_k\left(\exp(-E_kt) + \exp(-E_k(L_t - t))\right) \quad . \tag{2.68}$$

where L_t is the length of the lattice in the time direction. In practice, the fit is performed with data from $t = 2$ to $t = L_t/2$.

Examples of results from the variational method described above are shown in Figs. 2.7, 2.8 and 2.9 for the $I(\Lambda^P) = 0(A_1^+)$, $0(A_1^-)$ and $1(T_1^-)$ channels, respectively. The lightest few states are cleanly separated and free from contamination from heavier states. Many states with a variety of energy levels are observed. An analysis of all channels and interpretation of the spectrum is given in the following sections.

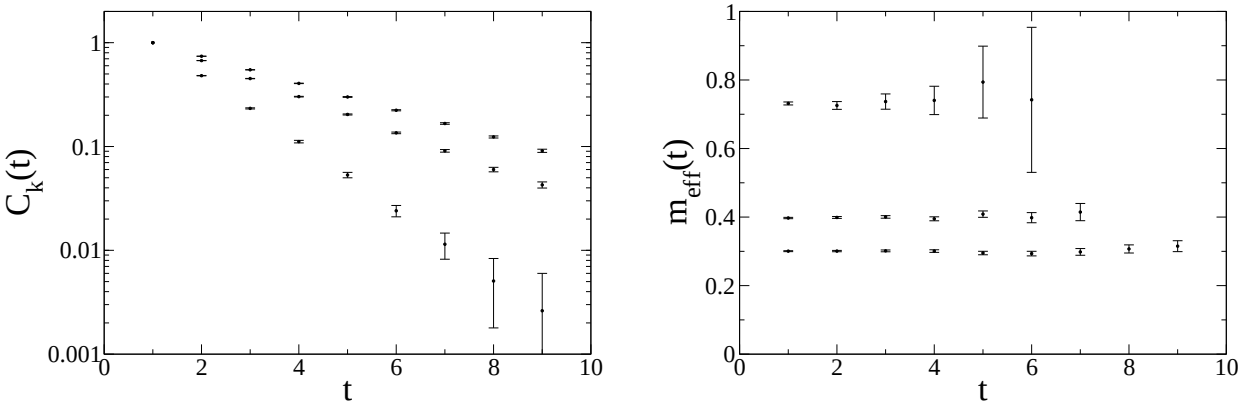

Figure 2.7: Results for the three lightest states in the $I(\Lambda^P) = 0(A_1^+)$ channel following from a variational analysis of gauge-invariant link operators ($L^{\phi}_{\mu\nu\rho}$ and $L^{\alpha}_{\mu\nu\rho}$) on a $20^3 \times 40$ lattice with $\beta = 8$, $\kappa = 0.131$ and $\lambda = 0.0033$. Left panel: correlation functions from Eq. (2.64) ($k = 1, 2, 3$). Right panel: Effective masses of the correlation functions on the left.

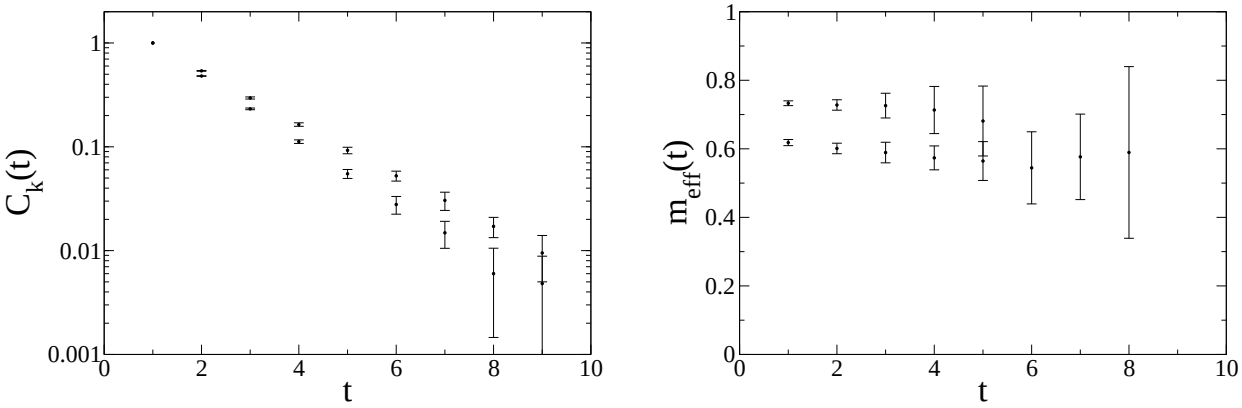

Figure 2.8: Results for the two lightest states in the $I(\Lambda^P) = 0(A_1^-)$ channel following from a variational analysis of Wilson and Polyakov loop operators ($W_{\mu\nu\rho}$ and $P_{\mu\nu\rho}$) on a $20^3 \times 40$ lattice with $\beta = 8$, $\kappa = 0.131$ and $\lambda = 0.0033$. Left panel: correlation functions from Eq. (2.64) ($k = 1, 2$). Right panel: Effective masses of the correlation functions on the left.

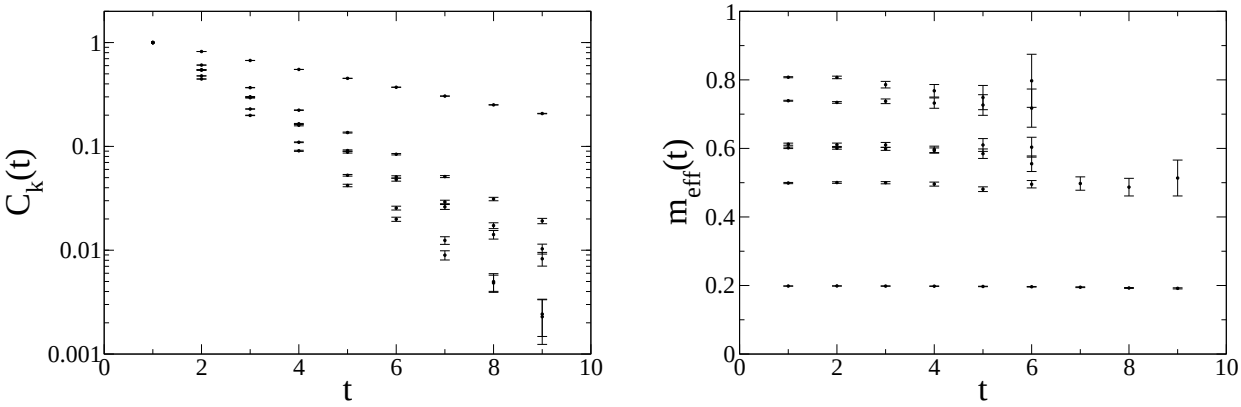

Figure 2.9: Results for the five lightest states in the $I(\Lambda^P) = 1(T_1^-)$ channel following from a variational analysis of gauge-invariant link operators ($L^{\phi}_{\mu\nu\rho}$ and $L^{\alpha}_{\mu\nu\rho}$). Left panel: correlation functions from Eq. (2.64) ($k = 1, 2, 3, 4, 5, 6$) on a $20^3 \times 40$ lattice with $\beta = 8$, $\kappa = 0.131$ and $\lambda = 0.0033$. Right panel: Effective masses of the correlation functions on the left. Note that $k = 4$ appears to reproduce the same energy level as $k = 3$ at a lattice energy of about 0.6.

2.6 Spectrum at the Physical Point

An ensemble of 20,000 configurations was created on a $20^3 \times 40$ lattice with $\beta = 8$, $\lambda = 0.0033$, and $\kappa = 0.131$ using the Monte Carlo methods described in Section 2.3. Operators were constructed for all $I(\Lambda^P)$ channels and for eight different smearing levels. Correlation matrices were calculated for each channel and analyzed using the variational method. Energy values (in lattice units) were obtained by a χ^2 fit.

Figure 2.10 shows the energy levels for isospins 0 and 1 as obtained from the gauge-invariant link operators $L^{\phi}_{\mu\nu\rho}$ and $L^{\alpha}_{\mu\nu\rho}$. Figure 2.11 shows the energy levels for isospin 0 as obtained from the Wilson loop and Polyakov loop operators. (Wilson/Polyakov loops cannot produce isospin 1). The gauge-invariant link was analyzed separately from the Wilson and Polykov loops to demonstrate the difference in the spectral content between these two sets of operators; the latter do not couple to the Higgs boson. A combined analysis did not reveal any new physics.

The lightest state in the spectrum has $I(\Lambda^P) = 1(T_1^-)$ corresponding to a single W boson. The mass is near 0.2 in lattice units (with a tiny statistical error) and identification with the experimentally known W mass allows an inference of the lattice spacing in physical units:

$$a = \frac{0.2}{m_W} = 0.5 \times 10^{-3} \text{ fm} \quad . \tag{2.69}$$

The next energy level above the single W has an energy near 0.3 and is observed in the $0(A_1^+)$ channel, and is interpreted as the Higgs boson. The lattice parameters were tuned to put this mass near the experimental value of 125 GeV; the result from the simulation is 122 ± 1 GeV. Notice that neither the single W boson nor the single Higgs boson is observed from the Wilson loop or Polyakov loop, but both are seen from the gauge-invariant link operators. Moreover, the Higgs boson H has not been created by just a single $\phi(x)$ but rather by gauge-invariant operators that can never contain any odd power of $\phi(x)$. Much like QCD, physical particles in the observed spectrum do not present any obvious linear one-to-one correspondence with fields in the Lagrangian. For a recent discussion in the context of a gauge-fixed lattice study, see Refs. [36, 37].

Continuing upward in energy within Figs. 2.10 and 2.11, there is a signal with energy

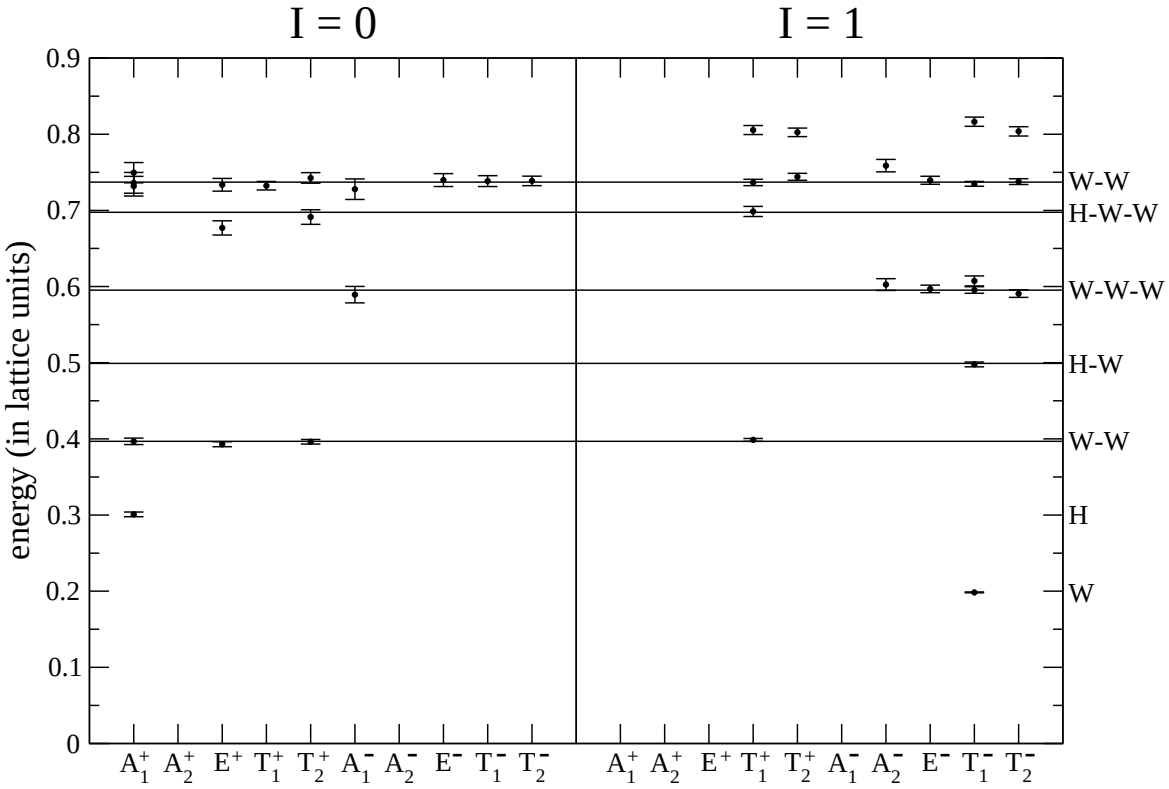

Figure 2.10: Energy spectrum extracted from correlation functions of the gauge-invariant link operators $L^{\phi}_{\mu\nu\rho}$ and $L^{\alpha}_{\mu\nu\rho}$ for all isoscalar and isovector channels on a $20^3 \times 40$ lattice with $\beta = 8$, $\kappa = 0.131$ and $\lambda = 0.0033$. These parameters put the theory very close to the experimental Higgs and W boson masses. Data points are lattice results with statistical bootstrap errors; horizontal lines are the expectations from Eq. (2.70).

at $2m_W$ in four specific channels: $0(A_1^+)$, $0(E^+)$, $0(T_2^+)$ and $1(T_1^+)$. These are exactly the four channels that correspond to the allowed quantum numbers of a pair of stationary W bosons. In the continuum, the wave function for such a pair of spin-1 W bosons would be the product of a spin part and an isospin part. The total wave function must be symmetric under particle interchange. This permits just two continuum states with isospin 0 [$0(0^+)$ and $0(2^+)$], and a single continuum state with isospin 1 [$1(1^+)$]. Note that the parity of a W pair is always positive in the absence of orbital angular momentum. Table 2.1 reveals that these continuum states match the lattice observations at energy $2m_W$ perfectly. An energy shift away from $2m_W$ would represent binding energy or a scattering state, but no shift is visible in the lattice simulation at this weak coupling value.

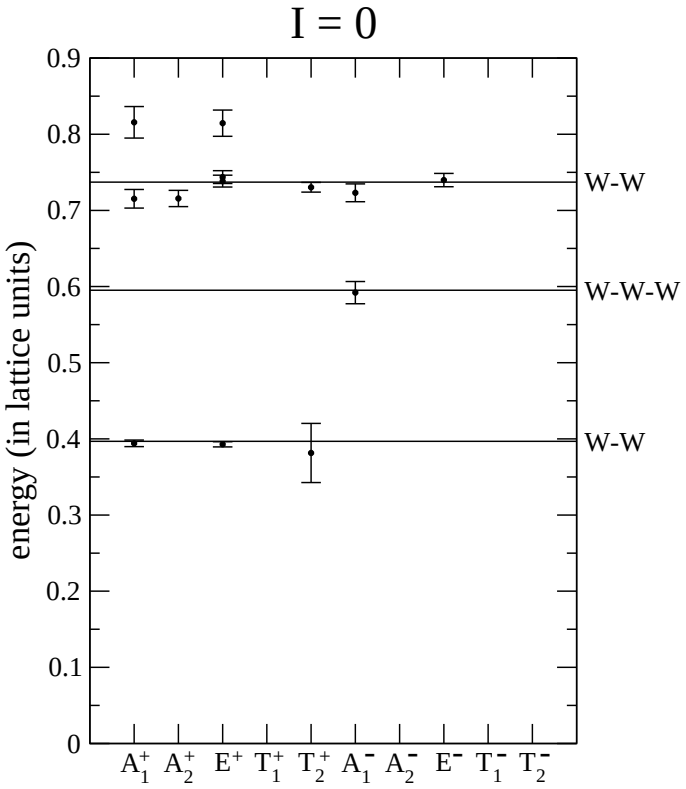

Figure 2.11: Energy spectrum extracted from correlation functions of the Wilson loop and Polyakov loop operators $W_{\mu\nu\rho}$ and $P_{\mu\nu\rho}$ for all isoscalar channels on a $20^3 \times 40$ lattice with $\beta = 8$, $\kappa = 0.131$ and $\lambda = 0.0033$. These parameters put the theory very close to the experimental Higgs and W boson masses. Data points are lattice results with statistical bootstrap errors; horizontal lines are the expectations from Eq. (2.70).

The next state in Figs. 2.10 and 2.11 has an energy of $m_H + m_W$ and is another pair of stationary bosons. Because the Higgs boson is $0(0^+)$, the Higgs-W pair should have the quantum numbers of the W. The lattice data show that the Higgs-W pair appears in exactly the same $I(\Lambda^P)$ channels as does the single W.

Two states are expected to appear with an energy near 0.6 because this corresponds to $2m_H \approx 3m_W$. A pair of stationary Higgs bosons should have the same quantum numbers as a single Higgs, i.e. $I(J^P) = 0(0^+)$, but no such signal appears in Figs. 2.10 and 2.11. To see this two-Higgs state requires a different creation operator; Sec. 2.9 introduces this operator and uses it to observe the two-Higgs state.

A collection of three stationary W bosons must have a wave function that is symmetric

under interchange of any pair, and must be built from a spin part and an isospin part. The $I = 0$ case has an antisymmetric isospin part and the only available antisymmetric spin part is $J = 0$. The $I = 1$ case is of mixed symmetry and can combine with $J = 1$, 2, or 3 (but not $J = 0$) to form a symmetric wave function. These continuum options, i.e., $0(0^-)$, $1(1^-)$, $1(2^-)$ and $1(3^-)$, can be converted into lattice channels using Table 2.1 and the result is precisely the list of channels observed in Figs. 2.10 and 2.11, i.e. $0(A_1^-)$, $1(T_1^-)$, $1(E^-)$, $1(T_2^-)$, and $1(A_2^-)$.

The next energy level is $m_H + 2m_W$, which should have identical $I(\Lambda^P)$ options to the pair of stationary W bosons discussed above. Figure 2.10 verifies this expectation, having signals for $0(A_1^+)$, $0(E^+)$, $0(T_2^+)$, and $1(T_1^+)$, although errors bars are somewhat larger for this high energy state.

The next energy level in Figs. 2.10 and 2.11 is a pair of moving W bosons with vanishing total momentum. Recall that these operators were defined to have zero total momentum, but this still permits a two-particle state where the particles have equal and opposite momenta. Momentum components along the x, y or z axes of the lattice can have integer multiple values of $2\pi/L$, where L is the spatial length of the lattice. The lattice dispersion relation for a boson with mass m and momentum $\vec{p}$ is

$$\sinh^2\left(\frac{aE(\vec{p})}{2}\right) = \sinh^2\left(\frac{am}{2}\right) + \sum_{i=1}^{3}\sin^2\left(\frac{ap_i}{2}\right) \quad , \tag{2.70}$$

which reduces to the continuum relation, $E(\vec{p}) = \sqrt{m^2 + \vec{p}^2}$, as the lattice spacing a goes to zero. Given the lattice spacing and statistical precision used here, the difference between Eq. (2.70) and the continuum relation is noticeable. The energy of a state of two noninteracting bosons is simply $E_1(\vec{p}_1) + E_2(\vec{p}_2)$, with energies from Eq. (2.70).

Two particles with relative motion can also have orbital angular momentum L; the allowed $I(J^P)$ for Higgs-Higgs, Higgs-W and W-W states are listed in Table 2.3. There is no way to specify L with lattice operators because it is not a conserved quantum number; only the total momentum J can be specified, which corresponds to Λ in a lattice simulation. For two moving W particles, all quantum numbers with $I = 0$ or 1 are possible except $0(0^-)$ and $1(0^+)$. Therefore a signal could appear in all $I(\Lambda^P)$ channels, even $0(A_1^-)$ and $1(A_1^+)$ because of $J = 4$ states. As evident from Figs. 2.10 and 2.11, the lattice simulation produced signals

Table 2.3: $I(J^P)$ quantum numbers for Higgs-Higgs, Higgs-W and W-W states with orbital angular momentum L. Higgs-Higgs states must have positive parity due to Bose statistics.

	Higgs-Higgs	Higgs-W	W-W	
L	$I=0$	$I=1$	$I=0$	$I=1$
0	0^+	1^-	0^+, 2^+	1^+
1	—	0^+, 1^+, 2^+	1^-, 2^-, 3^-	0^-, 1^-, 2^-
2	2^+	1^-, 2^-, 3^-	0^+, 1^+, 2^+, 3^+, 4^+	1^+, 2^+, 3^+
3	—	2^+, 3^+, 4^+	1^-, 2^-, 3^-, 4^-, 5^-	2^-, 3^-, 4^-
⋮	⋮	⋮	⋮	⋮

in many channels, but not in all. Section 2.9 provides the explanation for why this particular subset of channels did not show a signal.

This large energy is near the limit of the reach of this set of operators. A few data points are shown at even higher energies (in the neighborhood of $4m_W$) in Figs. 2.10 and 2.11, but a confident interpretation of those will require further computational effort that is presented in Secs. 2.7 and 2.8.

To conclude this section, it is interesting to notice a clear qualitative distinction between the Wilson/Polyakov loop operators and the gauge-invariant link operators: the former (Fig. 2.11) found only pure W boson states whereas the latter (Fig. 2.10) found additional states containing one Higgs boson. States containing two Higgs bosons must wait until Sec. 2.9.

2.7 Spectrum on a Larger Lattice

To confirm that several of the states in Figs. 2.10 and 2.11 are truly multiparticle states with linear momentum, the simulations of the previous section are repeated using a larger lattice volume. Since momentum on a lattice is given by integer multiples of $2\pi/L$, where L is the spatial length of the lattice, increasing the lattice volume should cause the energies of states with linear momentum to decrease by a predictable amount. Here the lattice parameters are

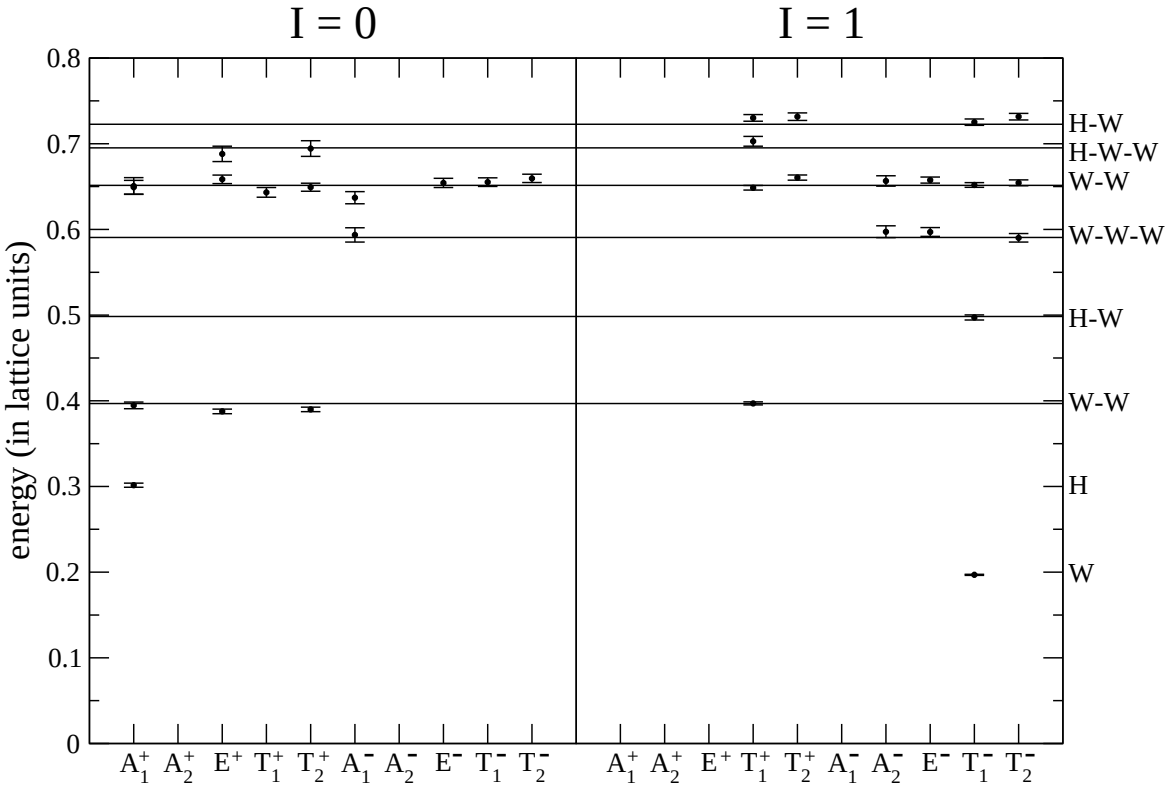

Figure 2.12: The same as Fig. 2.10 but using a $24^3 \times 48$ lattice.

set to $\beta = 8$, $\lambda = 0.0033$, $\kappa = 0.131$, which is the same as the previous section, but now the lattice volume is $24^3 \times 48$. An ensemble of 20,000 configurations is used.

The energy spectrum, extracted by a variational analysis, is shown in Figs. 2.12 and 2.13. The Higgs and W masses remain virtually unchanged, with a Higgs mass of 123 ± 1 GeV. This stability indicates that finite volume artifacts are negligible.

The data points that lie at 0.65 in lattice units correspond perfectly to two W particles with the minimal nonzero linear momentum. This physics appears in Figs. 2.10 and 2.11 at a larger energy, and the energy shift is in numerical agreement with the change in energy due to changing the lattice volume. Also, the four data points at 0.8 in Fig. 2.10 were numerically compatible with (a) a Higgs-W pair moving back-to-back with the minimal momentum or (b) a collection of four W bosons all at rest. This physics has energy 0.73 in Fig. 2.12, which implies that it cannot be a four-W state but is in good agreement with a back-to-back Higgs-W pair. From Table 2.3 all J^P quantum numbers except 0^- are allowed for a moving Higgs-W pair, but these lattice operators have found a signal in only a few channels.

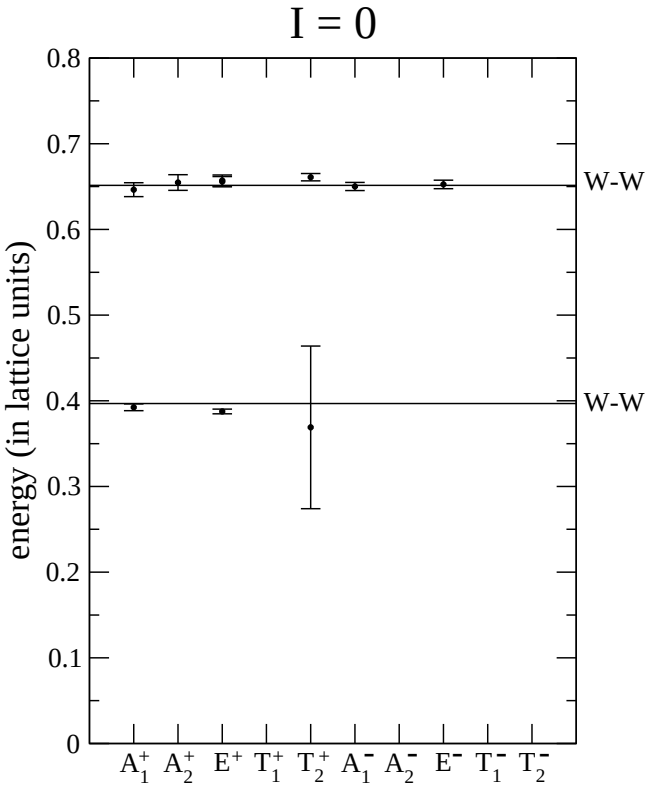

Figure 2.13: The same as Fig. 2.11 but using a $24^3 \times 48$ lattice.

Section 2.9 addresses the issue of missing irreducible representations for multiparticle states with momentum.

It is noteworthy that some states consisting of three stationary W particles, $1(T_1^-)$ in Fig. 2.12 and $0(A_1^-)$ in Fig. 2.13, as well as the $0(A_1^+)$ Higgs-W-W state in Fig. 2.12, were not detected in the larger lattice volume. This is because the variational analysis cannot resolve these states from the current basis of operators. When the lattice volume was increased, the spectral density increased as more multiparticle states became detectable in the correlation functions. As a result, states with a small overlap with the basis of operators could not be successfully extracted, even though they had been observed for the smaller lattice volume. Of course, these states could be seen again if the basis of operators was improved, for example, by increasing the number of operators.

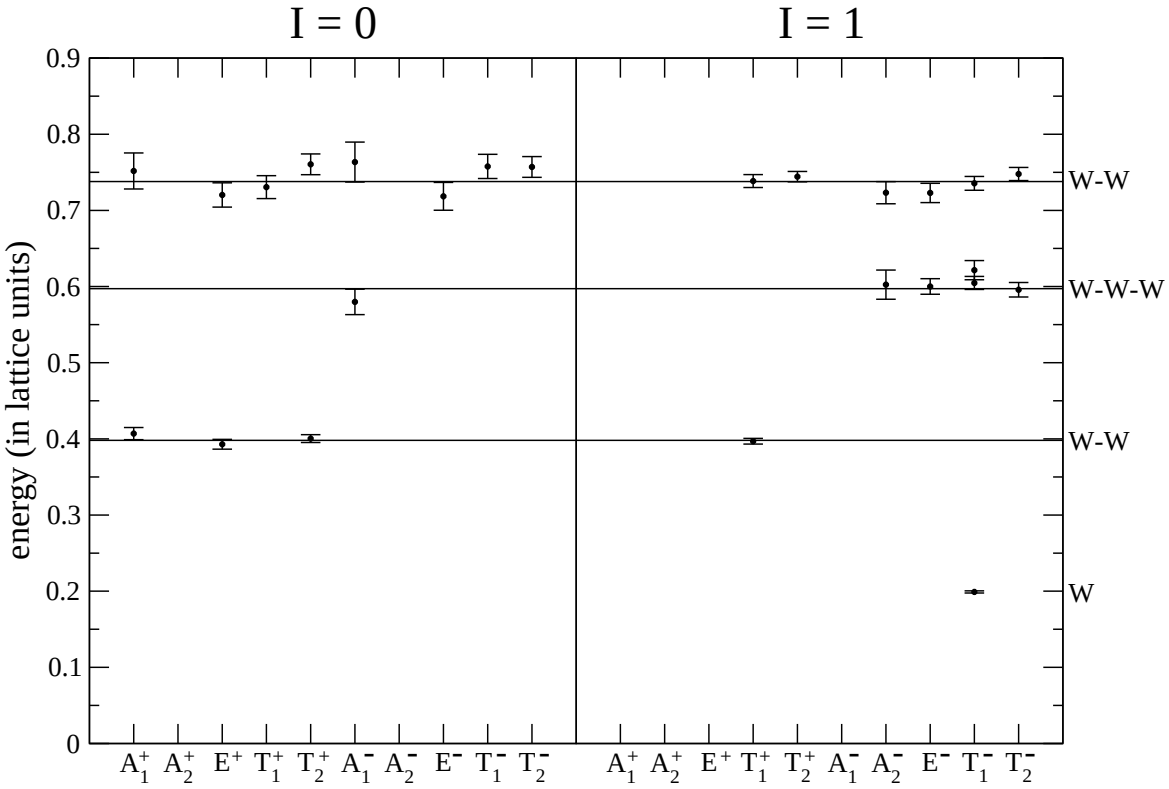

Figure 2.14: The same as Fig. 2.10 but using $\kappa = 0.40$ and $\lambda = \infty$. The Higgs mass is off the graph because of its large value.

2.8 Spectrum with a Heavy Higgs

A simple method to confirm which of the multiparticle states in Figs. 2.10 and 2.11 contain a Higgs boson is to change the Higgs mass and leave everything else unchanged. The extreme case of an infinite quartic coupling, corresponding to the maximal Higgs mass [26–28], is chosen. The lattice parameters are set to $\beta = 8$, $\lambda = \infty$, $\kappa = 0.40$, and the geometry is $20^3 \times 40$. An ensemble of 20,000 configurations is used. With these parameters, the W mass in lattice units is nearly identical to the value in Fig. 2.10.

The energy spectrum, extracted by a variational analysis, is shown in Figs. 2.14 and 2.15. The spectrum of states containing W particles remains essentially the same as in Figs. 2.10 and 2.11 but all states with Higgs content are no longer visible. In particular, states containing a Higgs and one or two W bosons have disappeared. This is consistent with the notion that the Higgs mass is now so large that all states with Higgs content have been pushed up to a higher energy scale.

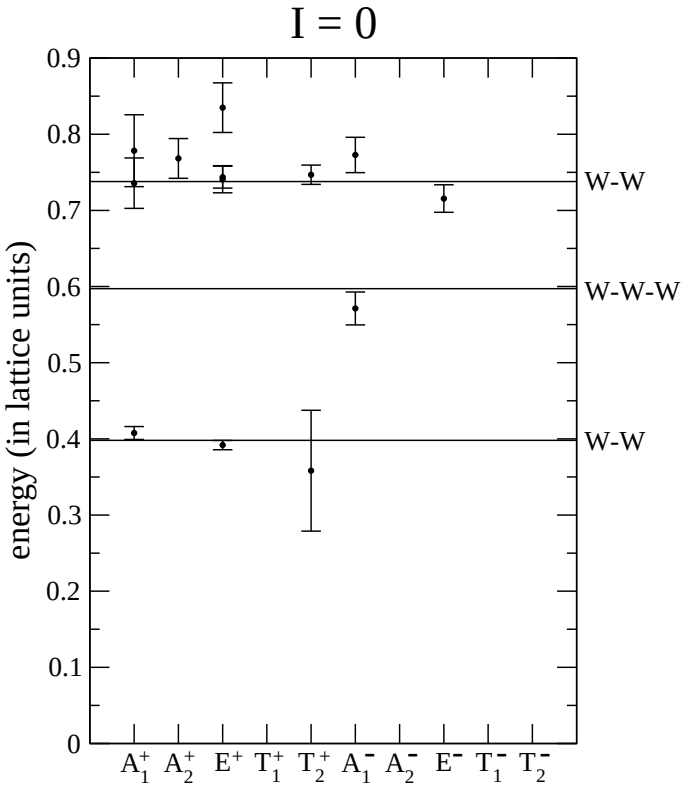

Figure 2.15: The same as Fig. 2.11 but using $\kappa = 0.40$ and $\lambda = \infty$.

To test this expectation of a large Higgs mass, a simultaneous fit of the entire $0(A_1^+)$ gauge-invariant-link correlation matrix was performed. (For a comparison of this method to the variational analysis in a different lattice context, see Ref. [91].) A three-state fit to time steps $t \geq 2$ provided a good description of the lattice data, with a χ^2/d.o.f. $= 0.84$. The smallest energy corresponds to a pair of stationary W bosons, the next energy is a pair of W bosons moving back-to-back with vanishing total momentum, and the third energy is 1.8 ± 0.2 in lattice units, which is 720 ± 70 GeV. This third energy is consistent with the maximal Higgs energy found in early lattice studies [26–28]. Lattice artifacts will be significant for this Higgs mass, since it is larger than unity in lattice units. For purposes of this study, it is sufficient to conclude that the Higgs mass is much larger than the low-lying spectrum of multiparticle W-boson states. The spectrum of a heavy-Higgs world reinforces the understanding of which states in the spectrum contain a Higgs boson.

2.9 Two-Particle Operators

The operators used in previous sections were, at most, quadratic in the field $\phi(x)$. They led to excellent results for several states in the SU(2)-Higgs spectrum, including multiboson states, but additional operators can accomplish even more. In particular, recall that the two-Higgs state was not observed in previous sections, the two-W state with internal linear momentum was missing from a few $I(\Lambda^P)$ channels, and the Higgs-W state with internal linear momentum was similarly missing from some $I(\Lambda^P)$ channels.

Presently, multiparticle operators will be constructed and the allowed irreducible representations will be compared to the results in Figs. 2.10 and 2.11. A two-particle operator $\mathcal{O}^{AB}(t)$ can be obtained by multiplying two operators with the following vacuum subtractions:

$$\mathcal{O}^{AB}(t) = \mathcal{O}^{A}(t)\mathcal{O}^{B}(t) - \left\langle \mathcal{O}^{A}(t)\mathcal{O}^{B}(t) \right\rangle \tag{2.71}$$

$$\mathcal{O}^{A}(t) = O^{A}(t) - \left\langle O^{A}(t) \right\rangle \tag{2.72}$$

$$\mathcal{O}^{B}(t) = O^{B}(t) - \left\langle O^{B}(t) \right\rangle \quad , \tag{2.73}$$

where $\mathcal{O}^{A}(t)$ and $\mathcal{O}^{B}(t)$ each couple predominantly to a single-particle state. The two-particle correlation function is then simply

$$C^{AB}(t) = \left\langle \mathcal{O}^{AB}(t)\mathcal{O}^{AB\dagger}(0) \right\rangle \quad . \tag{2.74}$$

Note that $\mathcal{O}^{AB}(t)$ is not strictly a two-particle operator because all states with the same quantum numbers as $\mathcal{O}^{AB}(t)$ can be created by it, including single-particle states. However, this construction will result in a much stronger overlap with the two-particle states, such as Higgs-Higgs, which was not found using the operators in Sec. 2.4.4. A three-particle operator is defined similarly:

$$\mathcal{O}^{ABC}(t) = \mathcal{O}^{A}(t)\mathcal{O}^{B}(t)\mathcal{O}^{C}(t) - \left\langle \mathcal{O}^{A}(t)\mathcal{O}^{B}(t)\mathcal{O}^{C}(t) \right\rangle \quad . \tag{2.75}$$

In this section the correlation function was written using the Hermitian conjugate because operators with nonzero momentum are used, whereas in the previous sections all operators were strictly Hermitian. This does not affect the variational method because all of the correlation functions are real; to be precise, the imaginary component of each correlation function is equal to zero within statistical fluctuations.

The single-particle operators for the Higgs and W boson are given by

$$H(\vec{p}) = \sum_{\vec{x}} \frac{1}{2} \mathrm{Tr}\left\{\phi^\dagger(x)\phi(x)\right\} \exp\left\{i\vec{p}\cdot\vec{x}\right\} \tag{2.76}$$

$$W^a_\mu(\vec{p}) = \sum_{\vec{x}} \frac{1}{2} \mathrm{Tr}\left\{-i\sigma^a\phi^\dagger(x)U_\mu(x)\phi(x+\hat{\mu})\right\} \exp\left\{i\vec{p}\cdot\left(\vec{x}+\tfrac{1}{2}\hat{\mu}\right)\right\} \quad , \tag{2.77}$$

where $\vec{p}$ is the momentum and has components given by integer multiples of $2\pi/L$ in the x, y or z directions, with L being the spatial length of the lattice. Combining the W operators requires some additional care due to the isospin indices. W-W eigenstates of I are obtained using the scalar and vector products

$$I = 0: \quad \vec{W}_\mu \cdot \vec{W}_\nu = W^a_\mu W^a_\nu \tag{2.78}$$

$$I = 1: \quad \vec{W}_\mu \times \vec{W}_\nu = \epsilon^{abc} W^b_\mu W^c_\nu \quad , \tag{2.79}$$

where the repeated a, b, c indices are summed. Combinations of W operators with I greater than one are not considered in this work. The irreducible representations of the W-W operators with $\vec{p} = \vec{0}$ are given by

$$0(A_1^+): \quad W^a_1 W^a_1 + W^a_2 W^a_2 + W^a_3 W^a_3 \tag{2.80}$$

$$0(E^+): \quad \frac{W^a_1 W^a_1 - W^a_2 W^a_2}{\sqrt{2}}, \frac{W^a_1 W^a_1 + W^a_2 W^a_2 - 2W^a_3 W^a_3}{\sqrt{6}} \tag{2.81}$$

$$0(T_2^+): \quad W^a_1 W^a_2, W^a_2 W^a_3, W^a_3 W^a_1 \tag{2.82}$$

$$1(T_1^+): \quad \epsilon^{abc} W^b_1 W^c_2, \epsilon^{abc} W^b_2 W^c_3, \epsilon^{abc} W^b_3 W^c_1 \quad , \tag{2.83}$$

which correspond to the allowed continuum spins. The isospin combinations for three W's with $I = 0$ or 1 are

$$I = 0: \quad \vec{W}_\mu \cdot \left(\vec{W}_\nu \times \vec{W}_\rho\right) = \epsilon^{abc} W^a_\mu W^b_\nu W^c_\rho \tag{2.84}$$

$$I = 1: \quad \vec{W}_\mu \left(\vec{W}_\nu \cdot \vec{W}_\rho\right) = W^a_\mu W^b_\nu W^b_\rho \tag{2.85}$$

$$I = 1: \quad \vec{W}_\mu \times \left(\vec{W}_\nu \times \vec{W}_\rho\right) = \epsilon^{abc}\epsilon^{cde} W^b_\mu W^d_\nu W^e_\rho \quad . \tag{2.86}$$

Another $I = 1$ triple-W operator may be formed by combining an $I = 2$ pair with the third W, but this is unnecessary for the present work.

Table 2.4 shows the multiplicities for Higgs-Higgs, Higgs-W, W-W and W-W-W operators built entirely of $\vec{p} = \vec{0}$ operators. The energy spectrum obtained from the two-boson operators

Table 2.4: Octahedral group multiplicities of Higgs-Higgs, Higgs-W, W-W and W-W-W operators built of the operators in Eqs. (2.76) and (2.77) with $\vec{p} = \vec{0}$. Repeated isospin indices a, b, c, d, e are summed, but Lorentz indices μ, ν, ρ are not. The indices μ, ν, ρ are not equal to one another. (Note that there is a typo in Ref. [42] with operator $W^a_\mu W^b_\nu W^b_\nu$.)

Operator	I	A_1^+	A_2^+	E^+	T_1^+	T_2^+	A_1^-	A_2^-	E^-	T_1^-	T_2^-
HH	0	1	0	0	0	0	0	0	0	0	0
HW^a_μ	1	0	0	0	0	0	0	0	0	1	0
$W^a_\mu W^a_\mu$	0	1	0	1	0	0	0	0	0	0	0
$W^a_\mu W^a_\nu$	0	0	0	0	0	1	0	0	0	0	0
$\epsilon^{abc} W^b_\mu W^c_\nu$	1	0	0	0	1	0	0	0	0	0	0
$\epsilon^{abc} W^a_\mu W^b_\nu W^c_\rho$	0	0	0	0	0	0	1	0	0	0	0
$W^a_\mu W^b_\mu W^b_\mu$	1	0	0	0	0	0	0	0	0	1	0
$W^a_\mu W^b_\mu W^b_\nu$	1	0	0	0	0	0	0	0	0	1	1
$W^a_\mu W^b_\nu W^b_\nu$	1	0	0	0	0	0	0	0	0	1	1
$W^a_\mu W^b_\nu W^b_\rho$	1	0	0	0	0	0	0	1	1	0	0
$\epsilon^{abc}\epsilon^{cde} W^b_\mu W^d_\mu W^e_\nu$	1	0	0	0	0	0	0	0	0	1	1
$\epsilon^{abc}\epsilon^{cde} W^b_\mu W^d_\nu W^e_\rho$	1	0	0	0	0	0	0	0	1	0	0

by variational analysis is displayed in Fig. 2.16. The two-Higgs state, absent until now, is seen quite precisely. The W-W and Higgs-W signals are also excellent. Even three-boson and four-boson states are observed. While the four-W states in Fig. 2.16 have the same energy as a Higgs-W state with momentum, a Higgs-W state cannot have isospin 0. Another success worth noticing is that the single Higgs does not appear at all and the single W couples only weakly; that is a success because the operators were intended to be multiparticle operators.

The operators $H(\vec{p})$ and $W^a_\mu(\vec{p})$ from Eqs. (2.76) and (2.77) were calculated for momenta given by $|\vec{p}| = 2\pi/L$, $|\vec{p}| = \sqrt{2}(2\pi/L)$ and $|\vec{p}| = \sqrt{3}(2\pi/L)$. Figure 2.17 shows the spectrum obtained from a variational analysis of the single Higgs and W operators versus momentum. Both Higgs and W operators contain an excited state that is a two-W state, where one W is stationary and the other has momentum. Notice that the two-W energy does not form a

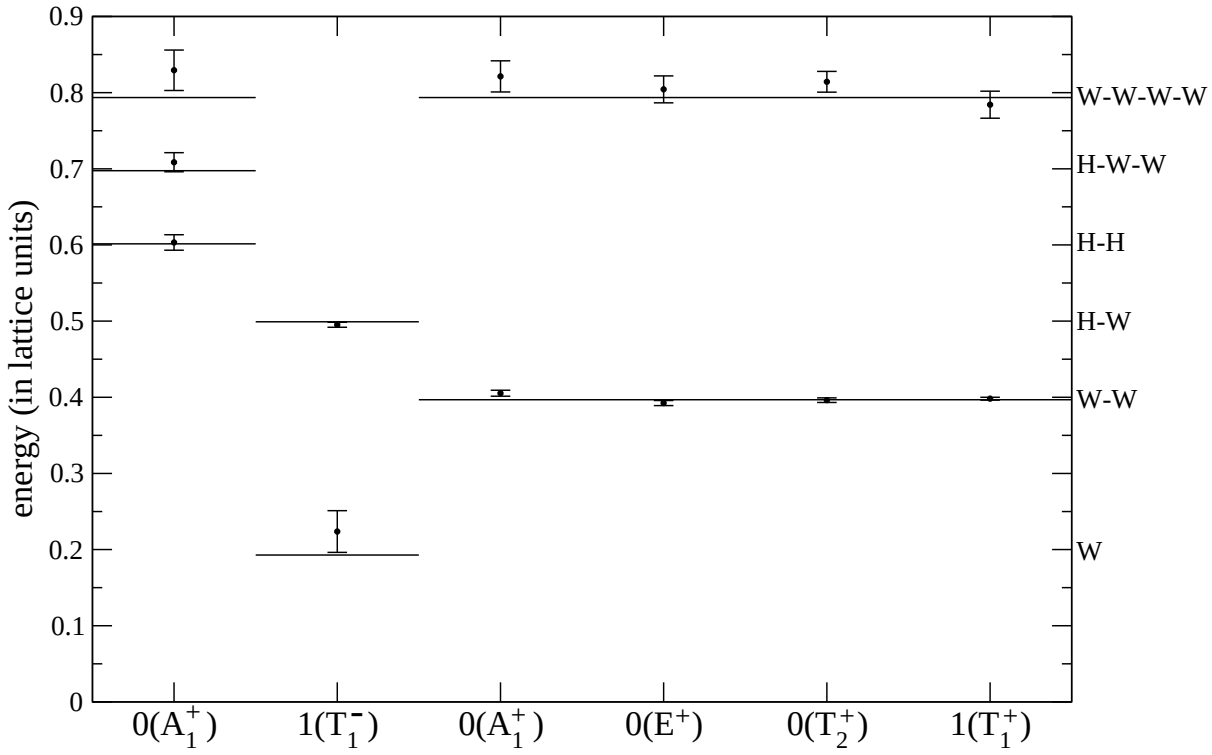

Figure 2.16: Energy spectrum extracted from correlation functions of Higgs-Higgs, Higgs-W and W-W operators built from Eqs. (2.76) and (2.77) with $\vec{p} = \vec{0}$ on a $20^3 \times 40$ lattice with $\beta = 8$, $\kappa = 0.131$ and $\lambda = 0.0033$. Data points are lattice results with statistical bootstrap errors; horizontal lines are the expectations from Eq. (2.70).

straight line since its continuum relation is $E = m + \sqrt{m^2 + \vec{p}^2}$.

Tables 2.5, 2.6 and 2.7 show the multiplicities for Higgs-Higgs, Higgs-W and W-W operators with the nonzero internal momentum, $|\vec{p}| = 2\pi/L$, $|\vec{p}| = \sqrt{2}(2\pi/L)$ and $|\vec{p}| = \sqrt{3}(2\pi/L)$, respectively. The list of allowed W-W representations for $|\vec{p}| = 2\pi/L$ agrees completely with the states that were found in Figs. 2.10 and 2.11. This shows why the W-W signal was absent from other channels in those graphs. In general, the direction of the internal momentum on the lattice will affect the allowed irreducible representations of multiparticle states [92, 93]. Application of the variational analysis to the two-Higgs, Higgs-W and two-W operators with back-to-back momenta $|\vec{p}| = 2\pi/L$, $|\vec{p}| = \sqrt{2}(2\pi/L)$ and $|\vec{p}| = \sqrt{3}(2\pi/L)$ produced Figs. 2.18 and 2.19.

The single-W states (near energy 0.2) and two-stationary-W states (near 0.4) were detected in a few channels but, as intended, these operators couple strongly to a pair with

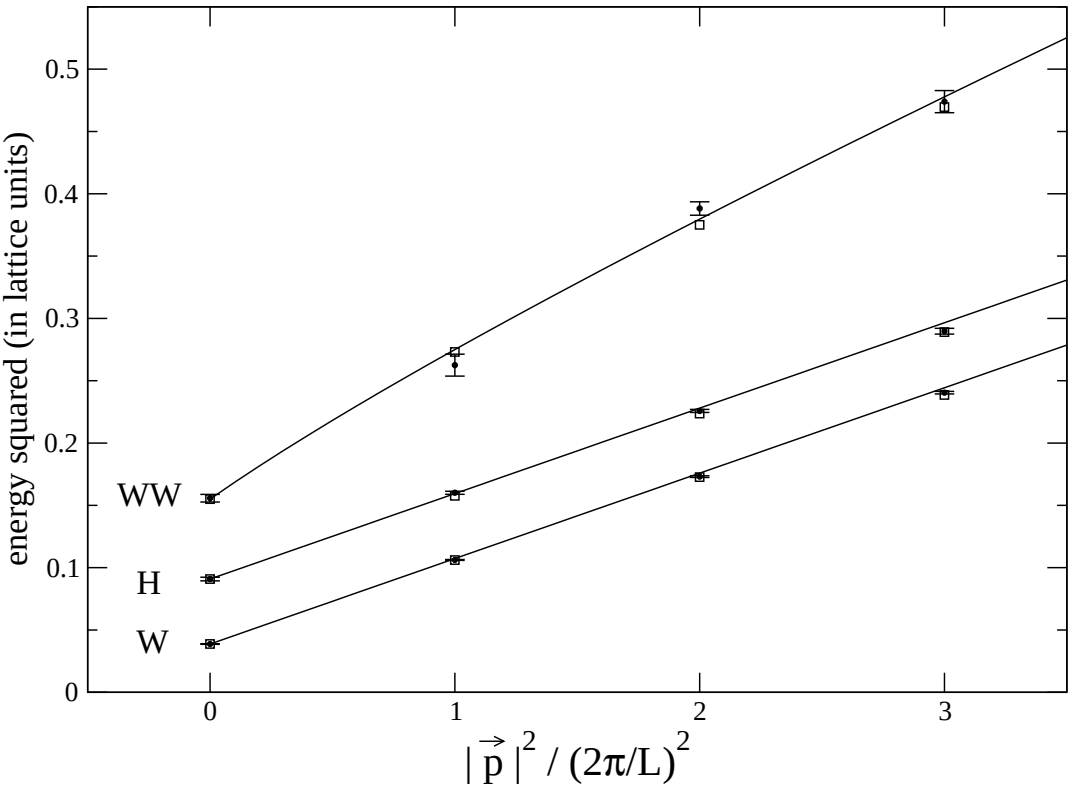

Figure 2.17: Energy spectrum extracted from correlation functions of $H(\vec{p})$ and $W^a(\vec{p})$ operators from Eqs. (2.76) and (2.77) as a function of momentum $\vec{p}$ on a $24^3 \times 48$ lattice with $\beta = 8$, $\kappa = 0.131$ and $\lambda = 0.0033$. Data points are lattice results with statistical bootstrap errors; solid curves are based on the continuum dispersion relation $E^2 = m^2 + \vec{p}^2$; empty boxes are the expectations from the lattice dispersion relation Eq. (2.70).

internal momentum. Comparison of Tables 2.5, 2.6 and 2.7 with Figs. 2.18 and 2.19 shows that signals are observed in precisely the expected subset of $I(\Lambda^P)$ channels in each case. Linear combinations of the two-Higgs, Higgs-W and two-W operators with back-to-back momentum corresponding the lattice irreps are listed in Appendix C.

Table 2.5: Octahedral group multiplicities of Higgs-Higgs, Higgs-W and W-W operators built of the operators in Eqs. (2.76) and (2.77) with $\vec{p} \neq \vec{0}$, where $\vec{p}_1 = \frac{2\pi}{L}(1,0,0)$, $\vec{p}_2 = \frac{2\pi}{L}(0,1,0)$ and $\vec{p}_3 = \frac{2\pi}{L}(0,0,1)$. Repeated isospin indices a, b, c are summed, but Lorentz indices μ, ν, ρ are not. The indices μ, ν, ρ are not equal to one another.

Operator	I	A_1^+	A_2^+	E^+	T_1^+	T_2^+	A_1^-	A_2^-	E^-	T_1^-	T_2^-
$H(\vec{p}_\mu)H(-\vec{p}_\mu)$	0	1	0	1	0	0	0	0	0	0	0
$H(\vec{p}_\mu)W_\mu^a(-\vec{p}_\mu)$	1	1	0	1	0	0	0	0	0	1	0
$H(\vec{p}_\mu)W_\nu^a(-\vec{p}_\mu)$	1	0	0	0	1	1	0	0	0	1	1
$W_\mu^a(\vec{p}_\mu)W_\mu^a(-\vec{p}_\mu)$	0	1	0	1	0	0	0	0	0	0	0
$W_\nu^a(\vec{p}_\mu)W_\nu^a(-\vec{p}_\mu)$	0	1	1	2	0	0	0	0	0	0	0
$W_\mu^a(\vec{p}_\mu)W_\nu^a(-\vec{p}_\mu)$	0	0	0	0	1	1	0	0	0	1	1
$W_\nu^a(\vec{p}_\mu)W_\rho^a(-\vec{p}_\mu)$	0	0	0	0	0	1	1	0	1	0	0
$\epsilon^{abc}W_\mu^b(\vec{p}_\mu)W_\mu^c(-\vec{p}_\mu)$	1	0	0	0	0	0	0	0	0	1	0
$\epsilon^{abc}W_\nu^b(\vec{p}_\mu)W_\nu^c(-\vec{p}_\mu)$	1	0	0	0	0	0	0	0	0	1	1
$\epsilon^{abc}W_\mu^b(\vec{p}_\mu)W_\nu^c(-\vec{p}_\mu)$	1	0	0	0	1	1	0	0	0	1	1
$\epsilon^{abc}W_\nu^b(\vec{p}_\mu)W_\rho^c(-\vec{p}_\mu)$	1	0	0	0	1	0	0	1	1	0	0

Table 2.6: Octahedral group multiplicities of Higgs-Higgs, Higgs-W and W-W operators built of the operators in Eqs. (2.76) and (2.77) with $\vec{p} \neq \vec{0}$, where $\vec{p}_{12} = \frac{2\pi}{L}(1,1,0)$, $\vec{p}_{23} = \frac{2\pi}{L}(0,1,1)$, $\vec{p}_{31} = \frac{2\pi}{L}(1,0,1)$, $\vec{p}_{1-2} = \frac{2\pi}{L}(1,-1,0)$, $\vec{p}_{2-3} = \frac{2\pi}{L}(0,1,-1)$ and $\vec{p}_{3-1} = \frac{2\pi}{L}(-1,0,1)$. Repeated isospin indices a, b, c are summed, but Lorentz indices μ, ν, ρ are not. The indices μ, ν, ρ are not equal to one another.

Operator	I	A_1^+	A_2^+	E^+	T_1^+	T_2^+	A_1^-	A_2^-	E^-	T_1^-	T_2^-
$H(\vec{p}_{\mu\nu})H(-\vec{p}_{\mu\nu})$	0	1	0	1	0	1	0	0	0	0	0
$H(\vec{p}_{\mu\nu})W_\mu^a(-\vec{p}_{\mu\nu})$	1	1	1	2	1	1	0	0	0	2	2
$H(\vec{p}_{\mu\nu})W_\rho^a(-\vec{p}_{\mu\nu})$	1	0	0	0	1	1	0	1	1	1	0
$W_\mu^a(\vec{p}_{\mu\nu})W_\mu^a(-\vec{p}_{\mu\nu})$	0	1	1	2	1	1	0	0	0	0	0
$W_\rho^a(\vec{p}_{\mu\nu})W_\rho^a(-\vec{p}_{\mu\nu})$	0	1	0	1	0	1	0	0	0	0	0
$W_\mu^a(\vec{p}_{\mu\nu})W_\nu^a(-\vec{p}_{\mu\nu})$	0	1	0	1	0	1	0	0	0	1	1
$W_\mu^a(\vec{p}_{\mu\nu})W_\rho^a(-\vec{p}_{\mu\nu})$	0	0	0	0	2	2	1	1	2	1	1
$\epsilon^{abc}W_\mu^b(\vec{p}_{\mu\nu})W_\mu^c(-\vec{p}_{\mu\nu})$	1	0	0	0	0	0	0	0	0	1	1
$\epsilon^{abc}W_\rho^b(\vec{p}_{\mu\nu})W_\rho^c(-\vec{p}_{\mu\nu})$	1	0	0	0	0	0	0	0	0	1	1
$\epsilon^{abc}W_\mu^b(\vec{p}_{\mu\nu})W_\nu^c(-\vec{p}_{\mu\nu})$	1	0	1	1	1	0	0	0	0	1	1
$\epsilon^{abc}W_\mu^b(\vec{p}_{\mu\nu})W_\rho^c(-\vec{p}_{\mu\nu})$	1	0	0	0	2	2	1	1	2	1	1

Table 2.7: Octahedral group multiplicities of Higgs-Higgs, Higgs-W and W-W operators built of the operators in Eqs. (2.76) and (2.77) with $\vec{p} \neq \vec{0}$, where $\vec{p}_{123} = \frac{2\pi}{L}(1,1,1)$, $\vec{p}_{-123} = \frac{2\pi}{L}(-1,1,1)$, $\vec{p}_{1-23} = \frac{2\pi}{L}(1,-1,1)$ and $\vec{p}_{12-3} = \frac{2\pi}{L}(1,1,-1)$. Repeated isospin indices a, b, c are summed, but Lorentz indices μ, ν, ρ are not. The indices μ, ν, ρ are not equal to one another.

Operator	I	A_1^+	A_2^+	E^+	T_1^+	T_2^+	A_1^-	A_2^-	E^-	T_1^-	T_2^-
$H(\vec{p}_{\mu\nu\rho})H(-\vec{p}_{\mu\nu\rho})$	0	1	0	0	0	1	0	0	0	0	0
$H(\vec{p}_{\mu\nu\rho})W_\mu^a(-\vec{p}_{\mu\nu\rho})$	1	1	0	1	1	2	0	1	1	2	1
$W_\mu^a(\vec{p}_{\mu\nu\rho})W_\mu^a(-\vec{p}_{\mu\nu\rho})$	0	1	0	1	1	2	0	0	0	0	0
$W_\mu^a(\vec{p}_{\mu\nu\rho})W_\nu^a(-\vec{p}_{\mu\nu\rho})$	0	1	0	1	1	2	1	0	1	1	2
$\epsilon^{abc}W_\mu^b(\vec{p}_{\mu\nu\rho})W_\mu^c(-\vec{p}_{\mu\nu\rho})$	1	0	0	0	0	0	0	1	1	2	1
$\epsilon^{abc}W_\mu^b(\vec{p}_{\mu\nu\rho})W_\nu^c(-\vec{p}_{\mu\nu\rho})$	1	0	1	1	2	1	0	1	1	2	1

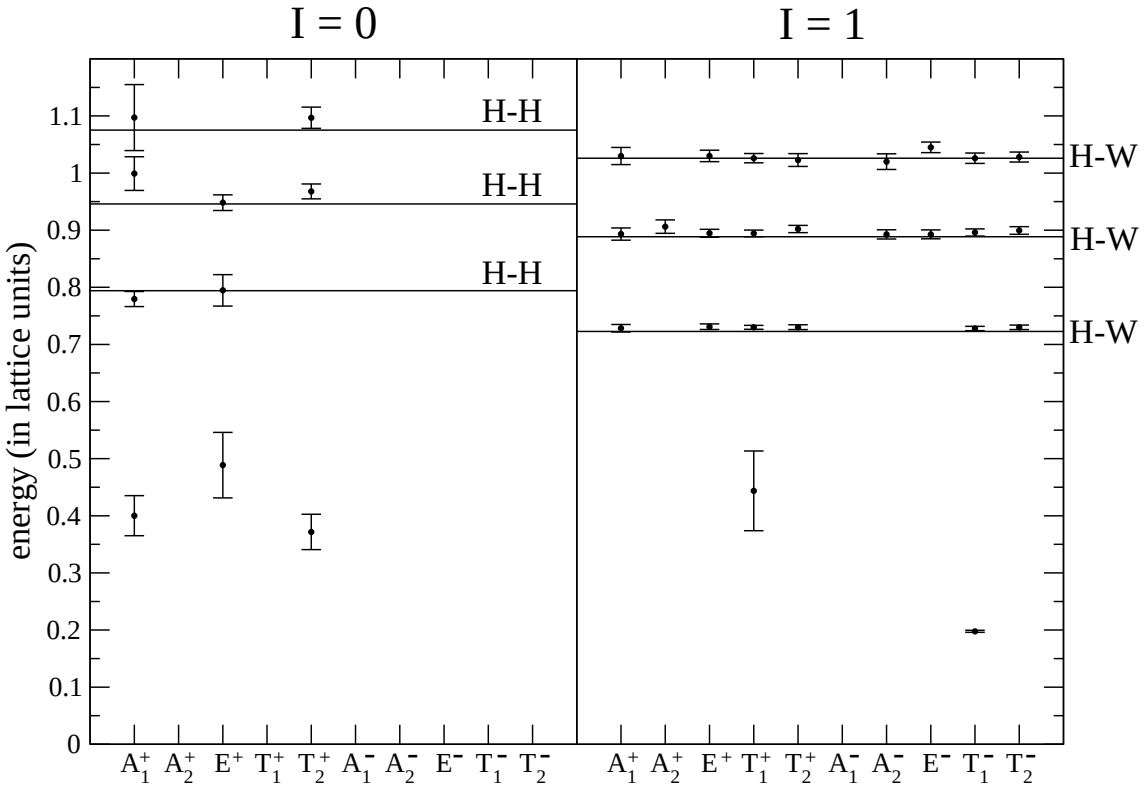

Figure 2.18: Energy spectrum extracted from correlation functions of Higgs-Higgs and Higgs-W operators built from Eqs. (2.76) and (2.77) with $|\vec{p}| = 2\pi/L$, $|\vec{p}| = \sqrt{2}(2\pi/L)$ and $|\vec{p}| = \sqrt{3}(2\pi/L)$ on a $24^3 \times 48$ lattice with $\beta = 8$, $\kappa = 0.131$ and $\lambda = 0.0033$. Data points are lattice results with statistical bootstrap errors; horizontal lines are the expectations from Eq. (2.70).

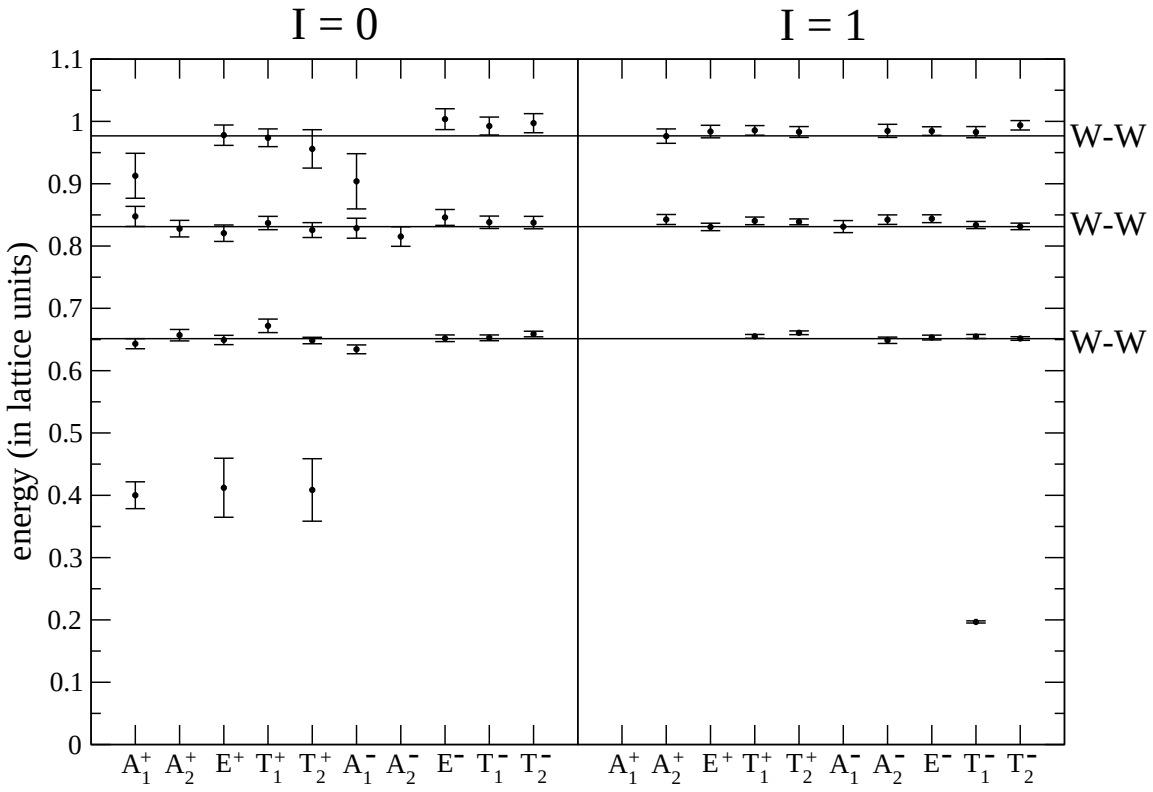

Figure 2.19: Energy spectrum extracted from correlation functions of W-W operators built from Eq. (2.77) with $|\vec{p}| = 2\pi/L$, $|\vec{p}| = \sqrt{2}(2\pi/L)$ and $|\vec{p}| = \sqrt{3}(2\pi/L)$ on a $24^3 \times 48$ lattice with $\beta = 8$, $\kappa = 0.131$ and $\lambda = 0.0033$. Data points are lattice results with statistical bootstrap errors; horizontal lines are the expectations from Eq. (2.70).

Chapter 3

Bottomonium and Bottom Meson Spectrum

3.1 Nonrelativistic QCD

For fermions whose mass M is greater than an energy cutoff Λ, the Dirac theory can be expanded in powers of $1/M$ by a Foldy-Wouthuysen-Tani transformation [94–97]

$$\begin{aligned}\overline{\Psi}\left(iD_\mu\gamma_\mu - M\right)\Psi = \psi^\dagger &\left(iD_t - M + \frac{\mathbf{D}^2}{2M} + \frac{\mathbf{D}^4}{8M^3} + \frac{g}{2M}\sigma\cdot\mathbf{B}\right)\psi \\ &+ \psi^\dagger\left(\frac{g}{8M^2}\left(\mathbf{D}\cdot\mathbf{E} - \mathbf{E}\cdot\mathbf{D}\right) + \frac{ig}{8M^2}\sigma\cdot\left(\mathbf{D}\times\mathbf{E} - \mathbf{E}\times\mathbf{D}\right)\right)\psi \\ &+ O\left(\frac{1}{M^3}\right) + \left\{\psi\leftrightarrow\chi, D_t\leftrightarrow -D_t, \mathbf{E}\leftrightarrow -\mathbf{E}\right\} \quad . \end{aligned} \tag{3.1}$$

This transformation systematically eliminates odd operators, which mix the upper and lower components of the Dirac spinor. It is then possible to separate the positive-energy and negative-energy eigenstates of Ψ in a nonrelativistic expansion. In Eq.(3.1), the particle ψ and anti-particle χ components of the spinor Ψ have been decoupled and interactions up to order $1/M^2$ are given in the expansion. For QCD, $\mathbf{E}$ and $\mathbf{B}$ are the chromo-electric and chromo-magnetic fields.

Whereas Ψ is a four-component spinor, the fields ψ and χ each have two components. A nonrelativistic basis of Dirac γ matrices allows the spin components of nonrelativistic and relativistic fermions to be contracted in a straightforward way. The choice of (Euclideanized) Dirac γ matrices used through this work is

$$\gamma_k = \begin{pmatrix} 0 & \sigma_k \\ \sigma_k & 0 \end{pmatrix} \qquad \gamma_4 = \begin{pmatrix} I & 0 \\ 0 & -I \end{pmatrix} \quad . \tag{3.2}$$

For forward (backward) time propagation, the top (bottom) two Dirac indices are contracted with the two nonrelativistic spin indices.

For heavy quarkonium, the relative importance of the expansion terms in Eq. (3.1) are determined by the dynamics of the hadron [64–66]. The magnitudes of the operators are estimated by the quark mass M and quark velocity v, as shown in Table 3.1. Since the typical kinetic energy of a bottom quark inside bottomonium is roughly the scale of QCD ($\Lambda_{\rm QCD} \sim 250$ MeV),

$$Mv^2 \sim 500 \text{ MeV} \quad , \tag{3.3}$$

and the bottom quark mass is about 4 GeV, the bottom quark velocity squared is about $v^2 \sim 0.1$. For heavy-light mesons, the quark velocity is not a good expansion parameter because the light quark is relativistic. Instead, $\Lambda_{\rm QCD}/M$ is the relevant expansion parameter.

Table 3.1: Estimated magnitudes of the field and derivative operators for a nonrelativistic action [66]. These apply to a heavy-heavy meson like bottomonium, but not to a heavy-light meson like the B meson.

Operator	Magnitude
ψ, χ	$(Mv)^{\frac{3}{2}}$
D_t	Mv^2
$\mathbf{D}$	Mv
$g\mathbf{E}$	M^2v^3
$g\mathbf{B}$	M^2v^4

Following from Eq. (3.1), the Lagrangian for a nonrelativistic fermion is given by

$$\mathcal{L}_{\rm NRQCD} = \psi^\dagger \left(iD_t - H\right) \psi \tag{3.4}$$

$$H = M - \frac{\mathbf{D}^2}{2M} - \frac{\mathbf{D}^4}{8M^3} - \frac{g}{2M}\sigma\cdot\mathbf{B} - \frac{g}{8M^2}\left(\mathbf{D}\cdot\mathbf{E} - \mathbf{E}\cdot\mathbf{D}\right) - \frac{ig}{8M^2}\sigma\cdot\left(\mathbf{D}\times\mathbf{E} - \mathbf{E}\times\mathbf{D}\right) + O\left(\frac{1}{M^3}\right) \quad , \tag{3.5}$$

where H is the nonrelativistic Hamiltonian expanded in powers of $1/M$. The constant mass term only corresponds to an overall energy shift and can be integrated out. This is because the rest mass is no longer a dynamical quantity in a nonrelativistic formulation. The equation of motion for the nonrelativistic fermion is given by the gauge-covariant Schrödinger equation

$$\left(iD_t - H\right)\psi = 0 \quad , \tag{3.6}$$

whose solution is given by the Green's function

$$G(t,\mathbf{x}) = \text{P.O.}\exp\left(-i\int_{t_0}^{t}\left(H(\tau,\mathbf{x}) + gA_t(\tau,\mathbf{x})\right)d\tau\right)G(t_0,\mathbf{x}) \quad , \tag{3.7}$$

where P.O. indicates path ordering of the time evolution operator. The fermion propagator is given by the Green's function above:

$$G(t,\mathbf{x};t_0,\mathbf{x}_0) = \overbrace{\psi(t,\mathbf{x})\psi^\dagger}(t_0,\mathbf{x}_0) \quad , \tag{3.8}$$

where $\psi^\dagger(t_0,\mathbf{x}_0)$ and $\psi(t,\mathbf{x})$ are the source and sink operators, respectively. The nonrelativistic fermion propagator is an initial value problem, where the initial value is given by

$$G(t_0,\mathbf{x}_0;t_0,\mathbf{x}_0) = G_0(t_0,\mathbf{x}_0) \quad . \tag{3.9}$$

In contrast, the relativistic propagator is a boundary value problem, solved by inverting the Dirac operator.

A consequence of the nonrelativistic expansion is that the theory is no longer renormalizable. All terms in the nonrelativistic expansion that have a coefficient with an inverse mass also contain higher dimensional operators, which are non-renormalizable. Higher order terms in the expansion take relativistic corrections into account, and are typically small as long as the energy cutoff Λ is not too large compared to the heavy mass M. As $\Lambda \to M$, the higher order terms grow and eventually diverge. At this point, the nonrelativistic theory is sick and only the relativistic theory, which contains all terms in the expansion, will remain predictive. When Λ grows large enough that pair production of the heavy fermions is relevant, it is intuitively expected that the nonrelativistic theory should fail. NRQCD is still a very useful effective field theory that gives reliable phenomological results for energy cutoffs less than the bottom quark mass.

Another aspect about the higher dimensional operators is that their coefficients receive significant renormalization effects. Although these operators are not renormalizable as $\Lambda \to \infty$, it is reasonable and practical to perturbatively renormalize them at cutoffs of around $\Lambda \sim M$. A large renormalization effect in practical lattice studies is from tadpole corrections to the bare gauge coupling. This effect severely affects the perturbative renormalization of lattice observables that contain gauge links. A very practical remedy is to divide the gauge links by

a mean-field tadpole correction u_0, often given by the fourth root of the average plaquette or the mean link in Landau gauge, and this dramatically reduces discretization effects [99, 100].

In addition to tadpoles, radiative corrections also modify the operator coefficients. For a cutoff much greater than $\Lambda_{\rm QCD}$, gluon loop corrections can be calculated from first principles by QCD perturbation theory. Alternatively, they can be tuned non-perturbatively by fixing physical observables, such as hadron masses, to their experimental values. For the present study of bottom quarks, effects from radiative corrections are small, though non-negligible.

3.2 Nonrelativistic Lattice QCD

Lattice simulations of relativistic bottom quarks are very difficult. Very fine lattice spacings and very large lattice box sizes are required to reduce discretization and finite-volume errors to a reasonable level. This comes from the requirements $aM_b < 1$ and $m_\pi L > 4$, which lead to lattice spacings of $a < 0.05\,\text{fm}$ and spatial lengths of $L > 5\,\text{fm}$. It follows that a minimum of about $L/a = 100$ points in each dimension are needed to fit relativistic bottom quarks on a lattice.

A nonrelativistic bottom quark can get around this problem. Because there is no longer a dynamical mass term, the requirement that aM_b be small is eliminated and much coarser lattice spacings may be used. A bonus of the nonrelativistic formulation is that a numerical lattice calculation is much more computationally efficient than the relativistic case. This is because a nonrelativistic propagator is solved as an initial value problem by time step evolution while a relativistic fermion propagator is solved as a boundary value problem by inverting the Dirac lattice operator.

On a Euclidean lattice, the time evolution of the NRQCD propagator can be given by

$$\begin{aligned} G(t+a,\mathbf{x}) = &\left(1 - \frac{aH_I(t+a,\mathbf{x})}{2}\right)\left(1 - \frac{aH_0(t+a,\mathbf{x})}{2n}\right)^n \frac{U_4^\dagger(t,\mathbf{x})}{u_0} \\ &\times \left(1 - \frac{aH_0(t,\mathbf{x})}{2n}\right)^n \left(1 - \frac{aH_I(t,\mathbf{x})}{2}\right) G(t,\mathbf{x}) \quad , \end{aligned} \tag{3.10}$$

where G is defined symmetrically with respect to forward or backward time propagation [98].

H_0 and H_I are the free and interacting Hamiltonians, respectively, and are given by

$$H_0 = -\frac{\Delta^{(2)}}{2M} \tag{3.11}$$

$$\begin{aligned} H_I = &- c_1\frac{(\Delta^{(2)})^2}{8M^3} + \frac{c_2}{u_0^4}\frac{ig}{8M^2}\left(\tilde{\Delta}\cdot\tilde{\mathbf{E}} - \tilde{\mathbf{E}}\cdot\tilde{\Delta}\right) - \frac{c_3}{u_0^4}\frac{g}{8M^2}\sigma\cdot\left(\tilde{\Delta}\times\tilde{\mathbf{E}} - \tilde{\mathbf{E}}\times\tilde{\Delta}\right) \\ &- \frac{c_4}{u_0^4}\frac{g}{2M}\sigma\cdot\tilde{\mathbf{B}} + c_5\frac{a^2\Delta^{(4)}}{24M} - c_6\frac{a(\Delta^{(2)})^2}{16nM^2} \quad , \end{aligned} \tag{3.12}$$

where Δ, $\Delta^{(2)}$ and $\Delta^{(4)}$ are gauge-covariant lattice derivatives. A tilde is used to distinguish operators and fields that have been improved by removing leading-order discretization errors. All of the gauge fields are explicitly divided by the tadpole correction u_0. The coefficients c_i are renormalization constants. At tree level $c_i = 1$ for all i, though radiative corrections modify them away from one. Radiatively corrected values of c_i are dependent on the type of gauge action, lattice cut-off, sea quark action and masses.

The improved chromoelectric and magnetic fields are related to a discretized version of the field strength tensor

$$\tilde{E}_i = \tilde{F}_{4i} \tag{3.13}$$

$$\tilde{B}_i = \frac{1}{2}\epsilon_{ijk}\tilde{F}_{jk} \tag{3.14}$$

$$\begin{aligned} \tilde{F}_{\mu\nu}(x) = &\frac{5}{3}F_{\mu\nu}(x) + \frac{1-u_0^2}{3u_0^2}F_{\mu\nu}(x) \\ &- \frac{1}{6u_0^2}\left[U_\mu(x)F_{\mu\nu}(x+\hat{\mu})U_\mu^\dagger(x) + U_\mu^\dagger(x-\hat{\mu})F_{\mu\nu}(x-\hat{\mu})U_\mu(x-\hat{\mu})\right. \\ &\left. + U_\nu(x)F_{\mu\nu}(x+\hat{\nu})U_\nu^\dagger(x) + U_\nu^\dagger(x-\hat{\nu})F_{\mu\nu}(x-\hat{\nu})U_\nu(x-\hat{\nu})\right] \quad , \end{aligned} \tag{3.15}$$

where Eq. (3.15) is given in Ref. [101]. The cloverleaf field $F_{\mu\nu}(x)$ is given by the sum of plaquettes $P_{\mu\nu}$ in the (μ,ν) plane that begin and end on the site x [66]:

$$\begin{aligned} gF_{\mu\nu}(x) = -\frac{1}{4u_0^4a^2}\big\{&\mathcal{I}[U_\mu(x)U_\nu(x+\hat{\mu})U_\mu^\dagger(x+\hat{\nu})U_\nu^\dagger(x)] \\ &+ \mathcal{I}[U_\nu(x)U_\mu^\dagger(x+\hat{\nu}-\hat{\mu})U_\nu^\dagger(x-\hat{\mu})U_\mu(x-\hat{\mu})] \\ &+ \mathcal{I}[U_\mu^\dagger(x-\hat{\mu})U_\nu^\dagger(x-\hat{\mu}-\hat{\nu})U_\mu(x-\hat{\mu}-\hat{\nu})U_\nu(x-\hat{\nu})] \\ &+ \mathcal{I}[U_\nu^\dagger(x-\hat{\nu})U_\mu(x-\hat{\nu})U_\nu(x-\hat{\nu}+\hat{\mu})U_\mu^\dagger(x)]\big\} \quad , \end{aligned} \tag{3.16}$$

where $\mathcal{I}$ is the (traceless) matrix analogue of an imaginary operator, given by

$$\mathcal{I}[P] = \frac{P-P^\dagger}{2i} - \frac{1}{3}\,\mathrm{Im}(\mathrm{Tr}\,P) \quad . \tag{3.17}$$

The basic discrete gauge-covariant spatial derivatives are given by

$$a\Delta_i G(x) = \frac{1}{2u_0}[U_i(x)G(x+\hat{i}) - U_i^\dagger(x-\hat{i})G(x-\hat{i})] \tag{3.18}$$

$$a\Delta_i^{(+)} G(x) = \frac{1}{u_0}U_i(x)G(x+\hat{i}) - G(x) \tag{3.19}$$

$$a\Delta_i^{(-)} G(x) = G(x) - \frac{1}{u_0}U_i^\dagger(x-\hat{i})G(x-\hat{i}) \tag{3.20}$$

$$a^2\Delta_i^{(2)} G(x) = \frac{1}{u_0}U_i(x)G(x+\hat{i}) - 2G(x) + \frac{1}{u_0}U_i^\dagger(x-\hat{i})G(x-\hat{i}) \quad , \tag{3.21}$$

where the first three are central, forward and backward first derivatives, respectively, and the last is a second derivative. Improved first derivative and Laplacian operators are given below

$$\tilde{\Delta}_i = \Delta_i - \frac{a^2}{6}\Delta_i^{(+)}\Delta_i\Delta_i^{(-)} \tag{3.22}$$

$$\Delta^{(2)} = \sum_{i=1}^{3}\Delta_i^{(2)} \tag{3.23}$$

$$\tilde{\Delta}^{(2)} = \Delta^{(2)} - \frac{a^2}{12}\Delta^{(4)} \tag{3.24}$$

$$\Delta^{(4)} = \sum_{i=1}^{3}\left(\Delta_i^{(2)}\right)^2 \quad . \tag{3.25}$$

3.3 Dynamical Gauge Action

Generating an ensemble of gauge fields with dynamical fermions by Monte Carlo is a computationally expensive feat. The required computer time increases as the lattice spacing and the quark mass decrease. Currently, only a few collaborations worldwide have the computational resources to create QCD ensembles on fine lattices ($a < 0.1$ fm) with physical pion masses ($m_\pi \sim 140$ MeV).

The gauge field ensemble used in this study was generated by the PACS-CS collaboration [102] and made publicly available on the Japan Lattice DataGrid. They used an improved action to reduce discretization effects. Improved gauge actions contain six-sided closed loops,

such as a rectangle, in addition to the basic four-sided plaquette

$$S_{\text{gauge}} = \beta \Big(c_0 \sum(\text{plaquette}) + c_1 \sum(\text{rectangle}) \\ + c_2 \sum(\text{chair-loop}) + c_3 \sum(\text{twisted-loop}) \Big) \quad . \tag{3.26}$$

The coefficients c_i may be chosen arbitrarily, but must satisfy the normalization condition $c_0 + 8c_1 + 16c_2 + 8c_3 = 1$. This ensures that as $a \to 0$ the correct continuum action is recovered. The Iwasaki gauge action [103, 104] has a rectangle term with $c_1 = -0.331$ and $c_0 = 1 - 8c_1 = 3.648$; all other coefficients are set to zero. It is expressed as

$$S_{\text{Iwasaki}}[U] = \beta \sum_x \Bigg\{ c_0 \sum_{\mu<\nu} \frac{1}{3} \operatorname{Re}\operatorname{Tr}\left[1 - U_\mu(x) U_\nu(x+\hat{\mu}) U_\mu^\dagger(x+\hat{\nu}) U_\nu^\dagger(x)\right] \\ + c_1 \sum_{\mu\neq\nu} \frac{1}{3} \operatorname{Re}\operatorname{Tr}\left[1 - U_\mu(x) U_\mu(x+\hat{\mu}) U_\nu(x+2\hat{\mu}) U_\mu^\dagger(x+\hat{\mu}+\hat{\nu}) U_\mu^\dagger(x+\hat{\nu}) U_\nu^\dagger(x)\right] \Bigg\} \quad . \tag{3.27}$$

The clover-improved Wilson action [105] is used for the dynamical fermions, and is given by

$$S_{\text{Wilson}}[U, \Psi] = \sum_x \Bigg\{ \overline{\Psi}(x)\Psi(x) - \kappa\, c_{\text{SW}} \sum_{\mu,\nu} \frac{i}{2} \overline{\Psi}(x) \sigma_{\mu\nu} F_{\mu\nu}(x) \Psi(x) \\ - \kappa \sum_\mu \left(\overline{\Psi}(x)(1-\gamma_\mu) U_\mu(x) \Psi(x+\hat{\mu}) + \overline{\Psi}(x)(1+\gamma_\mu) U_\mu^\dagger(x-\hat{\mu}) \Psi(x-\hat{\mu}) \right) \Bigg\} \quad , \tag{3.28}$$

where $\sigma_{\mu\nu} = \frac{1}{2}[\gamma_\mu, \gamma_\nu]$ and the anti-symmetric field strength tensor is given by the clover-leaf sum of plaquettes

$$F_{\mu\nu}(x) = \frac{1}{4} \times \frac{1}{2i} \Big\{ U_\mu(x) U_\nu(x+\hat{\mu}) U_\mu^\dagger(x+\hat{\nu}) U_\nu^\dagger(x) \\ + U_\nu(x) U_\mu^\dagger(x+\hat{\nu}-\hat{\mu}) U_\nu^\dagger(x-\hat{\mu}) U_\mu(x-\hat{\mu}) \\ + U_\mu^\dagger(x-\hat{\mu}) U_\nu^\dagger(x-\hat{\mu}-\hat{\nu}) U_\mu(x-\hat{\mu}-\hat{\nu}) U_\nu(x-\hat{\nu}) \\ + U_\nu^\dagger(x-\hat{\nu}) U_\mu(x-\hat{\nu}) U_\nu(x-\hat{\nu}+\hat{\mu}) U_\mu^\dagger(x) \\ - \text{h.c.} \Big\} \quad . \tag{3.29}$$

Wilson fermions avoid the famous fermion doubling problem but at the cost of breaking chiral symmetry. The Sheikholeslami-Wohlert term, also called the clover term, allows for systematic $O(a)$-improvement of discretization errors by tuning the c_{SW} coefficient. Setting c_{SW} to zero gives back the basic Wilson fermion action.

3.4 Free-Form Smearing

3.4.1 Quark Smearing and Spectroscopy

Hadron spectroscopy is the study of the masses of bound states of quarks. Lattice QCD allows computer simulations from first principles. While the quantum numbers of the operator can be chosen to select which states contribute to the correlation function, all states with the correct quantum numbers can appear. For example, an operator with $J^{PC} = 0^{-+}$ containing a bottom quark and an anti-bottom quark couples to the bottomonium ground state η_b, but it also couples to the radially excited $\eta_b(2S)$, $\eta_b(3S)$ and higher excited states. In the limit as the time separation of the correlation function goes to infinity, the ground state dominates and is the only state to contribute. For a practical calculation, the ground state may not dominate before the signal-to-noise ratio degrades, and all usable data points contain a mixture of states. A detailed choice of the operator shape and size, implemented through quark smearing, can improve the signal for the state of interest.

3.4.2 Previous Quark Smearing Methods

Quark smearing is a technique used frequently in lattice spectroscopy to improve the signal obtained from correlation functions. The idea is to smear the quarks into a shape that resembles the wavefunction of the bound state. A popular method is to smear the quark field into a Gaussian shape by iteratively applying the discrete gauge-covariant Laplacian operator Δ as given by

$$\tilde{\psi}(x) = \left[1 + \frac{\alpha}{n}\Delta\right]^n \psi(x) \quad , \tag{3.30}$$

where n is the number of iterations and α is the smearing parameter [84–86]. Note that the field is only smeared in the spatial directions and not the temporal direction. The name Gaussian smearing is used because, in the free field theory, as the number of iterations n goes to infinity the operator approaches a Gaussian shape. To see this, consider how Gaussian

smearing acts in the quark three-momentum:

$$\lim_{n\to\infty}\left[1+\frac{\alpha}{n}\Delta\right]^n\psi(\mathbf{x})=e^{\alpha\Delta}\psi(\mathbf{x})=\sum_{\mathbf{k}}e^{-\alpha\mathbf{k}^2}\psi(\mathbf{k})e^{i\mathbf{x}\cdot\mathbf{k}} \quad . \tag{3.31}$$

If the original quark field is located at single point, i.e. $\psi(x)=\delta(x)\Rightarrow\psi(k)=1$, then the smeared quark field takes the Gaussian form

$$\tilde{\psi}(\mathbf{x})=\left(\frac{\pi}{\alpha}\right)^{3/2}\exp\left(\frac{-\mathbf{x}^2}{4\alpha}\right) \quad . \tag{3.32}$$

This approach is straightforward to implement, improves the ground state signal and suppresses excited states.

Another smearing method that is commonly used in NRQCD is to fix the gauge links to Coulomb gauge and explicitly give the quark field an arbitrary shape [44] using the formula

$$\tilde{\psi}(x)=\sum_{y}f(x-y)\,\psi(y) \quad . \tag{3.33}$$

The function $f(x-y)$ can be tuned to obtain optimal signals for not just the ground state, but for excited states as well. By choosing a shape that closely matches the wave function of an excited state, the ground state can be suppressed and a cleaner excited-state signal obtained. The convolution can be efficiently implemented by a fast fourier transform, and gauge fixing is required because Eq. (3.33) is not gauge invariant.

3.4.3 Free-form Smearing

Free-form smearing [69] combines the advantages of the previous methods. It allows the quark field to be smeared to an arbritary shape while retaining gauge invariance, without the need for gauge fixing. Free-form smearing was initially applied to relativistic quarks, but in this work it is applied for the first time to nonrelativistic heavy quarks. In the initial study of free-form smearing applied to bottomonium, a reduction in statistical errors relative to the gauge fixed method was observed [67].

This section will review the original procedure of free-form smearing [69], and then introduce a new version for improved computational speed. The quark field $\psi(x)$ at a single point x is Gaussian smeared as in Eq. (3.30) so that gauge links reach from point x to all other

spatial sites y on a given time slice. The free-form smeared field is given by the reweighting formula

$$\tilde{\tilde{\psi}}(x) = \sum_y f(x-y) \frac{\tilde{\psi}_x(y)}{\left\langle \left\| \tilde{\psi}_x(y) \right\| \right\rangle} \quad , \tag{3.34}$$

where $f(x-y)$ is an arbitrary function, $\tilde{\psi}_x(y)$ is the component of a Gaussian smeared field, which gauge transforms at x with the quark field ψ located at y, and $\left\langle \left\| \tilde{\psi}_x(y) \right\| \right\rangle$ is the ensemble average of the norm of the Gaussian smeared field. The norm is defined as

$$\left\| \tilde{\psi}_x(y) \right\| = \sqrt{\mathrm{Tr}\left(\tilde{\psi}_x^\dagger(y) \tilde{\psi}_x(y) \right)} \quad , \tag{3.35}$$

where the trace is over spin and color indices. Note that the Gaussian smeared field $\tilde{\psi}(x)$ in Eq. (3.30) is obtained from $\tilde{\psi}_x(y)$ by summing over y. Any number of free-form smeared fields $\tilde{\tilde{\psi}}(x)$ can be generated by reusing the same field $\tilde{\psi}_x(y)$ and choosing a different shape $f(x-y)$.

Free-form smearing is fairly insensitive to the Gaussian smearing parameters α and n. The parameter n should be chosen large enough so that gauge links reach every spatial lattice site, and α must be chosen so that $\frac{\alpha}{n} < \frac{1}{6}$, above which Gaussian smearing breaks down. For a lattice with L sites in each of the spatial directions, $n = \frac{3}{2}L$ Gaussian smearing steps are required to cover all sites. This large number of Gaussian smearing steps is a computational burden for the current form of free-form smearing. A significant disadvantage of free-form smearing in this form is that it is not computationally feasible to apply it at the sink. The reason is that one is required to smear every point x separately and then perform a summation to obtain a momentum projection.

A much more computationally efficient alternative to the Gaussian version of free-form smearing is to construct all shortest link paths from a point to all other spatial lattice sites. Recall that Gaussian smearing generates many link paths from a point to all other spatial sites, but that the links are also multiplied by a factor $\frac{\alpha}{n}$, which must be less than 1/6. Therefore, since the Gaussian method multiplies the links by a small factor, the shortest links tend to dominate.

The new free-form link algorithm starts at a point x and multiplies links outward to all nearest neighbours, and then again to all of their nearest outward neighbours, as illustrated in

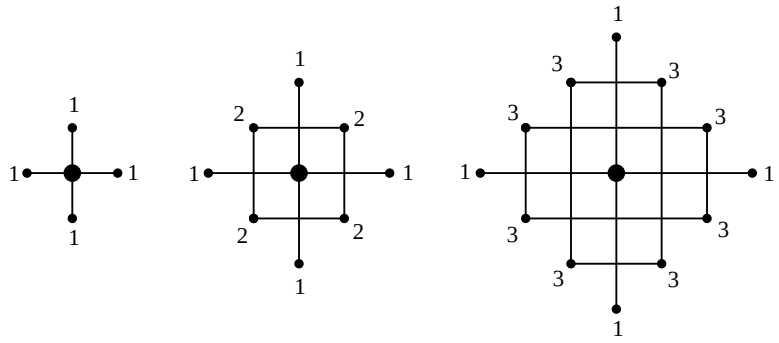

Figure 3.1: Illustration of the minimal-path method of free-form smearing in two dimensions. The first, second and third iterations are shown from left to right, respectively. The source position is in the center of each sketch and links are multiplied outwards iteratively, forming a shell. Different link paths that come to the same site are summed; the number of minimal paths for each site is indicated.

Fig. 3.1.[1] Different link paths that lead to the same point are added together, thus resulting in a sum of shortest link paths. This continues until all spatial sites have been reached and every link has been multiplied exactly once. The result is all shortest link paths from the original point x to all other spatial sites y,

$$\tilde{\psi}_x(y) = \sum_{\text{shortest paths}} U(x \to y)\psi(y) \quad . \tag{3.36}$$

The algorithm to compute the minimal paths of links is presented below in Alg. 1. Free-form smearing can then be implemented as in Eq. (3.34). Whereas the Gaussian version of free-form smearing requires $O(L^4)$ number of link multiplications, the shortest link method uses $3L^3$ link multiplications, which is exactly the number of spatial links on a given time slice – the minimal number of link multipications.

Link smearing can also be used prior to the Gaussian smearing or shortest-link step. Stout link smearing is used with parameters $\rho = 0.15$ and $n_\rho = 10$ as defined in Ref. [83]. Therefore, the shortest-link method actually uses the shortest path of stout links, which effectively contains longer link paths as well. Link smearing was useful in reducing some excited-state contamination, although the most significant improvements where made by

[1]Note the number of shortest paths shown in Fig. 3.1 for the case of two-dimensions are given by the binomial coefficients. For the actual three-dimensional case, the number of shortest paths are given by the trinomial coefficients.

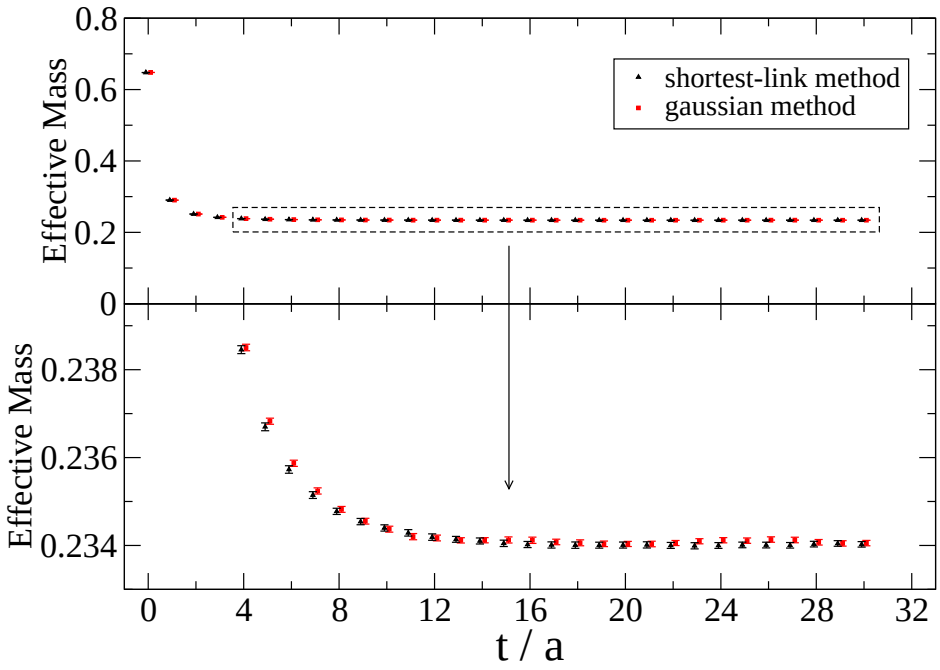

Figure 3.2: Comparison of effective masses for the Gaussian and shortest-link methods of free-form smearing, using the same function $f(x-y)$, applied to the bottomonium pseudoscalar. The bottom panel shows a close-up view of the ground-state plateau. The shortest-link method is much more computationally efficient.

careful selection of the smearing shape $f(x-y)$.

Figure 3.2 shows a direct comparison of the Gaussian and shortest-link free-form smearing methods for the effective mass of a bottomonium S-wave correlation function. The same wave-function shape $f(x-y)$ and stout-link smearings were used in both cases. In addition, the Gaussian smearing parameters used were $n = 64$ and $\alpha = 0.15$ from Eq. (3.30). There is virtually no difference between the results of the two methods shown in Fig. 3.2. Given the same function $f(x-y)$, the differences between the two methods are generally small and what slight differences can be found (e.g., in a P-wave correlation function) are only an issue of fine-tuning in $f(x-y)$.

For the present study, smearing the field over the whole spatial volume is appropriate since the volume is not very much larger than the hadron size. This also conforms to the way Gaussian smearing, wave-function smearing and the original free-form smearing have been done in the past [44, 69, 84–86].

Algorithm 1 The minimal-path algorithm to compute $\tilde{\psi}_x(y)$ of Eq. (3.36).

sitevisited = false
linkvisited = false
$\tilde{\psi} = 0$
$\tilde{\psi}(x) = 1$
sitevisited(x) = true
$y_{\text{frontier}}(1) = x$
$n = 1$
while $n > 0$ **do**
  $n_{\text{new}} = 0$
  for $i = 1, n$ **do**
    $y = y_{\text{frontier}}(i)$
    for $\mu = 1, 3$ **do**
      Forward direction
      if linkvisited(μ, y) = false **then**
        $\tilde{\psi}(y + \mu) = \tilde{\psi}(y + \mu) + U_\mu^\dagger(y)\tilde{\psi}(y)$
        linkvisited(μ, y) = true
        if sitevisited$(y + \mu)$ = false **then**
          sitevisited$(y + \mu)$ = true
          $n_{\text{new}} = n_{\text{new}} + 1$
          $y_{\text{new frontier}}(n_{\text{new}}) = y + \mu$
        end if
      end if
      Backward direction, essentially $\mu \to -\mu$
      if linkvisited$(\mu, y - \hat{\mu})$ = false **then**
        $\tilde{\psi}(y - \mu) = \tilde{\psi}(y - \mu) + U_\mu(y - \mu)\tilde{\psi}(y)$
        linkvisited(μ, y) = true
        if sitevisited$(y - \mu)$ = false **then**
          sitevisited$(y - \mu)$ = true
          $n_{\text{new}} = n_{\text{new}} + 1$
          $y_{\text{new frontier}}(n_{\text{new}}) = y - \mu$
        end if
      end if
    end for
  end for
  $n = n_{\text{new}}$
  $y_{\text{frontier}} = y_{\text{new frontier}}$
end while

3.5 Free-form Smeared Operators

For this study, smearing is applied to the bottom quark, leaving the antiquark unsmeared. This is expedient because the bottom-quark propagator is obtained from lattice NRQCD and is less computationally expensive than the relativistic propagators for the up/down, strange and charm quarks. For bottomonium, the resulting wave function places an anti-bottom quark at the origin surrounded by a bottom quark. For bottom mesons, an anti-up/down, anti-strange or anti-charm quark is surrounded by a bottom quark. A physically intuitive picture would instead place the center of mass at the origin, but, since a zero-momentum projection of the meson is taken, the location of the center of mass is irrelevant; only the distance between the quark and antiquark matters.

Hydrogen-like (i.e., Coulomb potential) wave-function shapes have been used successfully within the gauge-fixed smearing method in lattice NRQCD [44] and they are used here with free-form smearing as well. Different shapes are used depending on the intended orbital angular momentum, and nodes are included to optimize the operator for radial excitations. Here is a list of the basic smearing shapes used in this paper:

$$\text{S-wave:} \quad f(x-y) = \begin{cases} e^{-\frac{r}{a_0}} \\ e^{-\frac{r}{a_0}}\,(r-b) \\ e^{-\frac{r}{a_0}}\,(r-c)(r-b) \end{cases} \tag{3.37}$$

$$\text{P-wave:} \quad f_i(x-y) = \begin{cases} e^{-\frac{r}{a_0}}\,\tilde{x}_i \\ e^{-\frac{r}{a_0}}\,\tilde{x}_i\,(r-b) \end{cases} \tag{3.38}$$

$$\text{D-wave:} \quad f_{ij}(x-y) = \begin{cases} e^{-\frac{r}{a_0}}\,(\tilde{x}_i\tilde{x}_j - \frac{1}{3}\delta_{ij}(\tilde{x}_1^2+\tilde{x}_2^2+\tilde{x}_3^2)) \\ e^{-\frac{r}{a_0}}\,(\tilde{x}_i\tilde{x}_j - \frac{1}{3}\delta_{ij}(\tilde{x}_1^2+\tilde{x}_2^2+\tilde{x}_3^2))\,(r-b) \end{cases} \tag{3.39}$$

$$\text{F-wave:} \quad f_{ijk}(x-y) = \tilde{x}_i\tilde{x}_j\tilde{x}_k\,e^{-\frac{r}{a_0}} \tag{3.40}$$

$$\text{G-wave:} \quad f_{ijkl}(x-y) = \tilde{x}_i\tilde{x}_j\tilde{x}_k\tilde{x}_l\,e^{-\frac{r}{a_0}} \quad , \tag{3.41}$$

where $\tilde{x}_i$ is defined to be periodic, but r is simply defined as the shortest distance between

sites x and y in a periodic box,

$$r = \sqrt{(x_1 - y_1)^2_{\min} + (x_2 - y_2)^2_{\min} + (x_3 - y_3)^2_{\min}} \tag{3.42}$$

$$\tilde{x}_i = \sin\left(\frac{2\pi(x_i - y_i)}{L}\right) \quad . \tag{3.43}$$

The radius and nodal parameters (a_0, b, c) are tuned to optimize the signal of the ground-state or radial excitations. Free-form smeared operators are built according to

$$\chi(x)\tilde{\tilde{\psi}}(x) = \chi(x)\sum_y \Omega_f(x-y)\frac{\tilde{\psi}_x(y)}{\left\langle \left\| \tilde{\psi}_x(y) \right\| \right\rangle} \quad , \tag{3.44}$$

where ψ is the quark, χ is the antiquark and $\Omega_f(x-y)$ is the free-form operator. Table 3.2 lists all operators used in this paper by their lattice irreducible representations and continuum quantum numbers. It provides a thorough coverage of quantum numbers for S, P and D waves plus five operators that offer the simplest exploration of some of the F and G waves. As explained in Ref. [51], additional F and G operators would duplicate some of the Λ^{PC} quantum numbers that already exist in this table, so they are omitted here. Sink operators are unsmeared and are given by the covariant derivative operators listed in Tables II and III of Ref. [51].

Table 3.2: The factor Ω_f that defines the quantum numbers of the operator in Eq. (3.44) and incorporates the free-form smearing functions from Eqs. (3.37)–(3.41). Column 2 shows only the J value that is expected to dominate in each case.

Λ^{PC}	J^{PC}	$^{2S+1}L_J$	Ω_f
A_1^{-+}	0^{-+}	$^1S_0$	f
T_1^{--}	1^{--}	$^3S_1$	$\{f\sigma_1, f\sigma_2, f\sigma_3\}$
T_1^{+-}	1^{+-}	$^1P_1$	$\{f_1, f_2, f_3\}$
A_1^{++}	0^{++}	$^3P_0$	$f_1\sigma_1 + f_2\sigma_2 + f_3\sigma_3$
T_1^{++}	1^{++}	$^3P_1$	$\{f_2\sigma_3 - f_3\sigma_2\, f_3\sigma_1 - f_1\sigma_3, f_1\sigma_2 - f_2\sigma_1\}$
E^{++}	2^{++}	$^3P_2$	$\{(f_1\sigma_1 - f_2\sigma_2)/\sqrt{2}, (f_1\sigma_1 + f_2\sigma_2 - 2f_3\sigma_3)/\sqrt{6}\}$
T_2^{++}	2^{++}	$^3P_2$	$\{f_2\sigma_3 + f_3\sigma_2, f_3\sigma_1 + f_1\sigma_3, f_1\sigma_2 + f_2\sigma_1\}$
E^{-+}	2^{-+}	$^1D_2$	$\{(f_{11} - f_{22})/\sqrt{2}, (f_{11} + f_{22} - 2f_{33})/\sqrt{6}\}$
T_2^{-+}	2^{-+}	$^1D_2$	$\{f_{23}, f_{31}, f_{12}\}$
T_1^{--}	1^{--}	$^3D_1$	$\{f_{11}\sigma_1 + f_{12}\sigma_2 + f_{13}\sigma_3, f_{21}\sigma_2 + f_{22}\sigma_2 + f_{23}\sigma_3,$ $f_{31}\sigma_1 + f_{32}\sigma_2 + f_{33}\sigma_3\}$
E^{--}	2^{--}	$^3D_2$	$\{(f_{23}\sigma_1 - f_{13}\sigma_2)/\sqrt{2}, (f_{23}\sigma_1 + f_{31}\sigma_2 - 2f_{12}\sigma_3)/\sqrt{6}\}$
T_2^{--}	2^{--}	$^3D_2$	$\{(f_{22} - f_{33})\sigma_1 + f_{13}\sigma_3 - f_{12}\sigma_2, (f_{33} - f_{11})\sigma_2 + f_{21}\sigma_1 - f_{23}\sigma_3,$ $(f_{11} - f_{22})\sigma_3 + f_{32}\sigma_2 - f_{31}\sigma_1\}$
A_2^{--}	3^{--}	$^3D_3$	$f_{12}\sigma_3 + f_{23}\sigma_1 + f_{31}\sigma_2$
T_1^{--}	3^{--}	$^3D_3$	$\{3f_{11}\sigma_1 - 2f_{12}\sigma_2 - 2f_{13}\sigma_3, 3f_{22}\sigma_2 - 2f_{23}\sigma_3 - 2f_{21}\sigma_1,$ $3f_{33}\sigma_3 - 2f_{31}\sigma_1 - 2f_{32}\sigma_2\}$
T_2^{--}	3^{--}	$^3D_3$	$\{(f_{22} - f_{33})\sigma_1 + 2f_{12}\sigma_2 - 2f_{13}\sigma_3, (f_{33} - f_{11})\sigma_2 + f_{23}\sigma_3 - 2f_{21}\sigma_1,$ $(f_{11} - f_{22})\sigma_3 + 2f_{31}\sigma_1 - 2f_{32}\sigma_2\}$
A_2^{+-}	3^{+-}	$^1F_3$	f_{123}
T_2^{+-}	3^{+-}	$^3F_3$	$\{f_{122} - f_{133}, f_{233} - f_{211}, f_{311} - f_{322}\}$
A_2^{++}	3^{++}	$^3F_3$	$(f_{221} - f_{331})\sigma_1 + (f_{332} - f_{112})\sigma_2 + (f_{113} - f_{223})\sigma_3$
T_1^{-+}	4^{-+}	$^1G_4$	$\{f_{2223} - f_{3332}, f_{3331} - f_{1113}, f_{1112} - f_{2221}\}$
A_1^{--}	4^{--}	$^3G_4$	$(f_{2223} - f_{3332})\sigma_1 + (f_{3331} - f_{1113})\sigma_2 + (f_{1112} - f_{2221})\sigma_3$

The optimized free-form smearing parameters corresponding to Eqs. (3.37)–(3.41) used in this study are given in Table 3.3. The parameters (a_0, b, c) are tuned by hand to optimize

Table 3.3: Free-form smearing parameters for B, B_s, B_c and bottomonium. Parameters were optimized by trial and error. In addition, nonoptimal parameters ($a_0 = 0.5$ and 1.0) are used for B, B_s and B_c, as well as unsmeared operators for bottomonium, as discussed in the text.

bottomonium				B_c			B_s			B		
L	a_0	b	c	L	a_0	b	L	a_0	b	L	a_0	b
S	1.4			S	0.5		S	0.5		S	0.5	
	1.6				2.0			4.5			5.0	
	2.6	2.6			2.2			5.8	5.8		5.5	
	2.8	2.8			4.0	4.0		6.0	6.0		6.2	6.2
	3.0	2.13	6.0	P	1.0		P	1.0		P	0.5	
P	2.0				3.0			6.0			7.0	
	3.0	4.6			4.0	6.0		7.0				
D	2.5			D	1.0							
	3.5	6.5			5.0							
F	3.0											
	4.0											
G	4.0											
	5.0											

the signal in a correlation function for the ground state, the first excited state and, for bottomonium S-waves, the second excited state. These optimizations improve the accuracy and precision of the spectrum. The effective mass plots shown in Figs. 3.3 and 3.4 demonstrate the effectiveness of free-form smearing to obtain clean signals for ground states and excited states. Figure 3.3 shows that the plateau begins at small Euclidean times for a bottomonium D-wave ground state and for the first radial excitation. In particular, note that the effective mass for the first radial excitation shows no contamination from the ground state. Similarly, Fig. 3.4 shows small-time plateaus for B_c meson S-wave, P-wave and D-wave ground states.

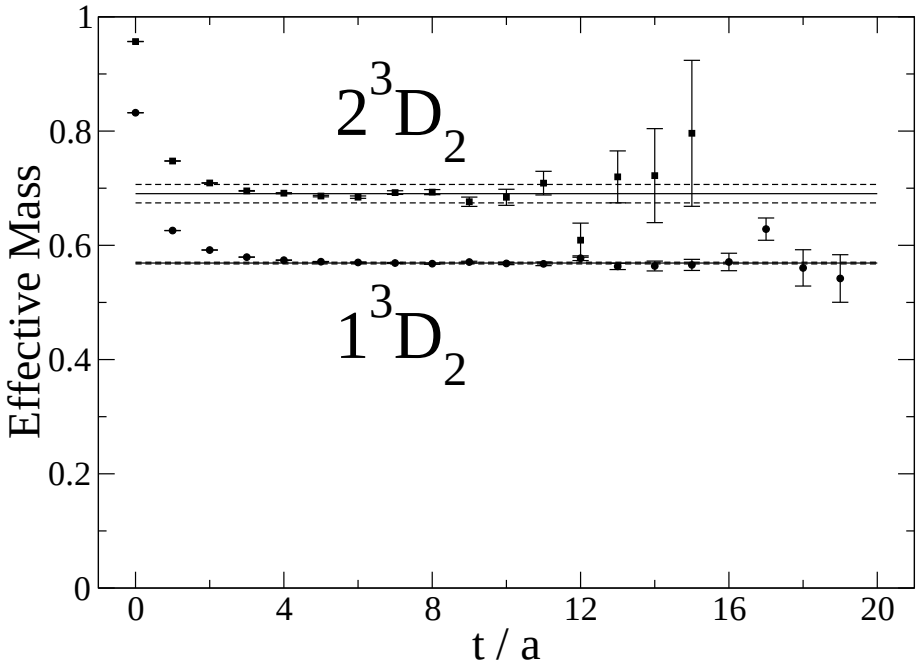

Figure 3.3: Effective mass plots for the free-form smeared ${}^3D_2$ (E^{--} representation) bottomonium correlation functions tuned to optimize the ground state and the first excited state. Energy values extracted from fits to the correlation functions are shown as solid horizontal lines. Dashed horizontal lines are the statistical bootstrap uncertainties.

Free-form smearing shrinks the contamination from unwanted states, thereby emphasizing the one state of interest, but it does not eliminate the contamination entirely. Different choices for the smearing parameters can be used to emphasize each state separately, and then a simultaneous fit to several correlation functions will be stable and reliable. For the present work, nonoptimized correlation functions are also included in the multistate fits and they further stabilize the results. For bottomonium, the nonoptimized correlators are calculated using unsmeared operators as given in Tables II and III of [51]. For B, B_s and B_c ground-state profiles, small radial parameters $a_0 = 0.5$ or $a_0 = 1.0$ are used as the nonoptimized choices.

Chronologically, the calculation for B_c was started before the minimal-path method had been developed, so it uses the Gaussian version of free-form smearing with parameters $n = 64$ and $\alpha = 0.15$ from Eq. (3.30). The minimal-path method of free-form smearing is used for all B, B_s and bottomonium calculations. Throughout this work, stout links with parameters

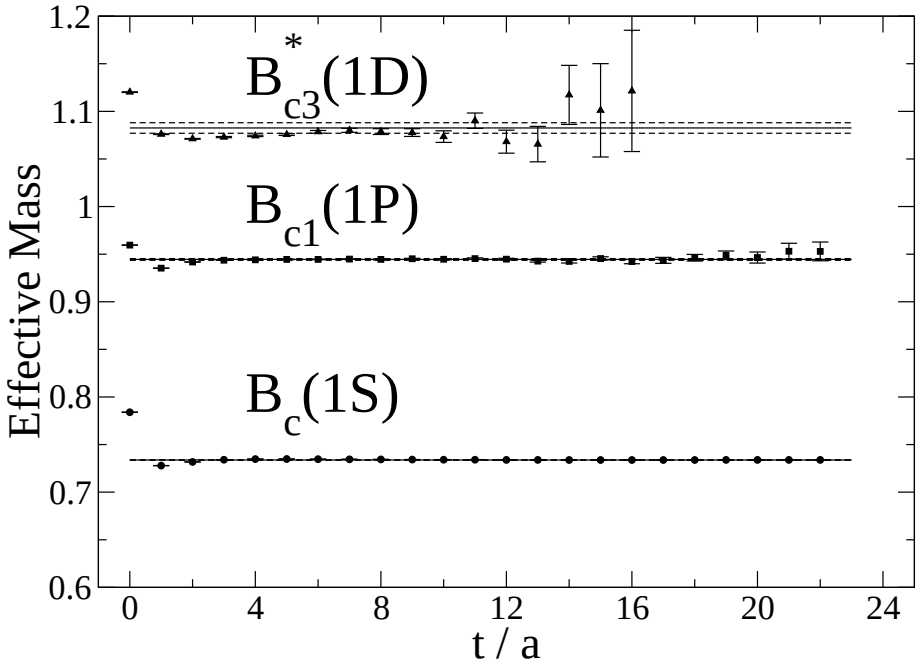

Figure 3.4: Effective mass plots for the free-form smeared 0^-, 1^+ and 3^- (T_2^- representation) B_c meson correlation functions tuned to optimize the S-wave, P-wave and D-wave ground states. The P-wave operator shown corresponds to 1^{++} when applied to quarkonium; see Sec. 3.9 for discussion on this operator when applied to heavy-light mesons. Energy values extracted from fits to the correlation functions are shown as solid horizontal lines. Dashed horizontal lines are the statistical bootstrap uncertainties.

$\rho = 0.15$ and $n_\rho = 10$ were employed.

3.6 Simulation Details

An $N_f = 2 + 1$ gauge field ensemble from the PACS-CS Collaboration [102] was used for this study. The action contains an Iwasaki gauge term and clover-improved Wilson fermions. The lattice dimensions are $32^3 \times 64$ and the lattice spacing

$$a_{\mathrm{PACS-CS}} = 0.0907(13) \text{ fm} \tag{3.45}$$

was determined by the PACS-CS Collaboration [102] using the experimental π, K and Ω masses. The pion mass is near physical at $m_\pi = 156(7)$ MeV. At $(m_K)_{\mathrm{orig}} = 554(8)$ MeV, the kaon mass is larger than its physical value so, to account for this, a partially quenched

Table 3.4: The hopping parameters and clover coefficients for relativistic sea and valence quarks.

sea quark	κ	c_{SW}
up/down	0.13781	1.715
strange	0.13640	1.715
valence quark	κ	c_{SW}
up/down	0.13781	1.715
strange	0.13666	1.715
charm	0.12686	1.64978

strange quark is used in this study as was done in Ref. [106] where the valence strange quark was retuned to match the physical ϕ mass, giving a kaon mass of $m_K = 504(7)$ MeV.

The charm quark parameters are taken from Ref. [106] where they were tuned using the Fermilab interpretation. The parameters for the relativistic quarks are given in Table 3.4. The propagators for the relativistic valence quarks $(u/d, s, c)$ are calculated using the sap_gcr solver from the DD-HMC code made available by Martin Lüscher [72–74].

The bottom quark is implemented using lattice NRQCD, including terms up to $O(v^4)$ in the bottom-quark velocity, which corresponds to $c_i = 1$ for $1 \leq i \leq 6$ and $c_i = 0$ for $i \geq 7$ according to the notation of the Appendix in Ref. [98]. Following Ref. [51], the bare mass of the bottom quark ($M_b = 1.95$) is taken from fitting the kinetic mass of the Υ to its experimental value, the tadpole factor is set to the average link in Landau gauge ($u_L = 0.8463$), and the stability parameter is chosen to be $n = 4$.

The calculation of correlation functions for bottom mesons with a nonrelativistic bottom quark requires some additional care with regard to the contraction of spin indices. The choice for Dirac γ matrices is

$$\gamma_k = \begin{pmatrix} 0 & \sigma_k \\ \sigma_k & 0 \end{pmatrix} \qquad \gamma_4 = \begin{pmatrix} I & 0 \\ 0 & -I \end{pmatrix} \quad , \tag{3.46}$$

which allows the Dirac indices of the relativistic propagator and the Pauli indices of the nonrelativistic propagator to be contracted in a simple manner. For forward time propagation the top two Dirac indices are used, while for backward time propagation the bottom two Dirac

indices are used.

Simulating multiple sources on a given configuration can reduce statistical errors. A random $U(1)$ wall source imitates multiple sources at different spatial sites on a given time slice without the need to calculate many propagators. While it is easily implemented using the conventional smearing methods given by Eqs. (3.30) and (3.33), a free-form smeared random wall source is computationally expensive because every site x must be smeared independently and summed according to the formula

$$\tilde{\tilde{\psi}}_W = \sum_i^N e^{i\theta_W(x_i)}\, \tilde{\tilde{\psi}}(x_i) \quad . \tag{3.47}$$

An efficient approach is to calculate a partial random wall source, where only a relatively small number of spatial sites x is used. For this study the partial wall source has $N = 4^3$ evenly spaced free-form smeared sites. Including more sites in the partial wall source did not improve the statistical errors for the case of bottomonium [67]. Statistical errors are further reduced by using partial wall sources for multiple time slices. For bottomonium a partial wall source is built for each of the 64 time slices, and for the B, B_s and B_c mesons a partial wall source is built for 32 time slices. To further increase the statistics, NRQCD propagators are calculated forward and backward in time. The correlation functions are binned over all time sources and over forward and backward propagation.

3.7 Fit Details

The simulation energies are extracted by a simultaneous multiexponential fit to multiple free-form smeared correlation functions of the form

$$C^i(t) = \sum_n A_n^i\, e^{-E_n t} \quad , \tag{3.48}$$

where E_n is the fit parameter for the energy of the nth state. Each Λ^{PC} channel from Table 3.2 is fit separately. The fits are done to correlation functions with free-form smeared source operators as described in Eqs. (3.37)–(3.41) and Tables 3.2 and 3.3. For bottomonium, unsmeared source operators are used as well. All fits exclude the source time step at $t = 0$, and are typically truncated at $t = 15$ or $t = 23$ because the signal is lost in noise for larger Euclidean times.

χ^2-minimization fits using an uncorrelated χ^2 were performed [70]. An advantage of using uncorrelated fits is that they are relatively simple and well behaved, whereas a disadvantage is that the χ^2/dof is not a reliable indicator of whether a fit is good. For example, the χ^2/dof may be less than one, but correlations among the time steps may cause the uncorrelated χ^2/dof to be too small, giving a bad fit and a misleading χ^2/dof. This can result in a significant underestimation of the statistical uncertainties in the fit parameters if the only criteria to determining whether a fit is good is a χ^2/dof of one. One way to avoid this is to use a correlated-χ^2 [107], however this method is known to have problems with stability.

Reliable results can still be obtained from uncorrelated fits if care is taken to ensure that the fits are good. It the case of Eq. (3.48), the fit is repeated while increasing the number of exponentials by one and using the previous fit results in the initial guesses. If the χ^2/dof decreases and the new fit parameters behave similarly to the previous fit parameters, then the additional fit parameters have improved the fit. If, however, the χ^2/dof does not decrease or the fit parameters begin to misbehave, i.e. they take on wild values or two or more energies E_n try to fit the same energy with competing values of A_n, then the additional exponential has not improved the fit. Trial and error is required to determine the optimal number exponential terms to achieve a good fit.

For bottomonium, the S-wave correlator is fitted to six exponentials, where the lightest three energies are identified as the ground state, first radial excitation and second radial excitation. The other exponentials are collectively able to account for higher excitations but they are not interpreted individually as physical states.

For the P waves and D waves, separate fits are performed to extract the ground states and first excited states. The fits for the P-wave and D-wave excited states are done using three correlation functions: an unsmeared operator, a free-form smeared ground state, and a free-form smeared excited state. The ground-state P waves and D waves are fit to the first two correlation functions with the excited-state optimized correlator excluded. Removing this correlation function from the fit significantly reduced the statistical uncertainty of the ground states. These more precise ground-state fit values are statistically compatible with the noisier ground-state fit values that are obtained by including the excited-state correlation function. The excited-state fits use five exponentials (six for ${}^3D_1$ and ${}^3D_{3T_1}$) and the ground-

state fits use four (five for ${}^3D_1$ and ${}^3D_{3T_1}$). The D-wave T_1^{--} operators ${}^3D_1$ and ${}^3D_{3T_1}$ have a noticeable mixing with the ${}^3S_1$ ground state and an additional exponential is included in the fit for these two channels. The smallest energy is consistent with the ${}^3S_1$ ground state and all higher energy levels are assumed to be D waves. A confident interpretation would require a cross-correlation matrix between the ${}^3S_1$, ${}^3D_1$ and ${}^3D_{3T_1}$ operators, but this is beyond the scope of the present study. Note that the results for ${}^3S_1$ also assume no D-wave contamination.

The F-wave bottomonium state ${}^3F_3$ is fit with four exponentials to three correlation functions: unsmeared, free-form smeared with $a_0 = 3.0$, and free-form smeared with $a_0 = 4.0$. To obtain a reliable result, ${}^1F_{3A_2}$ is fit with four exponentials to the unsmeared and $a_0 = 3.0$ free-form smeared correlation functions, and ${}^1F_{3T_2}$ is fit with three exponentials to the $a_0 = 3.0$ and $a_0 = 4.0$ free-form smeared correlation functions. The bottomonium G-wave ground states are obtained from four exponential fits to three correlations functions: unsmeared, free-form smeared with $a_0 = 4.0$ and free-form smeared with $a_0 = 5.0$. Even for these higher orbital angular momenta, the hydrogen-like smearing profiles from Eqs. (3.40) and (3.41) produced significantly better ground-state signals than Gaussian smearing.

For B_c mesons, the S-wave correlator is fitted with five exponentials, while the P and D waves use four exponentials. The D-wave T_1^- operators have an overlap with the S-wave B_c^*. The smallest energy is interpreted as the B_c^* ground state and next smallest energy as the D-wave ground state. For B_s and B, the S-wave and P-wave correlators are fitted with four exponentials.

3.8 Bottomonium Spectrum

Since the bottom-quark mass is fixed by tuning the kinetic mass of the Υ to its physical value [51], the absolute masses of the bottomonium spectrum are calculated from

$$mc^2 = m_\Upsilon^{\text{exp}} c^2 + \frac{\hbar c}{a}\left(E^{\text{sim}} - E_\Upsilon^{\text{sim}}\right) \quad . \tag{3.49}$$

Using the lattice spacing scale given in Ref. [102], the masses of the $2S$, $1P$, $2P$ and $1D$ bottomonia are all systematically smaller than the experimental values by a significant amount,

Table 3.5: Bottomonium mass splittings for $\overline{1P}$, $\overline{2S}$, 1^3D_2 and $\overline{2P}$ with respect to $\overline{1S}$, where a bar represents the spin average. Results using two different lattice spacing definitions are shown: Eq. (3.45) and Eq. (3.50). The value for $^3D_2$ is the dimensional average of the E and T_2 lattice representations.

	$m - m_{\overline{1S}}$ [MeV/c^2]		
	lattice using $a_{\text{PACS-CS}}$	lattice using $a_{\overline{1P}-\overline{1S}}$	experiment [108]
$\overline{1P}$	437(6)	455.0(9)	455.0(9)
$\overline{2S}$	547(10)	569(6)	572.5(1.3)
1^3D_2	688(10)	715(3)	719.0(1.7)
$\overline{2P}$	743(15)	773(11)	815.4(9)

as shown in Table 3.5. However, ratios of differences having the $1S$ mass subtracted from the $2S$, $1P$ and $1D$ masses agree with experiment, which suggests using the bottomonium spectrum to set the scale. A new lattice spacing is defined using the spin-averaged $\overline{1P} - \overline{1S}$ mass splitting

$$a_{\overline{1P}-\overline{1S}} = \hbar c \frac{(E_{\overline{1P}} - E_{\overline{1S}})_{\text{sim}}}{(m_{\overline{1P}}c^2 - m_{\overline{1S}}c^2)_{\text{exp}}} = 0.0872(3)\text{fm} \quad , \tag{3.50}$$

which is 4.0% smaller than the PACS-CS value from Eq. (3.45). Reference [106] notes that other methods find a lattice spacing that is up to 4.4% larger than the PACS-CS value for this ensemble.

The lattice spacing reported in Ref. [102] was obtained from the light quark hadron spectrum, which is less relevant for the case of bottomonium. Therefore, Eq. (3.50) is used to set the scale for the bottomonium spectrum. Even after using the scale from Eq. (3.50), the $2P$ masses remain systematically smaller than experiment. This cannot be due to contamination from higher excited states because that would cause the $2P$ masses to be larger, not smaller. Applying radiative corrections or nonperturbative tunings to the NRQCD coefficients c_i and including higher-order terms in the bottomonium velocity are possible ways to remove this discrepancy. In principle, the bottom-quark mass should also be retuned using this new lattice spacing. At present, simply note that setting the scale with physics relevant to the bottom quark increases the accuracy of the bottomonium spectrum.

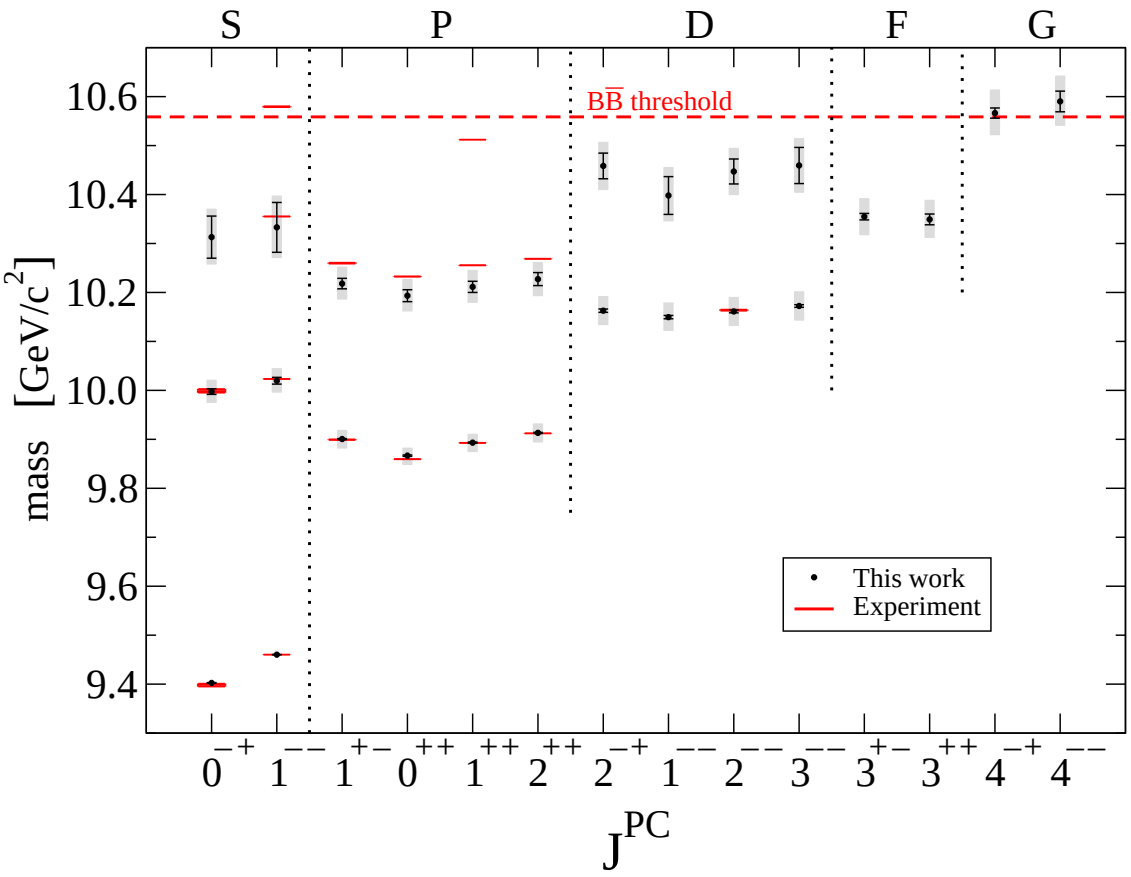

Figure 3.5: Mass spectrum of bottomonium. Red bands are experimental values. Black points with errors bars are lattice data with statistical bootstrap errors only. Grey bands are the statistical error and lattice spacing uncertainty, added in quadrature. Numerical values are given in Table D.1.

The entire bottomonium spectrum below the $B\overline{B}$ threshold [with the exception of the $3P$ states, where the experimental value of $\chi_{b1}(3P)$ is just below the $B\overline{B}$ threshold [109]] is shown in Fig. 3.5, as extracted using chi-squared fits of free-form smeared correlation functions. For spin-2 and spin-3 states, where results for more than one lattice irreducible representation Λ were calculated, the dimensional average of the simulation energies,

$$E_{\overline{\text{dim}}} = \frac{\sum_\Lambda \dim(\Lambda) E_\Lambda}{\sum_\Lambda \dim(\Lambda)} \quad , \tag{3.51}$$

is the reported value for the mass. The grey bands show a combination of the statistical bootstrap errors and a 4.0% systematic uncertainty in the lattice spacing, which come from discrepancies in the determination of the lattice spacing. This work provides the first lattice result for the bottomonium D-wave radial excitations in all channels.

Precise spin splittings were obtained for $1S$, $2S$, $1P$, $2P$ and $1D$ bottomonia, shown in Table 3.6 and Fig. 3.6. The spin splittings in Table 3.6 agree well with experiment, except for the $\chi_{b0}(1P)$. This discrepancy with the BABAR results [110] is more evident in the spin-dependent splittings

$$-2\chi_{b0}(1P) + 3\chi_{b1}(1P) - \chi_{b2}(1P) = \begin{cases} 34.5(9)\,\mathrm{MeV}/c^2 & \text{this work} \\ 46.0(1.9)\,\mathrm{MeV}/c^2 & \text{BABAR} \end{cases} \tag{3.52}$$

$$-2\chi_{b0}(1P) - 3\chi_{b1}(1P) + 5\chi_{b2}(1P) = \begin{cases} 157(4)\,\mathrm{MeV}/c^2 & \text{this work} \\ 160.0(2.2)\,\mathrm{MeV}/c^2 & \text{BABAR} \end{cases} \tag{3.53}$$

where, at tree level, the former is proportional to the NRQCD parameter c_4^2 while the latter is proportional to c_3. For $\chi_{b2}(1P)$ in Eqs. (3.52) and (3.53) the dimensional average of the E and T_2 lattice irreducible representations is used. Since these simulations only use tree-level coefficients where $c_3 = c_4 = 1$, the P-wave spin structure could be improved by tuning c_4 until Eq. (3.52) agrees with experiment. Reference [49] noted that increasing $c_4 > 1$ had the effect of decreasing the $\chi_{b0}(1P)$ mass relative to the $\overline{1^3P}$ spin-averaged mass while doing little else.

The D-wave splittings have not yet been experimentally observed, but the results in Table 3.6 are smaller than the predictions given in Ref. [50], also shown in Table 3.6. Reference [50] proposed a method to reduce systematic effects from c_3 and c_4 dependence. When applied to the data of this work, the method produces results that are consistent within statistical uncertainties with the simple difference shown in Table 3.6.

Table 3.6: Spin splittings for $1S$, $2S$, $1P$, $2P$ and $1D$ bottomonia. $\overline{^3P}$ represents the spin-averaged triplet P wave. All quantities are in units of MeV/c^2. Only statistical bootstrap errors are shown for this work.
[a] Extracted from Fig. 5 of Meinel [46] and Fig. 23 of HPQCD [49].
[b] Extracted from Ref. [50].

	this work	Meinel [46, 48]	HPQCD [49, 50, 52]	experiment [108]
$\Upsilon(1S) - \eta_b(1S)$	57.97(16)	60.3(5.5)(5.0)(2.1)	62.8(6.7)	62.3(3.2) [Belle=57.9(2.3)]
$\Upsilon(2S) - \eta_b(2S)$	22(3)	23.5(4.1)(2.1)(0.8)	26.5(1.6)(1.4)	24(4)
$\overline{1^3P} - \chi_{b0}(1P)$	35.7(5)	36(3)[a]	40.0(1.2)[a]	40.4(5)
$\overline{1^3P} - \chi_{b1}(1P)$	8.3(4)	8.5(1.8)[a]	7.4(6)[a]	7.1(4)
$\overline{1^3P} - h_b(1P)$	0.8(3)	0.04(93)(20)	2.0(6)[a]	0.6(1.0)
$\chi_{b2}(1P) - \overline{1^3P}$	12.1(3)	12.4(1.4)[a]	12.4(5)[a]	12.3(2)
$\overline{2^3P} - \chi_{b0}(2P)$	24(9)	-	-	27.7(7)
$\overline{2^3P} - \chi_{b1}(2P)$	6(5)	-	-	4.8(5)
$\overline{2^3P} - h_b(2P)$	0(4)	-	-	0.4(1.3)
$\chi_{b2}(2P) - \overline{2^3P}$	9(4)	-	-	8.4(3)
$\Upsilon_2(1D) - \Upsilon(1D)$	11(3)	-	17(6)	-
$\Upsilon_3(1D) - \Upsilon_2(1D)$	11(2)	-	18(5)	-
$\Upsilon_3(1D) - \Upsilon(1D)$	22(3)	-	34(8)	-
$\eta_{b2}(1D) - \Upsilon_2(1D)$	1.6(1.5)	-	5(8)[b]	-

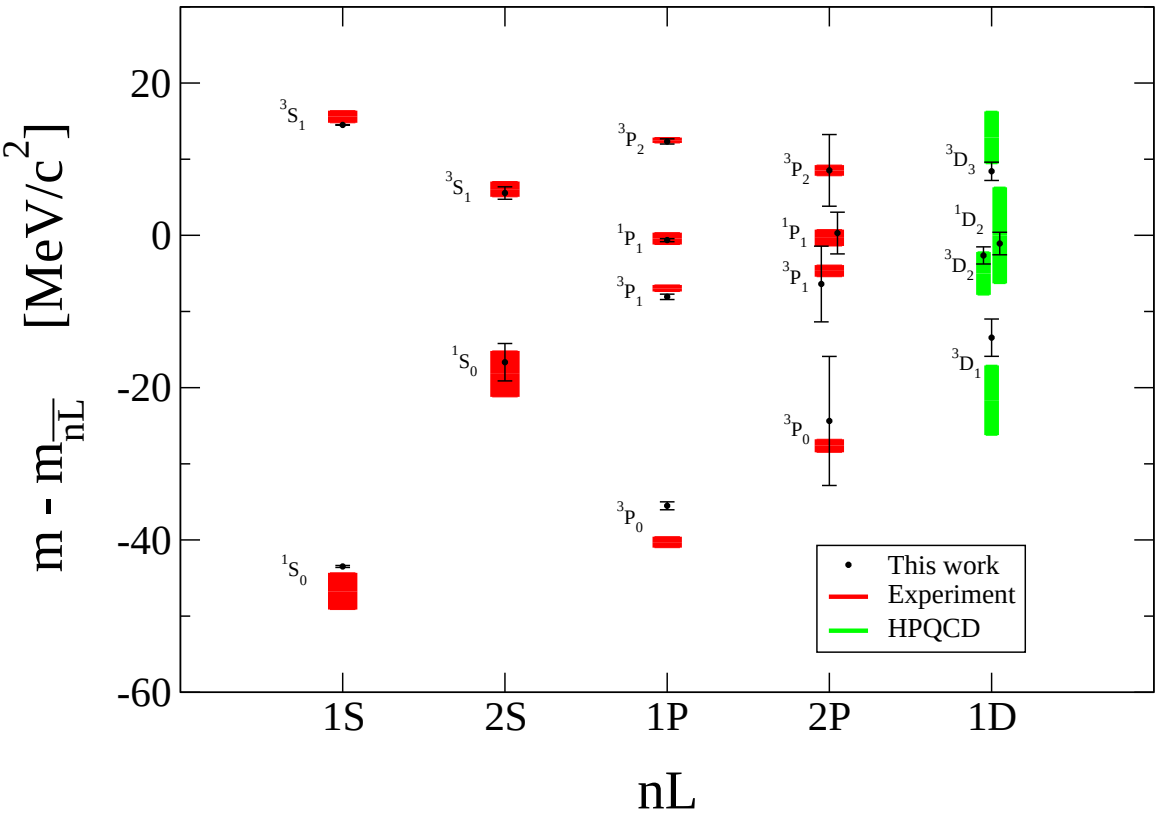

Figure 3.6: Bottomonium mass splittings with respect to the spin average for $1S$, $2S$, $1P$, $2P$ and $1D$. Red bands are experimental values. Green bands are D-wave predictions from Ref. [50]. Black points with errors bars are lattice data with statistical bootstrap errors only.

3.9 B, B_s and B_c Spectrum

In contrast to the case of bottomonium, charge conjugation is not a helpful quantum number for bottom mesons. Whereas the 1^{+-} and 1^{++} operators in Table 3.2 couple to separate quarkonium states, those same two operators each couple to a mixture of heavy-light meson states [111, 112]. The same is true for the 2^{-+} and 2^{--} operators.

In the nonrelativistic basis, the 1^{+-} and 1^{++} operators are distinguished by the presence of a Pauli matrix in the latter but not in the former. Terms in the NRQCD propagator that contain a Pauli matrix are also proportional to an odd power of the quark momentum. The cross correlator of a Pauli matrix operator with a non-Pauli matrix operator will be proportional to an odd power of momentum, and should be zero in the ensemble average because of spatial lattice symmetry. Calculations of the cross correlators of the 1^{+-} and

1^{++} operators for bottom mesons verified that they are statistically consistent with zero at all Euclidean times. This confirms that the two operators are orthogonal, but it does not provide information on the mixing of the physical states within each operator. The same is true for the 2^{-+} and 2^{--} operators.

In practice the 1^{+-} and 1^{++} operators appear to plateau at different energies, given a limited extent in Euclidean time. Even though they should contain the same ground state, they have a mixing with an excited state that is very close in energy to the ground state. They each have a different mixing with these two states, which can give the appearance of different ground states in a practical lattice study. These false ground-state signals would each be larger than the physical ground state and smaller than the physical excited state. A multiexponential fit is unable to distinguish the two physical states given the precision of the data. An application of the variational method to a correlator matrix can separate these states (see, for example, [113]), but that is beyond the scope of this project. Results will be stated from both 1^+ operators (and both 2^- operators), using a prime for the heavier of the pair, and acknowledge that there is an unresolved mixing.

For bottom mesons, the additive NRQCD mass of Eq. (3.49) takes the form

$$mc^2 = \frac{1}{2} m_\Upsilon^{\text{exp}} c^2 + \frac{\hbar c}{a} \left(E^{\text{sim}} - \frac{1}{2} E_\Upsilon^{\text{sim}} \right) \tag{3.54}$$

and the lattice spacing from Eq. (3.50) is used. Absolute masses are not calculated for B_c mesons. The absolute mass for a B_c meson contains large discretization effects because the mass of the charm quark is large compared to the lattice cutoff, so absolute masses will not be studied in this work. Instead, mass differences among B_c states are given because these are expected to be close to their physical values [106].

The spectrum of B_c mass differences with respect to the lightest B_c state for $1S$, $2S$, $1P$, $2P$ and $1D$ is shown in Fig. 3.7. The $J^P = 0^-$ radially excited S-wave state agrees with a recent observation by the ATLAS Collaboration [114]. First lattice results are given for the B_c D-wave ground states and the P-wave radial excitations. The B_c results are all under or very near the BD threshold. Precise B_c spin splittings for $1S$, $2S$, $1P$ and $1D$ are given in Table 3.7. Note that spin splittings are only given between spin 0 and spin 2 for P waves, and spin 1 and spin 3 for D waves, because of the unresolved mixing between the two spin-1

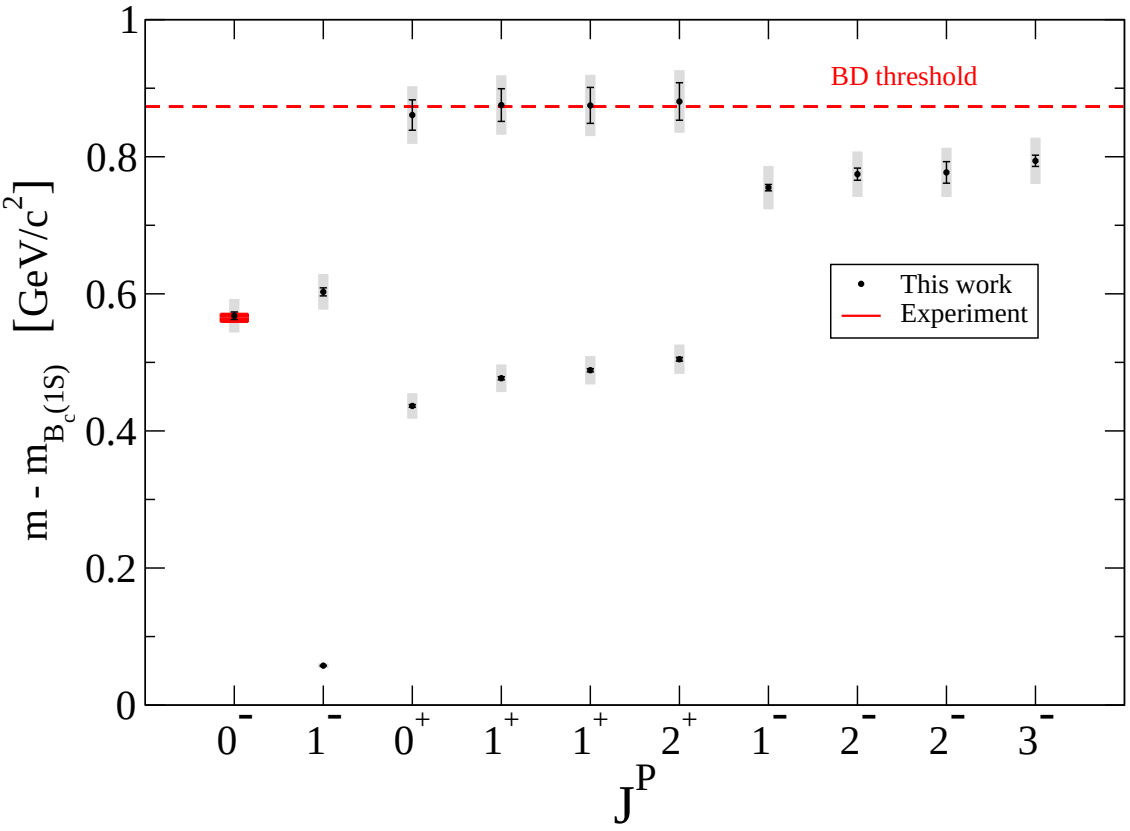

Figure 3.7: Spectrum of B_c meson mass differences with respect to the lightest B_c meson. The red band is an experimental value [114]. Black points with errors bars are lattice data with statistical bootstrap errors only. Grey bands are combined statistical and systematic lattice spacing uncertainty, added in quadrature. Numerical values are given in Table D.2.

P waves and the two spin-2 D waves.

The spectrum of B_s masses for $1S$, $2S$ and $1P$ is shown in Fig. 3.8. B_s spin splittings are given in Table 3.7. The B_s radial and orbital excitations are either very near or above the threshold for breakup into BK or B^*K. Therefore, the $2S$ and $1P$ B_s states have the possibility to mix with these two-meson scattering states. A cross-correlation matrix of B_s with two-meson operators and application of the variational method, which was done in Ref. [61], would be necessary to analyze the mixing and account for its effect.

Since the $J^P = 2^+$ state does not decay to BK via S wave, and the S-wave decay to B^*K is suppressed for the $J^P = 1^+$ state with $j = \frac{3}{2}$ [61, 115], the two-meson decay must contain nonzero momentum. Therefore the finite-volume thresholds for these two states are higher

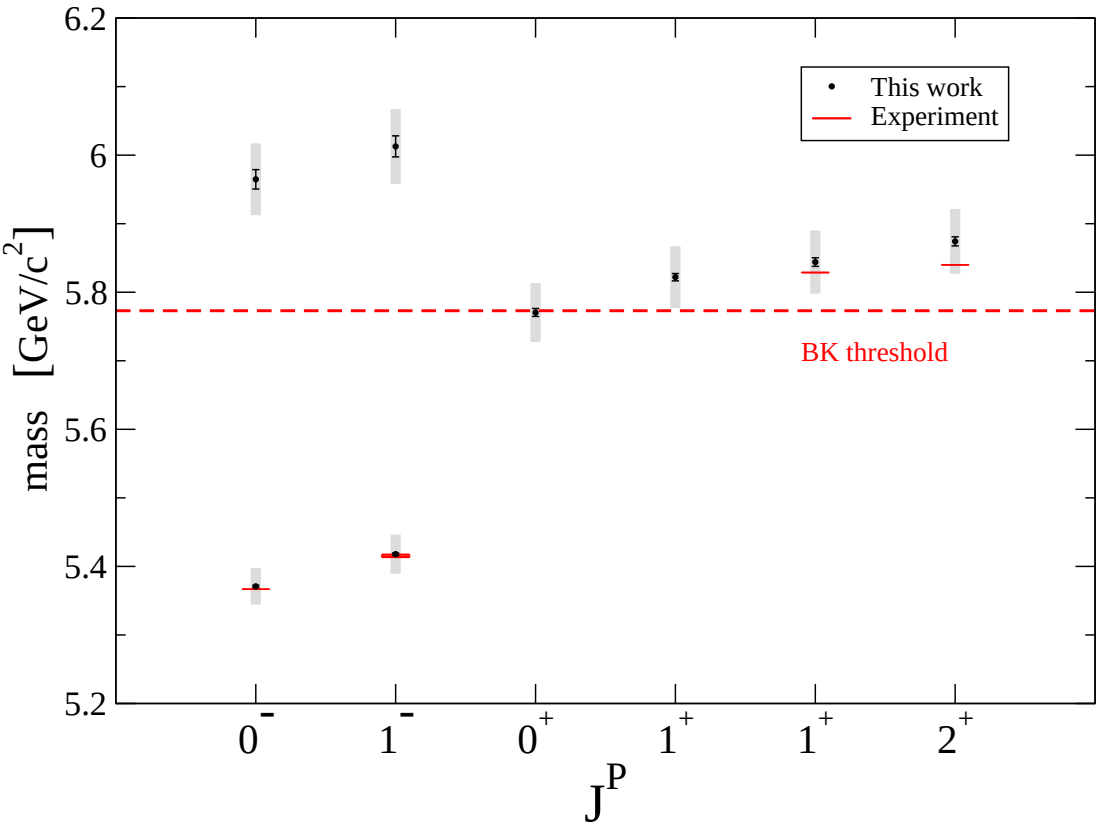

Figure 3.8: Mass spectrum of the B_s meson. Red bands are experimental values. Black points with errors bars are lattice data with statistical bootstrap errors only. Grey bands are combined statistical and systematic lattice spacing uncertainty, added in quadrature. Numerical values can be found in Table D.3.

than the continuum threshold. The same thing applies for the S-wave radial excitations, which are forbidden to decay to $B^{(*)}K$ by S wave. Given the minimum nonzero momentum for the lattice ensemble used in this study, the threshold is around 5.96 GeV for B^*_{s2} and $B^*_s(2S)$, and 6.01 GeV for B'_{s1} and $B_s(2S)$. Recall the systematic uncertainty due to lattice spacing: if the PACS-CS lattice spacing from Eq. (3.45) is used, then the $B^*_{s2} - B_s$ and $B'_{s1} - B_s$ mass differences agree with Ref. [61] and with experiment.

The 0^+ and 1^+ states for B_s have not been observed by experiment. The results agree with Ref. [58], which did not calculate mixing with two-meson states, but differ from Ref. [61], which included two-meson states explicitly, as shown in Table 3.7. This is another indication that including two-meson operators is a necessary step for obtaining reliable masses near and above threshold.

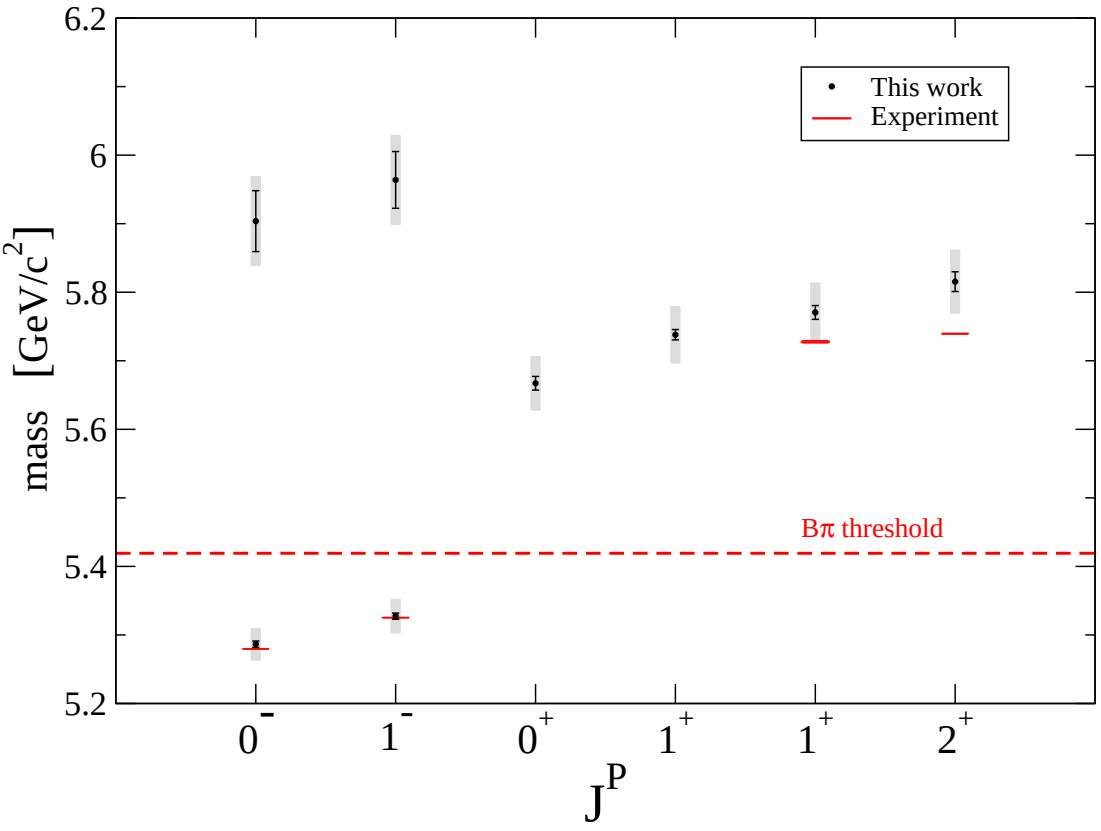

Figure 3.9: Mass spectrum of the B meson. Red bands are experimental values. Black points with errors bars are lattice data with statistical bootstrap errors only. Grey bands are combined statistical and systematic lattice spacing uncertainty, added in quadrature. Numerical values are given in Table D.4.

The spectrum of B masses for $1S$, $2S$ and $1P$ is shown in Fig. 3.9. The LHCb Collaboration has evidence for two states $B(5840)$ and $B(5960)$ in the mass range consistent with $B(2S)$ and $B^*(2S)$ [116]. The CDF Collaboration also has evidence for a state $B(5970)$ in this energy range [117]. B spin splittings are given in Table 3.7. The B radial and orbital excitations are all well above the continuum $B\pi$ threshold. As discussed above for the case of B_s, the two-meson S-wave decays are suppressed for B_2^* and B_1' [115] and are forbidden for $B^*(2S)$ and $B(2S)$. Given the minimum nonzero lattice momentum used in this study, the threshold for B_2^* and $B^*(2S)$ is 5.76 GeV, and for B_1' and $B(2S)$ is 5.81 GeV. A thorough treatment of the B meson spectrum, like that done in Ref. [118] for the D meson P waves, would require the inclusion of two-meson operators.

Table 3.7: Comparison of lattice results for B, B_s and B_c. All quantities are in units of MeV/c^2. Only statistical bootstrap errors are shown for this work.
[a] Mixing with two-meson scattering states was not calculated.
[b] There is unresolved mixing between the two 1^+ states.

	this work	HPQCD [58, 60]	Lang *et. al.* [61]	ALPHA [63]	experiment [108, 114]
$B_s - B$	84(5)	84(2)	81.5(4.3)	88.9(6.1)	87.35(23)
$B^* - B$	41(3)	50(3)	47(7)	41.7(5.3)	45.0(4)
$B_s^* - B_s$	46.9(5)	52(3)	47.1(1.7)	37.8(6.7)	48.7(2.2)
$B_c^* - B_c$	57.5(3)	54(3)	-	-	-
$B^*(2S) - B(2S)$	60(25)[a]	-	-	-	-
$B_s^*(2S) - B_s(2S)$	48(9)[a]	-	-	-	-
$B_c^*(2S) - B_c(2S)$	35(2)	29(26)	-	-	-
$B_2^* - B_0^*$	148(17)[a]	-	-	-	-
$B_{s2}^* - B_{s0}^*$	104(7)[a]	-	142(26)	-	-
$B_{c2}^* - B_{c0}^*$	68(3)	-	-	-	-
$B_{c3}^* - B_c^*(1D)$	39(10)	-	-	-	-
$B(2S) - B$	617(42)[a]	-	-	791(73)[a]	-
$B^*(2S) - B^*$	636(39)[a]	-	-	-	-
$B_s(2S) - B_s$	594(14)[a]	-	-	566(57)[a]	-
$B_s^*(2S) - B_s^*$	595(15)[a]	-	-	-	-
$B_c(2S) - B_c$	568(6)	616(19)	-	-	565(4)(5)
$B_c^*(2S) - B_c^*$	545(6)	591(18)	-	-	-
B_{s0}^*	5770(6)[a]	5752(30)[a]	5711(23)	-	-
B_{s1}	5822(5)[a,b]	5806(30)[a,b]	5750(25)	-	-
B'_{s1}	5844(6)[a,b]	-	5831(11)	-	5828.7(4)
B_{s2}^*	5874(7)[a]	-	5853(13)	-	5839.96(20)
$B_{c0}^* - B_c$	436(2)	429(13)	-	-	-
$B_{c1} - B_c^*$	419(2)[b]	410(13)[b]	-	-	-
$B'_{c1} - B_c^*$	431(2)[b]	-	-	-	-

Chapter 4

Conclusion

4.1 Higgs Spectroscopy

The particle spectrum of the SU(2)-Higgs model has been computed thoroughly, using lattice simulations with all parameters tuned to experimental values. The goal was to search for non-perturbative states that could hypothetically exist due to the analytic connection of the Higgs and confinement regions. Three conceptually different classes of operators were used to extract the energy spectrum: gauge-invariant links, Wilson loops and Polyakov loops. Particular spatial shapes were chosen for these operators to provide access to all irreducible representations of angular momentum and parity, for both isospin 0 and 1. Varying levels of stout-link and scalar smearing were applied to improve the operators and to generate a basis for a variational analysis of the correlation matrices. The energies computed from the variational analysis comprise a vast multi-particle spectrum that is completely consistent with collections of almost-noninteracting Higgs and W bosons. No states were found beyond this simple picture. This result has important consequences for the experiments at the LHC as it points to the nonexistence of bounds states in the Higgs sector.

Of course the interactions between bosons are not expected to be strictly zero, but such tiny deviations from zero are not attainable using the lattice studies presented here. Simulations with a stronger gauge coupling – but still in the Higgs region of the phase diagram – might provide information about interactions, and the fact that the SU(2)-Higgs model is a single phase implies an analytic connection from strong coupling to the physical point. It also implies an analytic connection to the confinement region of the phase diagram with its seemingly very different spectrum. Therefore future lattice studies, similar to what has been here done but at stronger gauge coupling, could be of significant value.

This study, by observing more than a dozen distinct energy levels from the single W up to multiboson states with various momentum options, represents a major step beyond previous simulations of this spectrum. This work demonstrates that present-day lattice methods can provide precise quantitative results for the Higgs-W boson spectrum.

4.2 Free-form Smearing for Heavy Meson Spectroscopy

In this work, the use of free-form smearing has allowed a lattice study of several bottom mesons and bottomonium states. The method permits the user to build a source operator with any desired shape, and does not require gauge fixing. New to the present work is a "minimal-path" method for free-form smearing that reduces the computational cost by $O(L)$ on $L^3 \times T$ lattices. Moreover, any number of unrelated smearing choices for a particular field, i.e. Eq. (3.34), can be built by reusing a single sum over the shortest link paths, i.e. Eq. (3.36).

Beginning with local operators designed to have the appropriate J^{PC} quantum numbers for each hadron, free-form smearing was used to produce a particular hydrogen-like wave-function shape in each case, with the radius and node positions tuned for optimal results. For each meson, the free-form smearing was applied to the bottom quark at the source, leaving the antiquark ($\bar{u}/\bar{d}$, $\bar{s}$, $\bar{c}$ or $\bar{b}$) unsmeared. Bottom quarks were handled with NRQCD and all other quarks were relativistic.

A nearly complete picture of the bottom meson and bottomonium spectrum below the two-meson breakup threshold is given in Figs. 3.5, 3.7, 3.8 and 3.9 with first lattice results for bottomonium D-wave radial excitations, B_c D-wave ground states and B_c P-wave radial excitations. The results for states that are well below the breakup threshold (e.g., $BB^{(*)}$ for bottomonium, $B^{(*)}D$ for B_c) agree reasonably well with available experimental data and several predictions were made.

Some states that were near or even above threshold are also calculated. These include the B and B_s S-wave radial excitations and P-wave ground states, the B_c P-wave radial excitations and the bottomonium G-wave ground states. Where mixing with meson scattering states may be important, a more complete analysis will be required to obtain robust predic-

tions. This work, aimed at constructing correlation functions with good radial and orbital excitation signals, is a step in that direction.

The original free-form smearing [69] was considered unusable for sink smearing. The speedup obtained through the minimal-path implementation gets the method closer to the possibility of sink smearing. This is an avenue for further development that would make the technique more generally applicable and would allow it to be combined with other ideas like the variational method.

Bibliography

[1] S. L. Glashow, "Partial Symmetries of Weak Interactions," Nucl. Phys. **22**, 579 (1961).

[2] P. W. Higgs, "Broken symmetries, massless particles and gauge fields," Phys. Lett. **12**, 132 (1964).

[3] F. Englert and R. Brout, "Broken Symmetry and the Mass of Gauge Vector Mesons," Phys. Rev. Lett. **13**, 321 (1964).

[4] P. W. Higgs, "Broken Symmetries and the Masses of Gauge Bosons," Phys. Rev. Lett. **13**, 508 (1964).

[5] G. S. Guralnik, C. R. Hagen and T. W. B. Kibble, "Global Conservation Laws and Massless Particles," Phys. Rev. Lett. **13**, 585 (1964).

[6] J. Goldstone, "Field Theories with Superconductor Solutions," Nuovo Cim. **19**, 154 (1961).

[7] J. Goldstone, A. Salam and S. Weinberg, "Broken Symmetries," Phys. Rev. **127**, 965 (1962).

[8] P. W. Higgs, "Spontaneous Symmetry Breakdown without Massless Bosons," Phys. Rev. **145**, 1156 (1966).

[9] S. Weinberg, "A Model of Leptons," Phys. Rev. Lett. **19**, 1264 (1967).

[10] A. Salam, "Weak and Electromagnetic Interactions," *Elementary Particle Theory: Relativistic Groups and Analyticity, Nobel Symposium No. 8*, ed. N. Svartholm, (Almqvist and Wiksell, Stockholm, 1968).[1]

[1]Note: This paper is hard to find, but it can be found in Ref. [11].

[11] A. Salam, *Selected papers of Abdus Salam: (with commentary)*, ed. A. Ali, *et. al.* (World Scientific, Singapore, 1994).

[12] G. Aad *et al.* [ATLAS Collaboration], "Observation of a new particle in the search for the Standard Model Higgs boson with the ATLAS detector at the LHC," Phys. Lett. B **716**, 1 (2012) [arXiv:1207.7214 [hep-ex]].

[13] S. Chatrchyan *et al.* [CMS Collaboration], "Observation of a new boson at a mass of 125 GeV with the CMS experiment at the LHC," Phys. Lett. B **716**, 30 (2012) [arXiv:1207.7235 [hep-ex]].

[14] G. Aad *et al.* [ATLAS and CMS Collaborations], "Combined Measurement of the Higgs Boson Mass in pp Collisions at $\sqrt{s} = 7$ and 8 TeV with the ATLAS and CMS Experiments," Phys. Rev. Lett. **114**, 191803 (2015) [arXiv:1503.07589 [hep-ex]].

[15] E. H. Fradkin and S. H. Shenker, "Phase Diagrams of Lattice Gauge Theories with Higgs Fields," Phys. Rev. D **19**, 3682 (1979).

[16] K. Osterwalder and E. Seiler, "Gauge Field Theories on the Lattice," Annals Phys. **110**, 440 (1978).

[17] C. B. Lang, C. Rebbi, and M. Virasoro, "The Phase Structure of a Nonabelian Gauge Higgs Field System," Phys. Lett. **104B**, 294 (1981).

[18] E. Seiler, "Gauge Theories as a Problem of Constructive Quantum Field Theory and Statistical Mechanics," Lect. Notes Phys. **159**, 1 (1982).

[19] H. Kühnelt, C. B. Lang, and G. Vones, "SU(2) Gauge - Higgs Theory With Radial Degree of Freedom," Nucl. Phys. **B230**, 16 (1984).

[20] I. Montvay, "Correlations in the SU(2) Fundamental Higgs Model," Phys. Lett. **150B**, 441 (1985).

[21] J. Jersák, C. B. Lang, T. Neuhaus, and G. Vones, "Properties of Phase Transitions of the Lattice SU(2) Higgs Model," Phys. Rev. D **32**, 2761 (1985).

[22] H. G. Evertz, J. Jersák, C. B. Lang, and T. Neuhaus, "SU(2) Higgs Boson and Vector Boson Masses on the Lattice," Phys. Lett. B **171**, 271 (1986).

[23] V. P. Gerdt, A. S. Ilchev, V. K. Mitrjushkin, I. K. Sobolev and A. M. Zadorozhnyi, "Phase Structure of the SU(2) Lattice Gauge Higgs Theory," Nucl. Phys. B **265**, 145 (1986).

[24] W. Langguth, I. Montvay and P. Weisz, "Monte Carlo Study of the Standard SU(2) Higgs Model," Nucl. Phys. B **277**, 11 (1986).

[25] I. Montvay, "Correlations and Static Energies in the Standard Higgs Model," Nucl. Phys. B **269**, 170 (1986).

[26] W. Langguth and I. Montvay, "A Numerical Estimate Of The Upper Limit For The Higgs Boson Mass," Z. Phys. C **36**, 725 (1987).

[27] A. Hasenfratz, K. Jansen, C. B. Lang, T. Neuhaus, and H. Yoneyama, "The Triviality Bound of the Four Component phi**4 Model," Phys. Lett. B **199**, 531 (1987).

[28] A. Hasenfratz and T. Neuhaus, "Upper Bound Estimate for the Higgs Mass From the Lattice Regularized Weinberg-Salam Model," Nucl. Phys. B **297**, 205 (1988).

[29] H. G. Evertz, E. Katznelson, P. Lauwers and M. Marcu, "Towards A Better Quantitative Understanding Of The Su(2) Higgs Model," Phys. Lett. B **221**, 143 (1989).

[30] G. 't Hooft, "Which Topological Features of a Gauge Theory Can Be Responsible for Permanent Confinement?," NATO Sci. Ser. B **59**, 117 (1980).

[31] S. Elitzur, "Impossibility of Spontaneously Breaking Local Symmetries," Phys. Rev. D **12**, 3978 (1975).

[32] J. Frohlich, G. Morchio and F. Strocchi, "Higgs Phenomenon Without Symmetry Breaking Order Parameter," Nucl. Phys. B **190**, 553 (1981).

[33] J. Frohlich, G. Morchio and F. Strocchi, "Higgs Phenomenon Without A Symmetry Breaking Order Parameter," Phys. Lett. B **97**, 249 (1980).

[34] X. Calmet and H. Fritzsch, "The Electroweak interaction as a confinement phenomenon," Phys. Lett. B **496**, 161 (2000) [hep-ph/0008243].

[35] X. Calmet and H. Fritzsch, "Electroweak D waves," Phys. Lett. B **526**, 90 (2002) [hep-ph/0103333].

[36] A. Maas, "Bound-state/elementary-particle duality in the Higgs sector and the case for an excited 'Higgs' within the standard model," Mod. Phys. Lett. A **28**, 1350103 (2013) [arXiv:1205.6625 [hep-lat]].

[37] A. Maas and T. Mufti, "Non-perturbative aspects in a weakly interacting Higgs sector," PoS ICHEP **2012**, 427 (2013) [arXiv:1211.5301 [hep-lat]].

[38] A. Maas and T. Mufti, "Exploring Higgs Sector Spectroscopy," PoS LATTICE **2013**, 056 (2014) [arXiv:1310.7832 [hep-lat]].

[39] A. Maas and T. Mufti, "Spectroscopic analysis of the phase diagram of Yang-Mills-Higgs theory," Phys. Rev. D **91**, no. 11, 113011 (2015) [arXiv:1412.6440 [hep-lat]].

[40] O. Philipsen, M. Teper and H. Wittig, "On the mass spectrum of the SU(2) Higgs model in (2+1)- dimensions," Nucl. Phys. B **469**, 445 (1996) [hep-lat/9602006].

[41] O. Philipsen, M. Teper and H. Wittig, "Scalar gauge dynamics in (2+1)-dimensions at small and large scalar couplings," Nucl. Phys. B **528**, 379 (1998) [hep-lat/9709145].

[42] M. Wurtz and R. Lewis, "Higgs and W boson spectrum from lattice simulations," Phys. Rev. D **88**, 054510 (2013) [arXiv:1307.1492 [hep-lat]].

[43] M. Wurtz and R. Lewis, "Multi-boson spectrum of the SU(2)-Higgs model," PoS LATTICE **2013**, 059 (2014) [arXiv:1310.1121 [hep-lat]].

[44] C. T. H. Davies, K. Hornbostel, A. Langnau, G. P. Lepage, A. Lidsey, J. Shigemitsu and J. H. Sloan, "Precision Upsilon spectroscopy from nonrelativistic lattice QCD," Phys. Rev. D **50**, 6963 (1994). [hep-lat/9406017].

[45] A. Gray, I. Allison, C. T. H. Davies, E. Dalgic, G. P. Lepage, J. Shigemitsu and M. Wingate, "The Upsilon spectrum and m(b) from full lattice QCD," Phys. Rev. D **72**, 094507 (2005) [hep-lat/0507013].

[46] S. Meinel, "The Bottomonium spectrum from lattice QCD with 2+1 flavors of domain wall fermions," Phys. Rev. D **79**, 094501 (2009) [arXiv:0903.3224 [hep-lat]].

[47] T. Burch, C. DeTar, M. Di Pierro, A. X. El-Khadra, E. D. Freeland, S. Gottlieb, A. S. Kronfeld and L. Levkova *et al.*, "Quarkonium mass splittings in three-flavor lattice QCD," Phys. Rev. D **81**, 034508 (2010) [arXiv:0912.2701 [hep-lat]].

[48] S. Meinel, "Bottomonium spectrum at order v^6 from domain-wall lattice QCD: Precise results for hyperfine splittings," Phys. Rev. D **82**, 114502 (2010) [arXiv:1007.3966 [hep-lat]].

[49] R. J. Dowdall *et al.* [HPQCD Collaboration], "The Upsilon spectrum and the determination of the lattice spacing from lattice QCD including charm quarks in the sea," Phys. Rev. D **85**, 054509 (2012) [arXiv:1110.6887 [hep-lat]].

[50] J. O. Daldrop, C. T. H. Davies and R. J. Dowdall [HPQCD Collaboration], "Prediction of the bottomonium D-wave spectrum from full lattice QCD," Phys. Rev. Lett. **108**, 102003 (2012) [arXiv:1112.2590 [hep-lat]].

[51] R. Lewis and R. M. Woloshyn, "Higher angular momentum states of bottomonium in lattice NRQCD," Phys. Rev. D **85**, 114509 (2012) [arXiv:1204.4675 [hep-lat]].

[52] R. J. Dowdall, C. T. H. Davies, T. Hammant and R. R. Horgan [HPQCD Collaboration], "Bottomonium hyperfine splittings from lattice nonrelativistic QCD including radiative and relativistic corrections," Phys. Rev. D **89**, 031502 (2014) [arXiv:1309.5797 [hep-lat]].

[53] A. Ali Khan, C. T. H. Davies, S. Collins, J. H. Sloan and J. Shigemitsu, "The Heavy - light spectrum from lattice NRQCD," Phys. Rev. D **53**, 6433 (1996) [hep-lat/9512025].

[54] S. Collins, U. M. Heller, J. H. Sloan, J. Shigemitsu, A. Ali Khan and C. T. H. Davies, "B spectroscopy from NRQCD with dynamical fermions," Phys. Rev. D **54**, 5777 (1996) [hep-lat/9602028].

[55] C. T. H. Davies, K. Hornbostel, G. P. Lepage, A. J. Lidsey, J. Shigemitsu and J. H. Sloan, "B(c) spectroscopy from lattice QCD," Phys. Lett. B **382**, 131 (1996) [hep-lat/9602020].

[56] I. F. Allison *et al.* [HPQCD and Fermilab Lattice and UKQCD Collaborations], "Mass of the B_c meson in three-flavor lattice QCD," Phys. Rev. Lett. **94**, 172001 (2005) [hep-lat/0411027].

[57] E. B. Gregory, C. T. H. Davies, E. Follana, E. Gamiz, I. D. Kendall, G. P. Lepage, H. Na and J. Shigemitsu *et al.*, "A Prediction of the B*(c) mass in full lattice QCD," Phys. Rev. Lett. **104**, 022001 (2010) [arXiv:0909.4462 [hep-lat]].

[58] E. B. Gregory, C. T. H. Davies, I. D. Kendall, J. Koponen, K. Wong, E. Follana, E. Gamiz and G. P. Lepage *et al.*, "Precise B, B_s and B_c meson spectroscopy from full lattice QCD," Phys. Rev. D **83**, 014506 (2011) [arXiv:1010.3848 [hep-lat]].

[59] C. McNeile, C. T. H. Davies, E. Follana, K. Hornbostel and G. P. Lepage, "Heavy meson masses and decay constants from relativistic heavy quarks in full lattice QCD," Phys. Rev. D **86**, 074503 (2012) [arXiv:1207.0994 [hep-lat]].

[60] R. J. Dowdall, C. T. H. Davies, T. C. Hammant and R. R. Horgan, "Precise heavy-light meson masses and hyperfine splittings from lattice QCD including charm quarks in the sea," Phys. Rev. D **86**, 094510 (2012) [arXiv:1207.5149 [hep-lat]].

[61] C. B. Lang, D. Mohler, S. Prelovsek and R. M. Woloshyn, "Predicting positive parity B_s mesons from lattice QCD," Phys. Lett. B **750**, 17 (2015) [arXiv:1501.01646 [hep-lat]].

[62] T. Burch, "Heavy hadrons on $N_f = 2$ and $2 + 1$ improved clover-Wilson lattices," arXiv:1502.00675 [hep-lat].

[63] F. Bernardoni, B. Blossier, J. Bulava, M. Della Morte, P. Fritzsch, N. Garron, A. Grardin and J. Heitger *et al.*, "B-meson spectroscopy in HQET at order 1/m," arXiv:1505.03360 [hep-lat].

[64] G. P. Lepage and B. A. Thacker, "Effective Lagrangians for simulating of heavy quark systems," Nucl. Phys. B (Proc. Suppl.) 4, 199 (1988).

[65] B. A. Thacker and G. P. Lepage, "Heavy quark bound states in lattice QCD," Phys. Rev. D **43**, 196 (1991).

[66] G. P. Lepage, L. Magnea, C. Nakhleh, U. Magnea and K. Hornbostel, "Improved nonrelativistic QCD for heavy quark physics," Phys. Rev. D **46**, 4052 (1992) [hep-lat/9205007].

[67] M. Wurtz, R. Lewis and R. M. Woloshyn, "Free-form Smeared Bottomonium Correlation Functions," Proc. Sci. LATTICE **2014** (2014) 111 [arXiv:1409.7103 [hep-lat]].

[68] M. Wurtz, R. Lewis and R. M. Woloshyn, "Free-form smearing for bottomonium and B meson spectroscopy," Phys. Rev. D **92**, no. 5, 054504 (2015) [arXiv:1505.04410 [hep-lat]].

[69] G. M. von Hippel, B. Jäger, T. D. Rae and H. Wittig, "The Shape of Covariantly Smeared Sources in Lattice QCD," J. High Energy Phys. 09 (2013) 014 [arXiv:1306.1440 [hep-lat]].

[70] W. H. Press, S. A. Teukolsky, W. T. Vetterling and B. P. Flannery, *Numerical Recipes in FORTRAN: The Art of Scientific Computing* (Cambridge University Press, Cambridge, 1992).

[71] http://www.netlib.org/lapack/

[72] M. Lüscher, "Solution of the Dirac equation in lattice QCD using a domain decomposition method," Comput. Phys. Commun. **156**, 209 (2004) [hep-lat/0310048].

[73] M. Lüscher, "Schwarz-preconditioned HMC algorithm for two-flavour lattice QCD," Comput. Phys. Commun. **165**, 199 (2005) [hep-lat/0409106].

[74] http://luscher.web.cern.ch/luscher/DD-HMC

[75] G. Marsaglia, "Choosing a Point from the Surface of a Sphere," Ann. Math. Statist. 43, 645 (1972).

[76] M. Creutz, "Monte Carlo Study of Quantized SU(2) Gauge Theory," Phys. Rev. D **21**, 2308 (1980).

[77] M. Creutz, *Quarks, Gluons and Lattices* (Cambridge University Press, Cambridge, 1983).

[78] A. D. Kennedy and B. J. Pendleton, "Improved Heat Bath Method for Monte Carlo Calculations in Lattice Gauge Theories," Phys. Lett. B **156**, 393 (1985).

[79] M. Creutz, "Overrelaxation and Monte Carlo Simulation," Phys. Rev. D **36**, 515 (1987).

[80] Z. Fodor and K. Jansen, "Overrelaxation algorithm for coupled gauge Higgs systems," Phys. Lett. B **331**, 119 (1994) [hep-lat/9403024].

[81] Z. Fodor, J. Hein, K. Jansen, A. Jaster, and I. Montvay, "Simulating the electroweak phase transition in the SU(2) Higgs model," Nucl. Phys. **B439**, 147 (1995).

[82] B. Bunk, "Monte Carlo methods and results for the electro-weak phase transition," Nucl. Phys. Proc. Suppl. **42**, 566 (1995).

[83] C. Morningstar and M. J. Peardon, "Analytic smearing of SU(3) link variables in lattice QCD," Phys. Rev. D **69**, 054501 (2004) [hep-lat/0311018].

[84] S. Güsken, U. Low, K. H. Mütter, R. Sommer, A. Patel and K. Schilling, "Nonsinglet Axial Vector Couplings of the Baryon Octet in Lattice QCD," Phys. Lett. B **227**, 266 (1989).

[85] C. Alexandrou, F. Jegerlehner, S. Güsken, K. Schilling and R. Sommer, "B meson properties from lattice QCD," Phys. Lett. B **256**, 60 (1991).

[86] C. R. Allton *et al.* [UKQCD Collaboration], "Gauge invariant smearing and matrix correlators using Wilson fermions at Beta = 6.2," Phys. Rev. D **47**, 5128 (1993) [hep-lat/9303009].

[87] R. C. Johnson, "Angular Momentum On A Lattice," Phys. Lett. B **114**, 147 (1982).

[88] B. Berg and A. Billoire, "Glueball Spectroscopy in Four-Dimensional SU(3) Lattice Gauge Theory. 1.," Nucl. Phys. B **221**, 109 (1983).

[89] A. S. Kronfeld, "Improved Methods for Computing Masses from Numerical Simulations," Nucl. Phys. Proc. Suppl. **17**, 313 (1990).

[90] M. Lüscher and U. Wolff, "How To Calculate The Elastic Scattering Matrix In Two-dimensional Quantum Field Theories By Numerical Simulation," Nucl. Phys. **B339**, 222 (1990).

[91] R. Lewis and R. M. Woloshyn, "Excited Upsilon Radiative Decays," Phys. Rev. D **84**, 094501 (2011) [arXiv:1108.1137 [hep-lat]].

[92] D. C. Moore and G. T. Fleming, "Angular momentum on the lattice: The Case of non-zero linear momentum," Phys. Rev. D **73**, 014504 (2006) [hep-lat/0507018].

[93] D. C. Moore and G. T. Fleming, "Multiparticle States and the Hadron Spectrum on the Lattice," Phys. Rev. D **74**, 054504 (2006) [hep-lat/0607004].

[94] M. H. L. Pryce, "The Mass center in the restricted theory of relativity and its connection with the quantum theory of elementary particles," Proc. Roy. Soc. Lond. A **195**, 62 (1948).

[95] S. Tani, Soryushiron Kenyu 1, 15 (1949) (in Japanese).

[96] L. L. Foldy and S. A. Wouthuysen, "On the Dirac theory of spin 1/2 particle and its nonrelativistic limit," Phys. Rev. **78**, 29 (1950).

[97] S. Tani, "Connection between Particle Models and Field Theories, I: The Case Spin 1/2," Prog. Theor. Phys. 6, 267 (1951).

[98] R. Lewis and R. M. Woloshyn, "Bottom baryons from a dynamical lattice QCD simulation," Phys. Rev. D **79**, 014502 (2009) [arXiv:0806.4783 [hep-lat]].

[99] G. P. Lepage and P. B. Mackenzie, "On the viability of lattice perturbation theory," Phys. Rev. D **48**, 2250 (1993) [hep-lat/9209022].

[100] G. P. Lepage, "Lattice QCD for small computers," In *Boulder 1993, Proceedings, The building blocks of creation* 207-236, and Preprint - Lepage, G.P. (94/02,rec.Mar.) 31 p [hep-lat/9403018].

[101] S. Groote and J. Shigemitsu, "One loop selfenergy and renormalization of the speed of light for some anisotropic improved quark actions," Phys. Rev. D **62**, 014508 (2000) [hep-lat/0001021].

[102] S. Aoki *et al.* [PACS-CS Collaboration], "2+1 Flavor Lattice QCD toward the Physical Point," Phys. Rev. D **79**, 034503 (2009) [arXiv:0807.1661 [hep-lat]].

[103] Y. Iwasaki, "Renormalization Group Analysis Of Lattice Theories And Improved Lattice Action. 2. Four-dimensional Nonabelian Su(n) Gauge Model," preprint UTHEP-118.

[104] Y. Iwasaki and T. Yoshie, "Renormalization Group Improved Action for SU(3) Lattice Gauge Theory and the String Tension," Phys. Lett. B **143**, 449 (1984).

[105] B. Sheikholeslami and R. Wohlert, "Improved Continuum Limit Lattice Action for QCD with Wilson Fermions," Nucl. Phys. B **259**, 572 (1985).

[106] C. B. Lang, L. Leskovec, D. Mohler, S. Prelovsek and R. M. Woloshyn, "Ds mesons with DK and D*K scattering near threshold," Phys. Rev. D **90**, 034510 (2014) [arXiv:1403.8103 [hep-lat]].

[107] C. Michael, "Fitting correlated data," Phys. Rev. D **49**, 2616 (1994) [hep-lat/9310026].

[108] K. A. Olive *et al.* [Particle Data Group Collaboration], "Review of Particle Physics," Chin. Phys. C **38**, 090001 (2014).

[109] R. Aaij *et al.* [LHCb Collaboration], "Measurement of the $\chi_b(3P)$ mass and of the relative rate of $\chi_{b1}(1P)$ and $\chi_{b2}(1P)$ production," J. High Energy Phys. 10 (2014) 088 [arXiv:1409.1408 [hep-ex]].

[110] J. P. Lees *et al.* [BABAR Collaboration], "Bottomonium spectroscopy and radiative transitions involving the $\chi_b J(1P, 2P)$ states at BABAR," Phys. Rev. D **90**, 112010 (2014) [arXiv:1410.3902 [hep-ex]].

[111] P. Boyle [UKQCD Collaboration], "Heavy meson spectroscopy at Beta = 6.0," Nucl. Phys. Proc. Suppl. **63**, 314 (1998) [hep-lat/9710036].

[112] G. S. Bali, "The D+(sJ)(2317): What can the lattice say?," Phys. Rev. D **68**, 071501 (2003) [hep-ph/0305209].

[113] D. Mohler and R. M. Woloshyn, "D and D_s meson spectroscopy," Phys. Rev. D **84**, 054505 (2011) [arXiv:1103.5506 [hep-lat]].

[114] G. Aad *et al.* [ATLAS Collaboration], "Observation of an Excited $B_c^{\pm}$ Meson State with the ATLAS Detector," Phys. Rev. Lett. **113**, 212004 (2014) [arXiv:1407.1032 [hep-ex]].

[115] N. Isgur and M. B. Wise, "Spectroscopy with heavy quark symmetry," Phys. Rev. Lett. **66**, 1130 (1991).

[116] R. Aaij *et al.* [LHCb Collaboration], "Precise measurements of the properties of the $B_1(5721)^{0,+}$ and $B_2^*(5747)^{0,+}$ states and observation of $B^{+,0}\pi^{-,+}$ mass structures," J. High Energy Phys. 04 (2015) 024 [arXiv:1502.02638 [hep-ex]].

[117] T. A. Aaltonen *et al.* [CDF Collaboration], "Study of orbitally excited B mesons and evidence for a new $B\pi$ resonance," Phys. Rev. D **90**, 012013 (2014) [arXiv:1309.5961 [hep-ex]].

[118] D. Mohler, S. Prelovsek and R. M. Woloshyn, "$D\pi$ scattering and D meson resonances from lattice QCD," Phys. Rev. D **87**, 034501 (2013) [arXiv:1208.4059 [hep-lat]].

Appendix A

SU(2)-Higgs Monte Carlo Algorithms

A.1 Heatbath Update for SU(2)-Gauge Links

The heatbath algorithm for an $SU(2)$-gauge link generates a new link $U_\mu(x)$ according to the distribution

$$dP(U_\mu(x)) \sim dU_\mu(x) \exp\left\{-S(U_\mu(x))\right\} \ . \tag{A.1}$$

The action is linear in $U_\mu(x)$ and so can be written in the form

$$S(U_\mu(x)) = -\frac{1}{2} \operatorname{Tr}\left\{U_\mu(x) W\right\} \ , \tag{A.2}$$

$$W = \beta U_\sqcap + 2\kappa X \ , \tag{A.3}$$

where $U_\sqcap$ is the sum of staples that couple to $U_\mu(x)$

$$U_\sqcap = \sum_{\nu \neq \mu} \left\{ U_\nu(x+\hat{\mu}) U_\mu^\dagger(x+\hat{\nu}) U_\nu^\dagger(x) + U_\nu^\dagger(x-\hat{\nu}+\hat{\mu}) U_\mu^\dagger(x-\hat{\nu}) U_\nu(x-\hat{\nu}) \right\} \ , \tag{A.4}$$

and $X = X_0 \cdot I + i X_a \cdot \sigma_a$ contains the scalar fields that interact with $U_\mu(x)$

$$X_0 = \operatorname{Re}\left\{\Phi^\dagger(x) \Phi(x+\hat{\mu})\right\} \ , \tag{A.5}$$

$$X_a = -\operatorname{Re}\left\{\Phi^\dagger(x) i\sigma_a \Phi(x+\hat{\mu})\right\} \ (a = 1,2,3) \ . \tag{A.6}$$

Rewriting $W = \alpha W_0$, where $\alpha = \sqrt{\det W} > 0$ and $W_0 \in SU(2)$, and using the change of variables

$$U_\mu(x) W_0 = A = a_0 I + i \vec{a} \cdot \vec{\sigma} \ , \tag{A.7}$$

$$a^2 = a_0^2 + \vec{a}^2 = 1 \ , \tag{A.8}$$

the probability distribution becomes

$$dP(U_\mu(x)) \sim d^4a\,\delta\left(a^2-1\right)\exp\left(\alpha a_0\right)\ . \tag{A.9}$$

The Haar measure, $dU_\mu(x) = d(U_\mu(x)W_0) = \pi^{-2}d^4a\,\delta\left(a^2-1\right)$, is invariant under $SU(2)$ transformations. Using the delta function to integrate over the variable $|\vec{a}|$ gives

$$dP(U_\mu(x)) \sim da_0\,d^2\Omega\,\left(1-a_0^2\right)^{\frac{1}{2}}\exp\left(\alpha a_0\right) \quad , \tag{A.10}$$

where $d^2\Omega$ is the differential solid angle of $\vec{a}$ and $|\vec{a}| = \sqrt{1-a_0^2}$. Since the probability distribution of Ω is uniform, the direction of $\vec{a}$ is totally random.

The distribution of a_0 in Eq. (A.10) is independent of the remaining variables $\vec{a} = (a_1, a_2, a_3)$ and may be generated by Monte Carlo according to the distribution

$$dP(a_0) \sim da_0\,\left(1-a_0^2\right)^{\frac{1}{2}}\exp\left(\alpha a_0\right) \quad . \tag{A.11}$$

The simplest approach is the direct accept/reject method, where a_0 is generated in the interval $[-1,1]$ with a uniform distribution and accepted with probability

$$P_{\text{accept}}(a_0) = \frac{\left(1-a_0^2\right)^{\frac{1}{2}}\exp\left(\alpha a_0\right)}{\max\left[\left(1-a_0^2\right)^{\frac{1}{2}}\exp\left(\alpha a_0\right)\right]} \quad . \tag{A.12}$$

As α grows the exponential term in Eq. (A.12) causes the acceptance propability to be strongly peaked for a narrow range of a_0. The acceptance rate decreases as $\frac{1}{2\alpha}\sqrt{\frac{\pi e}{2}}$ for $\alpha \to \infty$ and the method quickly becomes computationally inefficient. A method proposed by Creutz [76, 77] generates a_0 according to the exponential weight and the square root is accounted for by an accept/reject step. The probability distribution of Eq. (A.11) is rewritten as

$$dP(a_0) \sim dz\sqrt{1-\left(\frac{\log z}{\alpha}\right)^2} \quad , \tag{A.13}$$

$$z = \exp(\alpha a_0) \quad . \tag{A.14}$$

The variable z is generated in the interval $[e^{-\alpha}, e^{\alpha}]$ with a uniform distribution and accepted with probability

$$P_{\text{accept}}(z) = \sqrt{1-\left(\frac{\log z}{\alpha}\right)^2} \quad . \tag{A.15}$$

Then a_0 is given by the logarithm

$$a_0 = \frac{\log z}{\alpha} \quad . \tag{A.16}$$

Since the acceptance probability in Eq. (A.15) is much flatter than Eq. (A.12), the Creutz method has a greater acceptance rate and is more computationally efficient. As $\alpha \to \infty$ the acceptance rate goes as $\sqrt{\frac{\pi}{2\alpha}}$.

While the Creutz method has a higher acceptance rate than the direct accept/reject method, it still has a poor acceptance rate as α becomes large. Kennedy and Pendleton [78] proposed a heatbath method which achieves an optimal acceptance rate as $\alpha \to \infty$. The probability distribution of Eq. (A.11) is rewritten as

$$dP(a_0) \sim d\delta \sqrt{1 - \frac{\delta^2}{2}}\, \delta^2 \exp\left(-\alpha\delta^2\right) \quad , \tag{A.17}$$

$$\delta = \sqrt{1 - a_0} \quad , \tag{A.18}$$

where the variable δ is generated in the interval $[0, \infty)$ according to the probability distribution

$$dP(\delta) \sim d\delta\, \delta^2 \exp\left(-\alpha\delta^2\right) \quad , \tag{A.19}$$

and accepted with probability

$$P_{\text{accept}}(\delta) = \begin{cases} \sqrt{1 - \frac{\delta^2}{2}} & 0 \le \delta^2 \le 2 \\ 0 & 2 < \delta^2 \end{cases} \quad . \tag{A.20}$$

Then a_0 is given by

$$a_0 = 1 - \delta^2 \quad . \tag{A.21}$$

As $\alpha \to \infty$, the acceptance rate goes to one. However, since this method also generates $a_0 < -1$, which must be rejected, the method becomes efficient for small α; As $\alpha \to 0$, the acceptance rate goes as $\sqrt{2\pi\alpha^3}$. Therefore, the Creutz method may be used for small α and the Kennedy-Pendleton method for large α, as discussed below.

Generating the distribution in Eq. (A.17) requires a combination of multiple random variables (ξ_1, ξ_2, ρ) with specially chosen probability distributions. The variables $(\xi_1, \xi_2) \in [0, \infty)$

are each generated according to the distribution

$$dP(\xi) = d\xi \int_0^1 dx\, \delta\left(\xi - \sqrt{\frac{-\log x}{\alpha}}\right) = 2\alpha\xi \exp(-\alpha\xi^2)\, d\xi \quad , \tag{A.22}$$

$$\xi = \sqrt{\frac{-\log x}{\alpha}} \quad , \tag{A.23}$$

where x is uniformly distributed in the interval $[0, 1]$. The variable $\rho \in (-\infty, \infty)$ is generated according to a Gaussian distribution using ξ_1 and a uniformly distributed variable $\theta \in [0, 2\pi]$

$$dP(\rho) = d\rho \int_0^\infty dP(\xi_1) \int_0^{2\pi} d\theta\, \delta\left(\rho - \xi_1 \cos\theta\right) = \frac{\alpha}{\pi} \exp(-\alpha\rho^2)\, d\rho \quad , \tag{A.24}$$

$$\rho = \xi_1 \cos\theta \quad . \tag{A.25}$$

A statistically independent variable with the same distribution as Eq. (A.24) is given by $\rho' = \xi_1 \sin\theta$, which can be very useful for inexpensively generating multiple random variables with Gaussian distributions. The distribution of δ from Eq. (A.17) is finally given by a combination of ρ and ξ_2

$$dP(\delta) = d\delta \int_0^\infty dP(\xi_2) \int_{-\infty}^\infty dP(\rho)\, \delta\left(\delta - \sqrt{\xi_2^2 + \rho^2}\right) = 4\alpha\sqrt{\frac{\alpha}{\pi}}\delta^2 \exp(-\alpha\delta^2)\, d\delta \quad , \tag{A.26}$$

$$\delta = \sqrt{\xi_2^2 + \rho^2} \quad . \tag{A.27}$$

The ratio of the acceptance rates of the Creutz and Kennedy-Pendleton methods is

$$\frac{R_{\text{K-P}}}{R_{\text{C}}} = \sqrt{\frac{2\alpha}{\pi}}[1 - \exp(-2\alpha)] \quad . \tag{A.28}$$

At $\alpha = 1.6847$ the two methods have the same acceptance rates. However, since the Kennedy-Pendleton method is computationally more complicated, the two methods have equal computation times at a larger value of α. Depending on the specific numerical implementation, the two methods can have equivalent computation times as low as $\alpha \approx 3.5$ (more efficient implementation) or as high as $\alpha \approx 8$ (less efficient implementation). The computation time as a function of α for each method is quite flat in this range.

A simple recipe for generating a_0 with Kennedy-Pendleton method is as follows: generate four uniformly distributed random numbers $\{x_1, x_2, x_3, x_4\} \in [0, 1]$, calculate

$$a_0 = 1 + \frac{\log x_1 + \cos^2(2\pi x_3) \log x_2}{\alpha} \quad , \tag{A.29}$$

and accept a_0 if

$$a_0 \geq 2x_4^2 - 1 \quad . \tag{A.30}$$

A more efficient implementation is to generate the gaussian random number ρ by generating two uniform random numbers $\{y_1, y_2\} \in [-1, 1]$, accepting (y_1, y_2) if $y_1^2 + y_2^2 \leq 1$ (acceptance rate is $\frac{\pi}{4} = 0.7854$), and calculating

$$\rho = \frac{y_1}{\sqrt{y_1^2 + y_2^2}} \sqrt{\frac{-\log(y_1^2 + y_2^2)}{\alpha}} \quad , \tag{A.31}$$

$$\rho' = \frac{y_2}{\sqrt{y_1^2 + y_2^2}} \sqrt{\frac{-\log(y_1^2 + y_2^2)}{\alpha}} \quad , \tag{A.32}$$

where ρ and ρ' are independent gaussian random numbers. Then a_0 is given by

$$a_0 = 1 + \frac{\log x_1 + \frac{y_1^2}{y_1^2 + y_2^2} \log(y_1^2 + y_2^2)}{\alpha} \quad . \tag{A.33}$$

Even though this method involves an extra accept/reject step, it is more computationally efficient because it avoids the computationally expensive cosine or sine function.

Once a_0 is determined, the remaining task is to generate $\vec{a} = \{a_1, a_2, a_3\}$, which is a uniformly distributed vector with length $\sqrt{1 - a_0^2}$. One method is to generate three uniform random numbers in a box $\{a_1, a_2, a_3\} \in [-1, 1]$, accept them if $\vec{a}^2 \leq 1$, i.e. they lie inside a unit sphere, and then normalize them such that $|\vec{a}| = \sqrt{1 - a_0^2}$. The acceptance rate for this method is $\frac{\pi}{6} = 0.5236$. A more computationally efficient method of generating random numbers on the surface of a uniform sphere is the Marsaglia method [75]: generate two uniform random numbers $\{x_1, x_2\} \in [-1, 1]$, accept them if $x_1^2 + x_2^2 \leq 1$ and then the points

$$\{a_1, a_2, a_3\} = \{2x_1\sqrt{1 - x_1^2 - x_2^2},\ 2x_2\sqrt{1 - x_1^2 - x_2^2},\ 1 - 2(x_1^2 + x_2^2)\} \tag{A.34}$$

are uniformly distributed on a unit sphere. The acceptance rate for this method is $\frac{\pi}{4} = 0.7854$. The final value for the link variable is then given by

$$U_\mu(x) = W_0^\dagger A \quad , \tag{A.35}$$

where $A = a_0 I + i\vec{a} \cdot \vec{\sigma}$.

For the initial configuration of the Markov chain one usually chooses either a uniform or random field configuration. A random $SU(2)$ field configuration is given by four points

$u = \{u_1, u_2, u_3, u_4\}$ such that $u^2 = u_1^2 + u_2^2 + u_3^2 + u_4^2 = 1$ which are uniformly distributed on a unit four-sphere. The simplest approach is to generate the four random numbers uniformly in the interval $[-1, 1]$, accept them if $u^2 \leq 1$, and then normalize u to unity. The acceptance rate for this is $\frac{\pi^2}{32} = 0.3084$. An alternative is to generate four gaussian random numbers $\rho = \{\rho_1, \rho_2, \rho_3, \rho_4\}$ using Eqs. (A.31) and (A.32) and then $u = \rho/\sqrt{u^2}$. A more efficient approach is the Marsaglia method for the four-sphere [75]: generate uniform random numbers $\{x_1, x_2\} \in [-1, 1]$, accept them if $x_1^2 + x_2^2 \leq 1$, then generate uniform random numbers $\{x_3, x_4\} \in [-1, 1]$, accept them if $x_3^2 + x_4^2 \leq 1$, then

$$u_1 = x_1 \quad , \tag{A.36}$$

$$u_2 = x_2 \quad , \tag{A.37}$$

$$u_3 = x_3 \sqrt{\frac{1 - x_1^2 - x_2^2}{x_3^2 + x_4^2}} \quad , \tag{A.38}$$

$$u_3 = x_4 \sqrt{\frac{1 - x_1^2 - x_2^2}{x_3^2 + x_4^2}} \quad . \tag{A.39}$$

A.2 Heatbath Update for a Complex Scalar Doublet

The heatbath algorithm for an $SU(2)$-Higgs doublet [82] generates the four degrees of freedom of

$$\Phi(x) = \begin{pmatrix} \phi_2(x) + i\phi_1(x) \\ \phi_0(x) - i\phi_3(x) \end{pmatrix} \quad , \tag{A.40}$$

according to the Boltzmann distribution

$$dP(\Phi(x)) \sim d^4\phi(x) \exp\{-S(\Phi(x))\} \ , \tag{A.41}$$

$$\begin{aligned} S(\Phi(x)) &= \lambda \left(|\Phi(x)|^2 - 1\right)^2 + |\Phi(x)|^2 \\ &\quad - 2\kappa \sum_{\mu=1}^{4} \mathrm{Re}\left\{\Phi^\dagger(x) U_\mu(x) \Phi(x + \hat{\mu}) + \Phi^\dagger(x - \hat{\mu}) U_\mu(x - \hat{\mu}) \Phi(x)\right\} \quad . \end{aligned} \tag{A.42}$$

The gauge-Higgs interaction can be rewritten as

$$\begin{aligned} &\sum_{\mu=1}^{4} \mathrm{Re}\left\{\Phi^\dagger(x) U_\mu(x) \Phi(x + \hat{\mu}) + \Phi^\dagger(x - \hat{\mu}) U_\mu(x - \hat{\mu}) \Phi(x)\right\} \\ &= \mathrm{Re}\left\{\Phi^\dagger(x) Y(x)\right\} = \Phi(x) \cdot Y(x) \quad , \end{aligned} \tag{A.43}$$

where

$$Y(x) = \sum_{\mu=1}^{4} \left\{ U_\mu(x)\Phi(x+\hat{\mu}) + U_\mu(x-\hat{\mu})^\dagger \Phi(x-\hat{\mu}) \right\} \quad , \tag{A.44}$$

is a complex doublet and $\Phi(x) \cdot Y(x)$ is a 4-dimensional dot product of the real components of $\Phi(x)$ and $Y(x)$. The action of $\Phi(x)$ can now be written in the simplified form

$$S(\Phi) = \lambda \left(|\Phi|^2 - 1 \right)^2 + |\Phi|^2 + \Phi \cdot Y \quad , \tag{A.45}$$

where (x) is dropped for brevity. The quadratic part of the action can be generated directly; however, the quartic part must be taken into account using an accept/reject step. Therefore, an optimization parameter ξ is introduced to maximize the overlap of the quadratic and quartic terms, and action becomes (up to to an irrelevant constant)

$$S(\Phi) = \lambda \left(|\Phi|^2 - 1 + \frac{1-\xi}{2\lambda} \right)^2 + \xi \left| \Phi - \frac{Y}{\xi} \right|^2 \quad . \tag{A.46}$$

The four real components of Φ are each generated according to the gaussian distribution

$$dP_G(\phi_m) = d\phi_m \sqrt{\frac{\xi}{\pi}} \exp \left\{ -\xi \left(\phi_m - \frac{Y_m}{\xi} \right)^2 \right\} \tag{A.47}$$

by generating four random numbers $x_1, x_2, x_3, x_4 \in [0, 1]$ and calculating

$$\phi_0 = \sqrt{\frac{-\log x_1}{\xi}} \cos(2\pi x_2) + \frac{Y_0}{\xi} \ , \tag{A.48}$$

$$\phi_1 = \sqrt{\frac{-\log x_1}{\xi}} \sin(2\pi x_2) + \frac{Y_1}{\xi} \ , \tag{A.49}$$

$$\phi_2 = \sqrt{\frac{-\log x_3}{\xi}} \cos(2\pi x_4) + \frac{Y_2}{\xi} \ , \tag{A.50}$$

$$\phi_3 = \sqrt{\frac{-\log x_3}{\xi}} \sin(2\pi x_4) + \frac{Y_3}{\xi} \ . \tag{A.51}$$

A computationally efficient alternative is to implement Eqs. (A.31) and (A.32). Φ is then accepted with the conditional probability

$$P_A(\Phi) = \exp \left\{ -\lambda \left(|\Phi|^2 - 1 + \frac{1-\xi}{2\lambda} \right)^2 \right\} \ . \tag{A.52}$$

The parameter ξ maximizes the acceptance rate

$$R = \int_{-\infty}^{\infty} dP_G(\Phi) P_A(\Phi) \tag{A.53}$$

which gives the following equation for ξ

$$\xi^3 + (2\lambda - 1)\xi^2 - 4\lambda\xi - 2\lambda \det(Y) = 0 \ . \tag{A.54}$$

Solving a cubic equation exactly can be computationally expensive. In this case it is also unnecessary because ξ only affects the acceptance rate, not the final statistical distribution. The only coefficient in Eq. (A.54) that changes from lattice site to lattice site is $\det(Y)$, and this changes only a little bit. Taking advantage of the fact that ξ changes little between different lattice sites, ξ is calculated exactly for the first lattice site and then for subsequent sites is calculated approximately by Newton's method

$$\xi = \xi_0 - \frac{\xi_0^3 + (2\lambda - 1)\xi_0^2 - 4\lambda\xi_0 - 2\lambda \det(Y)}{3\xi_0^2 + 2(2\lambda - 1)\xi_0 - 4\lambda} \quad , \tag{A.55}$$

where ξ_0 is the value of ξ from the previously visited lattice site.

A.3 Overrelaxation Update

Overrelaxation is a Monte Carlo update which proposes a change that moves the field variable to a different location in phase space while resulting in only a small change in the action [79]. Combined with standard Monte Carlo methods, like the heatbath or Metropolis algorithms, overrelaxation greatly reduces autocorrelation between configurations, particularly for the $SU(2)$-Higgs model [80]. The limiting case of a deterministic overrelaxation update is often used. The new field variable is given by a reflection $f(U)$, where U is the old variable and $f(f(U)) = U$. The update is then accepted with probability

$$P_A(U) = \max\left(1, \left|\frac{df(U)}{dU}\right| \frac{\exp\{-S(f(U))\}]}{\exp\{-S(U)\}}\right) \quad . \tag{A.56}$$

The overrelaxation for the $SU(2)$-gauge link is given by the reflection

$$f(U) = \frac{W^\dagger U^\dagger W^\dagger}{\det W} \quad , \tag{A.57}$$

where W is given by Eq. (A.3) and the update is always accepted. A simple overrelaxation update for the $SU(2)$-Higgs doublet [82] is a reflection that leaves of the quadratic part of the action given in Eq. (A.46) invariant

$$f(\Phi) = -\Phi + \frac{2Y}{\xi} \quad , \tag{A.58}$$

where ξ is the same as in Eq. (A.54). The update is accepted with a conditional probability

$$P_A(\Phi) = \max\left(1\,,\, \frac{\exp\left\{-\lambda\left(|f(\Phi)|^2 - 1 + \frac{1-\xi}{2\lambda}\right)^2\right\}}{\exp\left\{-\lambda\left(|\Phi|^2 - 1 + \frac{1-\xi}{2\lambda}\right)^2\right\}}\right) \quad . \tag{A.59}$$

Appendix B

Lattice Rotational Symmetries

The continous symmetry of rotations in three dimensions corresponds to conservation of angular momentum. From the canonical commutators of the angular momentum operators $[J_i, J_j] = i\epsilon_{ijk}J_k$, it follows that only integer and half-integer eigenvalues for J_i are allowed. This is can easily be seen by examining the eigenvalues of angular momentum along the z-axis

$$\langle J, m'| L_z |J, m\rangle = m\delta_{m',m} \tag{B.1}$$

$$m = -J, -J+1, \ldots, J-1, J \quad . \tag{B.2}$$

Therefore, $J = -J + N \Rightarrow J = N/2$ where N is an integer.

Angular momentum is no longer a conserved quantity on a lattice because continuous spatial symmetry is broken to a discrete subgroup. The continuous rotational symmetry group $SO(3)$ is broken down to the 24 element octahedral symmetry group O [87, 88]. The rotations of the cubic group O are given by C_k^i, where k is the number of unique cubic symmetry rotations (including the identity) that can be done on an axis, also called the order of an axis, and i is the number of rotation axes of order k. The cubic rotations $\{C_2^{(1,2,3,4,5,6)}, C_3^{(1,2,3,4)}, C_4^{(1,2,3)}\}$ are listed in Table B.1 and illustrated in Fig. B.1.

There are five conjugacy classes for the group O. Recall the definitions: $g_1, g_2 \in G$ are conjugate if $\exists\ h \in G$ such that $g_1 = h \cdot g_2 \cdot h^{-1}$. A conjugacy class is the set of all mutually conjugate elements of G. Using c_k^i to denote the smallest positive rotation about an axis,

Table B.1: The three types of symmetry axes of a cube. Listed by number of rotations per axis, number of axes, minimal positive angle of rotation θ and the part of the cube about which the rotation takes place.

	# rotations per axis	# axes	θ	rotate about cube
C_2^i	2	6	π	edge
C_3^i	3	4	$\frac{2\pi}{3}$	diagonal
C_4^i	4	3	$\frac{\pi}{2}$	face

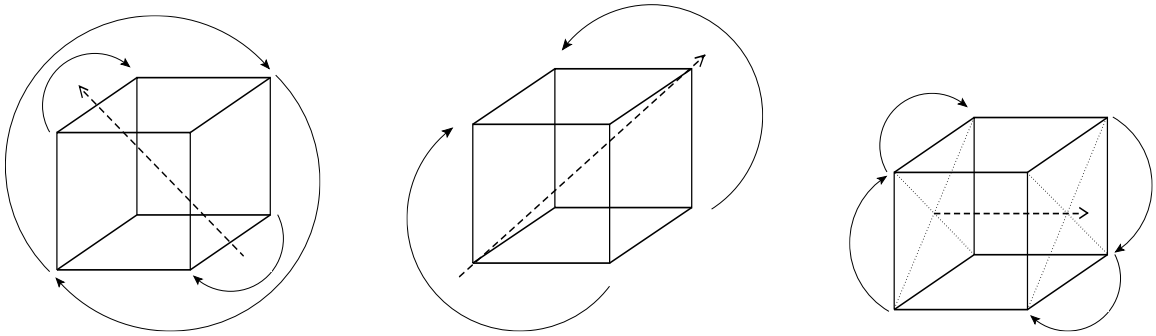

Figure B.1: Illustration of the different axes of symmetric cubic rotation. From left to right: C_2^i (edge), C_3^i (diagonal) and C_4^i (face).

and e for the trivial element, the conjugacy classes for O are

$$E = \{e\} \tag{B.3}$$

$$C_2 = \left\{c_2^i\right\} \tag{B.4}$$

$$C_3 = \left\{c_3^i, (c_3^i)^2\right\} \tag{B.5}$$

$$C_4 = \left\{c_4^i, (c_4^i)^3\right\} \tag{B.6}$$

$$C_4^2 = \left\{(c_4^i)^2\right\} \quad . \tag{B.7}$$

In particular, note that π rotations about the face of a cube are not conjugate to $\{\pi/2, 3\pi/2\}$ face rotations, i.e. $\nexists h \in O \ni (c_4^i)^2 = h \cdot c_4^j \cdot h^{-1}$.

The number of irreducible representations (irrep) of a group is equal to the number of conjugacy classes, and the sum of the squared dimensions of these irreps is equal to the number of elements in the group. For the octahedral group O there are five irreps, historically

named in crystallography as $\{A_1, A_2, E, T_1, T_2\}$, with dimensions $\{1, 1, 2, 3, 3\}$. The character table for the irreps of O is given in Table B.2.

Table B.2: Character table for the irreducible representations of the octahedral group O. The number of elements in each (non-trivial) conjugacy class is also given on the first line. The last line gives the smallest postive angle of rotation.

	E	$6C_2$	$8C_3$	$6C_4$	$3C_4^2$
A_1	1	1	1	1	1
A_2	1	-1	1	-1	1
E	2	0	-1	0	2
T_1	3	-1	0	1	-1
T_2	3	1	0	-1	-1
θ	0	π	$2\pi/3$	$\pi/2$	π

Continuum angular momentum with integer values $J = 0, 1, 2, ...$ are subduced to the irreps $\Lambda = \{A_1, A_2, E, T_1, T_2\}$ of the group O. The multiplicity

$$m_\Lambda^J = \frac{1}{24} \sum_{k=1}^{5} n_k \chi_k^\Lambda \chi^J(\theta_k) \quad , \tag{B.8}$$

is the projection of the irreps of $SO(3)$ onto the irreps of O, where k denotes the conjugacy class, n_k is the number of elements in the conjugacy class k, χ_k^Λ are the characters of the group O given in Table B.2, θ_k are the rotation angles of the conjugacy class k and $\chi^J(\theta_k)$ are the characters of the group $SO(3)$ as a function of rotation angle

$$\chi^J(\theta) = \mathrm{Tr}(\exp(-iJ_z\theta)) = \begin{cases} \frac{\sin\left((2J+1)\frac{\theta}{2}\right)}{\sin\left(\frac{\theta}{2}\right)} & \text{if } \theta \neq 0 \\ 2J+1 & \text{if } \theta = 0 \end{cases} \quad . \tag{B.9}$$

J_z are the matrix elements of angular momentum along the z-axis, given by Eq. (B.1). Table B.3 gives the multiplicities of the continuum spin J onto the irreps Λ.

The concept of angular momentum J on a spatially cubic lattice is necessarily replaced by a finite set of irreducible representations Λ of the octahedral group of symmetric rotations O. States in a numerical lattice calculation have the quantum number Λ, which can be mapped back to the continuum by Table B.3.

Table B.3: The number of copies of each irreducible representation Λ of the octahedral group O for continuum integer spin J.

Λ	J							
	0	1	2	3	4	5	6	...
A_1	1	0	0	0	1	0	1	...
A_2	0	0	0	1	0	0	1	...
E	0	0	1	0	1	1	1	...
T_1	0	1	0	1	1	2	1	...
T_2	0	0	1	1	1	1	2	...

Including the reflection symmetry, i.e. the parity group $C_2 = \{e, p\}$[1], the cubic symmetry group becomes the product $O_h = O \otimes C_2$. The parity operator p has the effect of reflecting a vector about the origin $p\mathbf{x} = -\mathbf{x}$. The octahedral group of rotations and reflections O_h has 48 elements and 10 conjugacy classes corresponding to Eqs. (B.3)-(B.7) and

$$P = \{p\} \tag{B.10}$$

$$PC_2 = \left\{pc_2^i\right\} \tag{B.11}$$

$$PC_3 = \left\{pc_3^i, p(c_3^i)^2\right\} \tag{B.12}$$

$$PC_4 = \left\{pc_4^i, p(c_4^i)^3\right\} \tag{B.13}$$

$$PC_4^2 = \left\{p(c_4^i)^2\right\} \quad . \tag{B.14}$$

The irreps are given by positive and negative parity copies Λ^P, where $\Lambda = \{A_1, A_2, E, T_1, T_2\}$ and $P = \{+1, -1\}$. The character table of O_h is an expanded version of Table B.2, where

$$\chi^{\Lambda^+}(O_h) = \chi^{\Lambda}(O) \quad , \tag{B.15}$$

$$\chi^{\Lambda^-}(O \otimes e) = \chi^{\Lambda}(O) \quad , \tag{B.16}$$

$$\chi^{\Lambda^-}(O \otimes p) = -\chi^{\Lambda}(O) \quad . \tag{B.17}$$

Charge conjugation $C = \{+1, -1\}$ can be included in the same way as parity, and the result is irreps Λ^{PC} which correspond to the continuum quantum numbers J^{PC}.

[1]The group C_2 is more generally known as the cyclic group of order 2, where $C_2 = \{e, c_2\}$ and $(c_2)^2 = e$.

The above discussion dealt solely with integer angular momentum on a lattice. To describe half-integer angular momentum, the anti-commutivity of fermions must be taken into account. This is done by including a negative identity i for $\theta = 2\pi$ rotations. This gives the double cover octahedral group $O^D = O \otimes C_2$, where $C_2 = \{e, i\}$. Unlike parity, which is independent of rotations, the negative identity i depends non-trivially on the rotations of O. There are eight conjugacy classes for O^D, and the irreps are $\{A_1, A_2, E, T_1, T_2, G_1, G_2, H\}$, where the first five correspond to integer angular momentum and the last three to half-integer angular momentum. The half-integer irreps $\{G_1, G_2, H\}$ have dimensions $\{2, 2, 4\}$ and their relation to continuum angular momentum is given in Table B.4.

Table B.4: The number of copies of the irreducible representations Λ of the double cover octahedral group O^D for continuum half-integer spin J.

Λ	J					
	$\frac{1}{2}$	$\frac{3}{2}$	$\frac{5}{2}$	$\frac{7}{2}$	$\frac{9}{2}$	$\ldots$
G_1	1	0	0	1	1	$\ldots$
G_2	0	0	1	1	0	$\ldots$
H	0	1	1	1	2	$\ldots$

Appendix C

Lists of Two-Particle Operators

A list of all Higgs-Higgs, Higgs-W and W-W operators with back-to-back momentum $|\vec{p}| = 2\pi/L$, $|\vec{p}| = \sqrt{2}(2\pi/L)$ and $|\vec{p}| = \sqrt{3}(2\pi/L)$ is given in Tables C.1-C.14 (operators with $I > 1$ are not considered in this work). The Higgs-W operators are written using the compressed notation

$$\mu\nu \equiv \begin{cases} H(\vec{p}_\nu)W^a_\mu(-\vec{p}_\nu) - W^a_\mu(\vec{p}_\nu)H(-\vec{p}_\nu) & \text{if } \; P = +1 \\ H(\vec{p}_\nu)W^a_\mu(-\vec{p}_\nu) + W^a_\mu(\vec{p}_\nu)H(-\vec{p}_\nu) & \text{if } \; P = -1 \end{cases} \tag{C.1}$$

where two different combinations are used depending on the intended parity. The W-W operators are written using the compressed notation

$$\mu\nu\rho \equiv \begin{cases} W^a_\mu(\vec{p}_\rho)W^a_\nu(-\vec{p}_\rho) & \text{if } \; I = 0 \\ \epsilon^{abc}W^b_\mu(\vec{p}_\rho)W^c_\nu(-\vec{p}_\rho) & \text{if } \; I = 1 \end{cases} \tag{C.2}$$

where repeated isospin indices (a, b, c) are summed. The momentum vectors are defined as

$$\vec{p}_1 = \frac{2\pi}{L}(1,0,0) \qquad \vec{p}_2 = \frac{2\pi}{L}(0,1,0) \qquad \vec{p}_3 = \frac{2\pi}{L}(0,0,1) \tag{C.3}$$

for $|\vec{p}| = 2\pi/L$,

$$\begin{aligned} \vec{p}_1 = \frac{2\pi}{L}(1,1,0) \qquad \vec{p}_2 = \frac{2\pi}{L}(0,1,1) \qquad \vec{p}_3 = \frac{2\pi}{L}(1,0,1) \\ \vec{p}_4 = \frac{2\pi}{L}(1,-1,0) \qquad \vec{p}_5 = \frac{2\pi}{L}(0,1,-1) \qquad \vec{p}_6 = \frac{2\pi}{L}(-1,0,1) \end{aligned} \tag{C.4}$$

for $|\vec{p}| = \sqrt{2}(2\pi/L)$, and

$$\vec{p}_0 = \frac{2\pi}{L}(1,1,1) \qquad \vec{p}_1 = \frac{2\pi}{L}(-1,1,1) \qquad \vec{p}_2 = \frac{2\pi}{L}(1,-1,1) \qquad \vec{p}_3 = \frac{2\pi}{L}(1,1,-1) \tag{C.5}$$

for $|\vec{p}| = \sqrt{3}(2\pi/L)$.

Table C.1: Higgs-Higgs operators with back-to-back momentum.

$I(\Lambda^P)$	$\lvert\vec{p}\rvert$	Operator
$0(A_1^+)$	$2\pi/L$	$H(p_1)H(-p_1) + H(p_2)H(-p_2) + H(p_3)H(-p_3)$
$0(E^+)$	$2\pi/L$	$H(p_1)H(-p_1) - H(p_2)H(-p_2)$
		$H(p_1)H(-p_1) + H(p_2)H(-p_2) - 2 \times H(p_3)H(-p_3)$
$0(A_1^+)$	$\sqrt{2}(2\pi/L)$	$H(p_1)H(-p_1) + H(p_2)H(-p_2) + H(p_3)H(-p_3)$
		$+H(p_4)H(-p_4) + H(p_5)H(-p_5) + H(p_6)H(-p_6)$
$0(E^+)$	$\sqrt{2}(2\pi/L)$	$H(p_1)H(-p_1) - H(p_2)H(-p_2) + H(p_4)H(-p_4) - H(p_5)H(-p_5)$
		$H(p_1)H(-p_1) + H(p_2)H(-p_2) - 2 \times H(p_3)H(-p_3)$
		$+H(p_4)H(-p_4) + H(p_5)H(-p_5) - 2 \times H(p_6)H(-p_6)$
$0(T_2^+)$	$\sqrt{2}(2\pi/L)$	$H(p_1)H(-p_1) - H(p_4)H(-p_4)$
		$H(p_2)H(-p_2) - H(p_5)H(-p_5)$
		$H(p_3)H(-p_3) - H(p_6)H(-p_6)$
$0(A_1^+)$	$\sqrt{3}(2\pi/L)$	$H(p_0)H(-p_0) + H(p_1)H(-p_1) + H(p_2)H(-p_2) + H(p_3)H(-p_3)$
$0(T_2^+)$	$\sqrt{3}(2\pi/L)$	$H(p_0)H(-p_0) + H(p_1)H(-p_1) - H(p_2)H(-p_2) - H(p_3)H(-p_3)$
		$H(p_0)H(-p_0) - H(p_1)H(-p_1) + H(p_2)H(-p_2) - H(p_3)H(-p_3)$
		$H(p_0)H(-p_0) - H(p_1)H(-p_1) - H(p_2)H(-p_2) + H(p_3)H(-p_3)$

Table C.2: Higgs-W operators from Eq. (C.1) with $|\vec{p}| = 2\pi/L$.

$I(\Lambda^P)$	Operator
$1(A_1^+)$	$11 + 22 + 33$
$1(E^+)$	$11 - 22, \quad 11 + 22 - 2 \times 33$
$1(T_1^+)$	$12 - 21,\ (123 \to 231),\ (123 \to 312)$
$1(T_2^+)$	$12 + 21,\ (123 \to 231),\ (123 \to 312)$
$1(T_1^-)$	$11,\ (123 \to 231),\ (123 \to 312)$
$1(T_1^-)$	$12 + 13,\ (123 \to 231),\ (123 \to 312)$
$1(T_2^-)$	$12 - 13,\ (123 \to 231),\ (123 \to 312)$

Table C.3: Higgs-W operators from Eq. (C.1) with $|\vec{p}| = \sqrt{2}(2\pi/L)$.

$I(\Lambda^P)$	Operator
$1(A_1^+)$	$11+21+22+32+33+13+14-24+25-35+36-16$
$1(A_2^+)$	$11-21+22-32+33-13+14+24+25+35+36+16$
$1(E^+)$	$11+21-22-32+14-24-25+35$
	$11+21+22+32-2\times33-2\times13$
	$+14-24+25-35-2\times36+2\times16$
$1(E^+)$	$11-21-22+32+14+24-25-35$
	$11-21+22-32-2\times33+2\times13$
	$+14+24+25+35-2\times36-2\times16$
$1(T_1^+)$	$11-21-14-24,\ (123456\to231564),\ (123456\to312645)$
$1(T_1^+)$	$31-12+24+15,\ (123456\to231564),\ (123456\to312645)$
$1(T_2^+)$	$11+21-14+24,\ (123456\to231564),\ (123456\to312645)$
$1(T_2^+)$	$31+12+34-15,\ (123456\to231564),\ (123456\to312645)$
$1(A_2^-)$	$31+12+23-34-15-26$
$1(E^-)$	$31-12-34+15,\ \ 31+12-2\times23-34-15+2\times26$
$1(T_1^-)$	$11+21+22+32-14+24+25-35$
	$(123456\to231564),\ (123456\to312645)$
$1(T_1^-)$	$11-21-22+32-14-24-25-35$
	$(123456\to231564),\ (123456\to312645)$
$1(T_1^-)$	$31+34,\ (123456\to231564),\ (123456\to312645)$
$1(T_2^-)$	$11-13+14-16,\ (123456\to231564),\ (123456\to312645)$
$1(T_2^-)$	$11-32-14+35,\ (123456\to231564),\ (123456\to312645)$

Table C.4: Higgs-W operators from Eq. (C.1) with $|\vec{p}| = \sqrt{3}(2\pi/L)$.

$I(\Lambda^P)$	Operator
$1(A_1^+)$	$10 + 20 + 30 - 11 + 21 + 31 + 12 - 22 + 32 + 13 + 23 - 33$
$1(E^+)$	$10 - 20 - 11 - 21 + 12 + 22 + 13 - 23$
	$10 + 20 - 2 \times 30 - 11 + 21 - 2 \times 31$
	$+12 - 22 - 2 \times 32 + 13 + 23 + 2 \times 33$
$1(T_1^+)$	$10 - 20 + 11 + 21 - 12 - 22 + 13 - 23$
	$(0123 \to 0231),\ (0123 \to 0312)$
$1(T_2^+)$	$10 - 11 - 12 - 13$
	$(0123 \to 0231),\ (0123 \to 0312)$
$1(T_2^+)$	$10 + 20 + 11 - 21 - 12 + 22 + 13 + 23$
	$(0123 \to 0231),\ (0123 \to 0312)$
$1(A_2^-)$	$10 + 20 + 30 + 11 - 21 - 31 - 12 + 22 - 32 - 13 - 23 + 33$
$1(E^-)$	$10 - 20 + 11 + 21 - 12 - 22 - 13 + 23$
	$10 + 20 - 2 \times 30 + 11 - 21 + 2 \times 31$
	$-12 + 22 + 2 \times 32 - 13 - 23 - 2 \times 33$
$1(T_1^-)$	$10 + 11 + 12 + 13$
	$(0123 \to 0231),\ (0123 \to 0312)$
$1(T_1^-)$	$10 + 20 - 11 + 21 + 12 - 22 - 13 - 23$
	$(0123 \to 0231),\ (0123 \to 0312)$
$1(T_2^-)$	$10 - 20 - 11 - 21 + 12 + 22 - 13 + 23$
	$(0123 \to 0231),\ (0123 \to 0312)$

Table C.5: W-W operators from Eq. (C.2) with $|\vec{p}| = 2\pi/L$ and $I = 0$.

$I(\Lambda^P)$	Operator
$0(A_1^+)$	$111 + 222 + 333$
$0(A_1^+)$	$221 + 331 + 332 + 112 + 113 + 223$
$0(A_2^+)$	$221 - 331 + 332 - 112 + 113 - 223$
$0(E^+)$	$111 - 222, \quad 111 + 222 - 2 \times 333$
$0(E^+)$	$112 + 113 - 223 - 221$
	$112 + 113 + 223 + 221 - 2 \times 331 - 2 \times 332$
$0(E^+)$	$112 - 113 - 223 + 221$
	$112 - 113 + 223 - 221 - 2 \times 331 + 2 \times 332$
$0(T_1^+)$	$121 + 211 - 122 - 212, \ (123 \to 231), \ (123 \to 312)$
$0(T_2^+)$	$231 + 321, \ (123 \to 231), \ (123 \to 312)$
$0(T_2^+)$	$121 + 211 + 122 + 212, \ (123 \to 231), \ (123 \to 312)$
$0(A_1^-)$	$231 - 321 + 312 - 132 + 123 - 213$
$0(E^-)$	$231 - 321 - 312 + 132$
	$231 - 321 + 312 - 132 - 2 \times 123 + 2 \times 213$
$0(T_1^-)$	$311 - 131 - 232 - 322, \ (123 \to 231), \ (123 \to 312)$
$0(T_2^-)$	$311 - 131 + 232 - 322, \ (123 \to 231), \ (123 \to 312)$

Table C.6: W-W operators from Eq. (C.2) with $|\vec{p}| = 2\pi/L$ and $I = 1$.

$I(\Lambda^P)$	Operator
$1(A_2^-)$	$231 + 321 + 312 + 132 + 123 + 213$
$1(E^-)$	$231 + 321 - 312 - 132$
	$231 + 321 + 312 + 132 - 2 \times 123 - 2 \times 213$
$1(T_1^+)$	$231 - 321,\ (123 \to 231),\ (123 \to 312)$
$1(T_1^+)$	$121 - 211 + 122 - 212,\ (123 \to 231),\ (123 \to 312)$
$1(T_1^-)$	$111,\ (123 \to 231),\ (123 \to 312)$
$1(T_1^-)$	$221 + 331,\ (123 \to 231),\ (123 \to 312)$
$1(T_1^-)$	$311 + 131 + 232 + 322,\ (123 \to 231),\ (123 \to 312)$
$1(T_2^+)$	$121 - 211 - 122 + 212,\ (123 \to 231),\ (123 \to 312)$
$1(T_2^-)$	$221 - 331,\ (123 \to 231),\ (123 \to 312)$
$1(T_2^-)$	$311 + 131 - 232 - 322,\ (123 \to 231),\ (123 \to 312)$

Table C.7: W-W operators from Eq. (C.2) with $|\vec{p}| = \sqrt{2}(2\pi/L)$, $I = 0$ and $P = +1$.

$I(\Lambda^P)$	Operator
$0(A_1^+)$	$111 + 221 + 222 + 332 + 333 + 113 + 114 + 224 + 225 + 335 + 336 + 116$
$0(A_1^+)$	$331 + 112 + 223 + 334 + 115 + 226$
$0(A_1^+)$	$121 + 211 + 232 + 322 + 313 + 133 - 124 - 214 - 235 - 325 - 316 - 136$
$0(A_2^+)$	$112 - 221 + 222 - 332 + 333 - 113 + 114 - 224 + 225 - 335 + 336 - 116$
$0(E^+)$	$111 + 221 - 222 - 332 + 114 + 224 - 225 - 335$
	$111 + 221 + 222 + 332 - 2 \times 333 - 2 \times 113$
	$+114 + 224 + 225 + 335 - 2 \times 336 - 2 \times 116$
$0(E^+)$	$111 - 221 - 222 + 332 + 114 - 224 - 225 + 335$
	$111 - 221 + 222 - 332 - 2 \times 333 + 2 \times 113$
	$+114 - 224 + 225 - 335 - 2 \times 336 + 2 \times 116$
$0(E^+)$	$331 - 112 + 334 - 115$
	$331 + 112 - 2 \times 223 + 334 + 115 - 2 \times 226$
$0(E^+)$	$121 + 211 - 232 - 322 - 124 - 214 + 235 + 325$
	$121 + 221 + 232 + 322 - 2 \times 313 - 2 \times 133$
	$+124 + 224 + 235 + 325 - 2 \times 316 - 2 \times 136$
$0(T_1^+)$	$111 - 221 - 114 + 224$
	$(123456 \to 231564),\ (123456 \to 312645)$
$0(T_1^+)$	$131 + 311 + 231 + 321 - 212 - 122 - 312 - 132$
	$+134 + 314 - 234 - 324 + 215 + 125 - 315 - 135$
	$(123456 \to 231564),\ (123456 \to 312645)$
$0(T_1^+)$	$131 + 311 - 231 - 321 + 212 + 122 - 312 - 132$
	$+134 + 314 + 234 + 324 - 215 - 125 - 315 - 135$
	$(123456 \to 231564),\ (123456 \to 312645)$
$0(T_2^+)$	$111 + 221 - 114 - 224$
	$(123456 \to 231564),\ (123456 \to 312645)$
$0(T_2^+)$	$331 - 334$
	$(123456 \to 231564),\ (123456 \to 312645)$
$0(T_2^+)$	$131 + 311 + 231 + 321 + 212 + 122 + 312 + 132$
	$+134 + 314 - 234 - 324 - 214 - 124 + 314 + 134$
	$(123456 \to 231564),\ (123456 \to 312645)$
$0(T_2^+)$	$131 + 311 - 231 - 321 - 212 - 122 + 312 + 132$
	$+134 + 314 + 234 + 324 + 214 + 124 + 314 + 134$
	$(123456 \to 231564),\ (123456 \to 312645)$

Table C.8: W-W operators from Eq. (C.2) with $|\vec{p}| = \sqrt{2}(2\pi/L)$, $I = 0$ and $P = -1$.

$I(\Lambda^P)$	Operator
$0(A_1^-)$	$131 - 311 - 231 + 321 + 212 - 122 - 312 + 132 + 323 - 233 - 123 + 213$
	$-134 + 314 - 234 + 324 - 215 + 125 - 315 + 135 - 326 + 236 - 126 + 216$
$0(A_2^-)$	$131 - 311 + 231 - 321 + 212 - 122 + 312 - 132 + 323 - 233 + 123 - 213$
	$-134 + 314 + 234 - 324 - 215 + 125 + 315 - 135 - 326 + 236 + 126 - 216$
$0(E^-)$	$131 - 311 - 231 + 321 - 212 + 122 + 312 - 132$
	$-134 + 314 - 234 + 324 + 215 - 125 + 315 - 135$
	$131 - 311 - 231 + 321 + 212 - 122 - 312 + 132$
	$-2 \times (+323 - 233 - 123 + 213)$
	$-134 + 314 - 234 + 324 - 215 + 125 - 315 + 135$
	$-2 \times (-326 + 236 - 126 + 216)$
$0(E^-)$	$131 - 311 + 231 - 321 - 212 + 122 - 312 + 132$
	$-134 + 314 + 214 - 124 + 215 - 125 - 315 + 135$
	$131 - 311 + 231 - 321 + 212 - 122 + 312 - 132$
	$-2 \times (+323 - 233 + 123 - 213)$
	$-134 + 314 + 234 - 324 - 215 + 125 + 315 - 135$
	$-2 \times (-326 + 236 + 126 - 216)$
$0(T_1^-)$	$121 - 211 - 232 + 322 + 124 - 214 + 235 - 325$
	$(123456 \to 231564),\ (123456 \to 312645)$
$0(T_1^-)$	$131 - 311 + 231 - 321 + 134 - 314 - 234 + 234$
	$(123456 \to 231564),\ (123456 \to 312645)$
$0(T_2^-)$	$121 - 211 + 232 - 322 + 124 - 214 - 235 + 325$
	$(123456 \to 231564),\ (123456 \to 312645)$
$0(T_2^-)$	$131 - 311 - 231 + 321 + 134 - 314 + 234 - 324$
	$(123456 \to 231564),\ (123456 \to 312645)$

Table C.9: W-W operators from Eq. (C.2) with $|\vec{p}| = \sqrt{2}(2\pi/L)$, $I = 1$ and $P = +1$.

$I(\Lambda^P)$	Operator
$1(A_2^+)$	$121 - 211 + 232 - 322 + 313 - 133 - 124 + 214 - 235 + 325 - 316 + 136$
$1(E^+)$	$121 - 211 - 232 + 322 - 124 + 214 + 235 - 325$
	$121 - 211 + 232 - 322 - 2 \times 313 + 2 \times 133$
	$-124 + 214 - 235 + 325 + 2 \times 316 - 2 \times 136$
$1(T_1^+)$	$121 - 211 + 124 - 214$
	$(123456 \to 231564),\ (123456 \to 312645)$
$1(T_1^+)$	$131 - 311 + 231 - 321 - 212 + 122 - 312 + 132$
	$+134 - 314 - 234 + 324 + 215 - 125 - 315 + 135$
	$(123456 \to 231564),\ (123456 \to 312645)$
$1(T_1^+)$	$131 - 311 - 231 + 321 + 212 - 122 - 312 + 132$
	$+134 - 314 + 234 - 324 - 215 + 125 - 315 + 135$
	$(123456 \to 231564),\ (123456 \to 312645)$
$1(T_2^+)$	$131 - 311 + 231 - 321 + 212 - 122 + 312 - 132$
	$+134 - 314 - 234 + 324 - 215 + 125 + 315 - 135$
	$(123456 \to 231564),\ (123456 \to 312645)$
$1(T_2^+)$	$131 - 311 - 231 + 321 - 212 + 122 + 312 - 132$
	$+134 - 314 + 234 - 324 + 215 - 125 + 315 - 135$
	$(123456 \to 231564),\ (123456 \to 312645)$

Table C.10: W-W operators from Eq. (C.2) with $|\vec{p}| = \sqrt{2}(2\pi/L)$, $I = 1$ and $P = -1$.

$I(\Lambda^P)$	Operator
$1(A_1^-)$	$-131 - 311 + 231 + 321 - 212 + 122 + 312 + 132 - 323 - 233 + 123 + 213$
	$+134 + 314 - 234 + 324 + 215 + 125 + 315 + 135 + 326 + 236 + 126 + 216$
$1(A_2^-)$	$131 + 311 + 231 + 321 + 212 + 122 + 312 + 132 + 323 + 233 + 123 + 213$
	$-134 - 314 + 234 + 324 - 215 - 125 + 315 + 135 - 326 - 236 + 126 + 216$
$1(E^-)$	$131 + 311 + 231 + 321 - 212 - 122 - 312 - 132$
	$-134 - 314 + 234 + 324 + 215 + 125 - 315 - 135$
	$131 + 311 + 231 + 321 + 212 + 122 + 312 + 132$
	$-2 \times (+323 + 232 + 123 + 213)$
	$-134 - 314 + 234 + 324 - 215 - 125 + 315 + 135$
	$-2 \times (-326 - 236 + 126 + 216)$
$1(E^-)$	$131 + 311 - 231 - 321 - 212 - 122 + 312 + 132$
	$-134 - 314 - 234 - 324 + 215 + 125 + 315 + 135$
	$131 + 311 - 231 - 321 + 212 + 122 - 312 - 132$
	$-2 \times (+323 + 232 - 123 - 213)$
	$-134 - 314 - 234 - 324 - 215 - 125 - 315 - 135$
	$-2 \times (-323 - 232 - 123 - 213)$
$1(T_1^-)$	$111 - 221 - 222 + 332 - 114 + 224 - 225 + 335$
	$(123456 \to 231564),\ (123456 \to 312645)$
$1(T_1^-)$	$331 + 112 - 334 + 115$
	$(123456 \to 231564),\ (123456 \to 312645)$
$1(T_1^-)$	$121 + 211 + 232 + 322 + 124 + 214 - 235 - 325$
	$(123456 \to 231564),\ (123456 \to 312645)$
$1(T_1^-)$	$131 + 311 + 231 + 321 + 134 + 314 - 234 - 324$
	$(123456 \to 231564),\ (123456 \to 312645)$
$1(T_2^-)$	$111 - 221 + 222 - 332 - 114 + 224 + 225 - 335$
	$(123456 \to 231564),\ (123456 \to 312645)$
$1(T_2^-)$	$-331 + 112 + 334 + 115$
	$(123456 \to 231564),\ (123456 \to 312645)$
$1(T_2^-)$	$121 + 211 - 232 - 322 + 124 + 214 + 235 + 325$
	$(123456 \to 231564),\ (123456 \to 312645)$
$1(T_2^-)$	$131 + 311 - 231 - 321 + 134 + 314 + 234 + 324$
	$(123456 \to 231564),\ (123456 \to 312645)$

Table C.11: W-W operators from Eq. (C.2) with $|\vec{p}| = \sqrt{3}(2\pi/L)$, $I = 0$ and $P = +1$.

$I(\Lambda^P)$	Operator
$0(A_1^+)$	$110 + 220 + 330 + 111 + 221 + 331 + 112 + 222 + 332 + 113 + 223 + 333$
$0(A_1^+)$	$120 + 210 + 230 + 320 + 310 + 130 - 121 - 211 + 231 + 321 - 311 - 131$
	$-122 - 212 - 232 - 322 + 312 + 132 + 123 + 213 - 233 - 323 - 313 - 133$
$0(E^+)$	$110 - 220 + 111 - 221 + 112 - 222 + 113 - 223,$
	$110 + 220 - 2 \times 330 + 111 + 221 - 2 \times 331$
	$+112 + 222 - 2 \times 332 + 113 + 223 - 2 \times 333$
$0(T_1^+)$	$110 - 220 - 111 + 221 - 112 + 222 + 113 - 223,$
	$(0123 \to 0231),\ (0123 \to 0312)$
$0(T_1^+)$	$120 + 210 - 230 - 320 + 121 + 211 + 231 + 321$
	$-122 - 212 + 232 + 322 - 123 - 213 - 233 - 323,$
	$(0123 \to 0231),\ (0123 \to 0312)$
$0(T_2^+)$	$110 + 111 - 112 - 113,$
	$(0123 \to 0231),\ (0123 \to 0312)$
$0(T_2^+)$	$110 + 220 - 111 - 221 - 112 - 222 + 113 + 223$
	$(0123 \to 0231),\ (0123 \to 0312)$
$0(T_2^+)$	$120 + 210 + 230 + 320 + 121 + 211 - 231 - 321$
	$-122 - 212 - 232 - 322 - 123 - 213 + 233 + 323,$
	$(0123 \to 0231),\ (0123 \to 0312)$
$0(T_2^+)$	$120 + 210 - 230 - 320 + 121 + 211 - 231 - 321$
	$+122 + 212 - 232 - 322 + 123 + 213 - 233 - 323,$
	$(0123 \to 0231),\ (0123 \to 0312)$

Table C.12: W-W operators from Eq. (C.2) with $|\vec{p}| = \sqrt{3}(2\pi/L)$, $I = 0$ and $P = -1$.

$I(\Lambda^P)$	Operator
$0(A_1^-)$	$120 - 210 + 230 - 320 + 310 - 130 + 121 - 211 - 231 + 321 + 311 - 131$
	$+122 - 212 + 232 - 322 - 312 + 132 - 123 + 213 + 233 - 323 + 313 - 133$
$0(E^-)$	$120 - 210 - 230 + 320 + 121 - 211 + 231 - 321$
	$+122 - 212 - 232 + 322 - 123 + 213 - 233 + 323,$
	$120 - 210 + 230 - 320 - 2 \times 310 + 2 \times 130$
	$+121 - 211 - 231 + 321 - 2 \times 311 + 2 \times 131$
	$+122 - 212 + 232 - 322 + 2 \times 312 - 2 \times 132$
	$-123 + 213 + 233 - 323 - 2 \times 313 + 2 \times 133$
$0(T_1^-)$	$120 - 210 - 230 + 320 - 121 + 211 - 231 + 321$
	$+122 - 212 - 232 + 322 + 123 - 213 + 233 - 323,$
	$(0123 \to 0231),\ (0123 \to 0312)$
$0(T_2^-)$	$120 - 210 - 121 + 211 - 122 + 212 - 123 + 213,$
	$(0123 \to 0231),\ (0123 \to 0312)$
$0(T_2^-)$	$120 - 210 + 230 - 320 - 121 + 211 + 231 - 321$
	$+122 - 212 + 232 - 322 + 123 - 213 - 233 + 323,$
	$(0123 \to 0231),\ (0123 \to 0312)$

Table C.13: W-W operators from Eq. (C.2) with $|\vec{p}| = \sqrt{3}(2\pi/L)$, $I = 1$ and $P = +1$.

$I(\Lambda^P)$	Operator
$1(A_2^+)$	$120 - 210 + 230 - 320 + 310 - 130 - 121 + 211 + 231 - 321 - 311 + 131$
	$-122 + 212 - 232 + 322 + 312 - 132 + 123 - 213 - 233 + 323 - 313 + 133$
$1(E^+)$	$120 - 210 - 230 + 320 - 121 + 211 - 231 + 321$
	$-122 + 212 + 232 - 322 + 123 - 213 + 233 - 323$
	$120 - 210 + 230 - 320 - 2 \times 310 + 2 \times 130$
	$-121 + 211 + 231 - 321 + 2 \times 311 - 2 \times 131$
	$-122 + 212 - 232 + 322 - 2 \times 312 + 2 \times 132$
	$+123 - 213 - 233 + 323 + 2 \times 313 - 2 \times 133$
$1(T_1^+)$	$120 - 210 + 121 - 211 + 122 - 212 + 123 - 213$
	$(0123 \to 0231),\ (0123 \to 0312)$
$1(T_1^+)$	$120 - 210 + 230 - 320 + 121 - 211 - 231 + 321$
	$-122 + 212 - 232 + 322 - 123 + 213 + 233 - 323$
	$(0123 \to 0231),\ (0123 \to 0312)$
$1(T_2^+)$	$120 - 210 - 230 + 320 + 121 - 211 + 231 - 321$
	$-122 + 212 + 232 - 322 - 123 + 213 - 233 + 323$
	$(0123 \to 0231),\ (0123 \to 0312)$

Table C.14: W-W operators from Eq. (C.2) with $|\vec{p}| = \sqrt{3}(2\pi/L)$, $I = 1$ and $P = -1$.

$I(\Lambda^P)$	Operator
$1(A_2^-)$	$110 + 220 + 330 - 111 - 221 - 331 - 112 - 222 - 332 - 113 - 223 - 333$
$1(A_2^-)$	$120 + 210 + 230 + 320 + 310 + 130 + 121 + 211 - 231 - 321 + 311 + 131$
	$+122 + 212 + 232 + 322 - 312 - 132 - 123 - 213 + 233 + 323 + 313 + 133$
$1(E^-)$	$110 - 220 - 111 + 221 - 112 + 222 - 113 + 223$
	$110 + 220 - 2 \times 330 + 111 + 221 - 2 \times 331$
	$112 + 222 - 2 \times 332 + 113 + 223 - 2 \times 333$
$1(E^-)$	$120 + 210 - 230 - 320 + 121 + 211 + 231 + 321$
	$+122 + 212 - 232 - 322 - 123 - 213 - 233 - 323$
	$120 + 210 + 230 + 320 - 2 \times 310 - 2 \times 130$
	$+121 + 211 - 231 - 321 - 2 \times 311 - 2 \times 131$
	$+122 + 212 + 232 + 322 + 2 \times 312 + 2 \times 132$
	$-123 - 213 + 233 + 323 - 2 \times 313 - 2 \times 133$
$1(T_1^-)$	$110 - 111 + 112 + 113$
	$(0123 \to 0231),\ (0123 \to 0312)$
$1(T_1^-)$	$110 + 220 + 111 + 221 + 112 + 222 - 113 - 223$
	$(0123 \to 0231),\ (0123 \to 0312)$
$1(T_1^-)$	$120 + 210 - 121 - 211 - 122 - 212 - 123 - 213$
	$(0123 \to 0231),\ (0123 \to 0312)$
$1(T_1^-)$	$120 + 210 + 230 + 320 - 121 - 211 + 231 + 321$
	$+122 + 212 + 232 + 322 + 123 + 213 - 233 - 323$
	$(0123 \to 0231),\ (0123 \to 0312)$
$1(T_2^-)$	$110 - 220 + 111 - 221 + 112 - 222 - 113 + 223$
	$(0123 \to 0231),\ (0123 \to 0312)$
$1(T_2^-)$	$120 + 210 - 230 - 320 - 121 - 211 - 231 - 321$
	$+122 + 212 - 232 - 322 + 123 + 213 + 233 + 323$
	$(0123 \to 0231),\ (0123 \to 0312)$

Appendix D

Bottomonium and Bottom Meson Data

Numerical values from Figs. 3.5, 3.7, 3.8 and 3.9 are provided in Tables D.1, D.2, D.3 and D.4 respectively.

Table D.1: Bottomonium simulation energies in lattice units and masses in units of MeV/c^2. Lattice values in physical units for the $J = 2, 3$ states are dimensionally averaged over the lattice irreducible representations. Only statistical bootstrap errors are shown for this work.

particle	J^{PC}	simulation energy	mass [MeV/c^2]	
			this work	experiment [108, 109]
$\eta_b(1S)$	0^{-+}	0.23401(7)	9402.3(3)	9398.0(3.2)
$\Upsilon(1S)$	1^{--}	0.25963(10)	9460.30(26)	9460.30(26)
$\eta_b(2S)$	0^{-+}	0.497(3)	9998(6)	9999(4)
$\Upsilon(2S)$	1^{--}	0.507(3)	10020(7)	10023.3(3)
$\eta_b(3S)$	0^{-+}	0.637(19)	10314(44)	-
$\Upsilon(3S)$	1^{--}	0.646(23)	10334(52)	10355.2(5)
$h_b(1P)$	1^{+-}	0.4540(5)	9900.2(9)	9899.3(1.0)
$\chi_{b0}(1P)$	0^{++}	0.4386(4)	9865.3(1.0)	9859.4(5)
$\chi_{b1}(1P)$	1^{++}	0.4507(5)	9892.7(9)	9892.8(4)
$\chi_{b2}(1P)$	2^{++}	$0.4599(6)_E$	9913.1(1.0)	9912.2(4)
		$0.4596(6)_{T_2}$		
$h_b(2P)$	1^{+-}	0.595(5)	10219(11)	10259.8(1.2)
$\chi_{b0}(2P)$	0^{++}	0.584(5)	10194(12)	10232.5(6)
$\chi_{b1}(2P)$	1^{++}	0.592(5)	10212(11)	10255.5(5)
$\chi_{b2}(2P)$	2^{++}	$0.600(6)_E$	10227(13)	10268.7(5)
		$0.598(6)_{T_2}$		
$\eta_{b2}(1D)$	2^{-+}	$0.571(3)_E$	10163(3)	-
		$0.5693(15)_{T_2}$		
$\Upsilon(1D)$	1^{--}	0.5646(9)	10150(2)	-
$\Upsilon_2(1D)$	2^{--}	0.5689(15)	10161(3)	10163.7(1.4)
		0.5697(17)		
$\Upsilon_3(1D)$	3^{--}	$0.5728(18)_{A_2}$	10172(3)	-
		$0.5761(10)_{T_1}$		
		$0.5730(16)_{T_2}$		
$\eta_{b2}(2D)$	2^{-+}	$0.712(11)_E$	10458(26)	-
		$0.693(18)_{T_2}$		
$\Upsilon(2D)$	1^{--}	0.675(17)	10401(39)	-
$\Upsilon_2(2D)$	2^{--}	$0.690(16)_E$	10447(25)	-
		$0.699(10)_{T_2}$		
$\Upsilon_3(2D)$	3^{--}	$0.703(24)_{A_2}$	10459(37)	-
		$0.704(22)_{T_1}$		
		$0.698(15)_{T_2}$		
$h_{b3}(1F)$	3^{+-}	$0.654(4)_{A_2}$	10355(7)	-
		$0.655(4)_{T_2}$		
$\chi_{b3}(1F)$	3^{++}	0.653(5)	10350(12)	-
$\eta_{b4}(1G)$	4^{-+}	0.749(4)	10568(9)	-
$\Upsilon_4(1G)$	4^{--}	0.760(9)	10592(21)	-

Table D.2: B_c meson simulation energies in lattice units and mass differences with respect to the lightest B_c state in units of MeV/c^2. Lattice values in physical units for the $J = 2, 3$ states are dimensionally averaged over the different lattice irreducible representations. Only statistical bootstrap errors are shown for this work.

particle	J^P	simulation energy	$m - m_{B_c(1S)}$ [MeV/c^2]	
			this work	experiment [108, 114]
$B_c(1S)$	0^-	0.73373(14)	0	0
$B_c^*(1S)$	1^-	0.75914(14)	57.5(3)	-
$B_c(2S)$	0^-	0.985(2)	568(6)	565(6)
$B_c^*(2S)$	1^-	1.000(3)	603(6)	-
$B_{c0}^*(1P)$	0^+	0.9266(8)	436(2)	-
$B_{c1}(1P)$	1^+	0.9445(9)	477(2)	-
$B'_{c1}(1P)$	1^+	0.9496(10)	489(2)	-
$B_{c2}^*(1P)$	2^+	$0.9564(13)_E$	505(3)	-
		$0.9569(13)_{T_2}$		
$B_{c0}^*(2P)$	0^+	1.114(9)	861(22)	-
$B_{c1}(2P)$	1^+	1.121(10)	875(24)	-
$B'_{c1}(2P)$	1^+	1.120(11)	875(26)	-
$B_{c2}^*(2P)$	2^+	$1.127(12)_E$	881(27)	-
		$1.120(13)_{T_2}$		
$B_c^*(1D)$	1^-	1.0674(18)	755(5)	-
$B_{c2}(1D)$	2^-	$1.074(3)_E$	775(9)	-
		$1.077(5)_{T_2}$		
$B'_{c2}(1D)$	2^-	$1.072(14)_E$	777(16)	-
		$1.080(7)_{T_2}$		
$B_{c3}^*(1D)$	3^-	$1.089(8)_{A_2}$	794(8)	-
		$1.085(2)_{T_1}$		
		$1.083(6)_{T_2}$		

Table D.3: B_s meson simulation energies in lattice units and masses in units of MeV/c^2. Lattice values in physical units for the $J = 2$ states are dimensionally averaged over the different lattice irreducible representations. Only statistical bootstrap errors are shown for this work.

particle	J^P	simulation energy	mass [MeV/c^2]	
			this work	experiment [108]
$B_s(1S)$	0^-	0.4130(3)	5370.9(1.6)	5366.77(24)
$B_s^*(1S)$	1^-	0.4337(4)	5417.8(1.8)	5415.4(2.3)
$B_s(2S)$	0^-	0.675(6)	5965(14)	-
$B_s^*(2S)$	1^-	0.697(7)	6013(15)	-
$B_{s0}^*(1P)$	0^+	0.590(2)	5770(6)	-
$B_{s1}(1P)$	1^+	0.612(2)	5822(5)	-
$B'_{s1}(1P)$	1^+	0.622(3)	5844(6)	5828.7(4)
$B_{s2}^*(1P)$	2^+	$0.635(3)_E$	5874(7)	5840.0(2)
		$0.636(3)_{T_2}$		

Table D.4: B meson simulation energies in lattice units and masses in units of MeV/c^2. Lattice values in physical units for the $J = 2$ states are dimensionally averaged over the different lattice irreducible representations. Only statistical bootstrap errors are shown for this work.

particle	J^P	simulation energy	mass [MeV/c^2]	
			this work	experiment [108, 116, 117]
$B(1S)$	0^-	0.3757(20)	5287(5)	5276.26(17)
$B^*(1S)$	1^-	0.3937(19)	5327(4)	5325.2(4)
$B(2S)$	0^-	0.648(20)	5904(44)	-
$B^*(2S)$	1^-	0.675(18)	5964(41)	-
$B_0^*(1P)$	0^+	0.544(4)	5667(10)	-
$B_1(1P)$	1^+	0.575(3)	5738(8)	-
$B_1'(1P)$	1^+	0.590(4)	5771(10)	5727.7(1.6)
$B_2^*(1P)$	2^+	$0.609(7)_E$	5815(14)	5739.4(5)
		$0.610(6)_{T_2}$		